COULOMB EXPLOSION DYNAMICS

A Dissertation presented to
the Doctoral Committee of S. Tahereh Alavi
at the University of Missouri-Columbia
Department of Chemistry

In Partial Fulfillment
of the Requirements for the Degree
Doctor of Philosophy

by

S. TAHEREH ALAVI

Professor Arthur G. Suits, Dissertation Supervisor

MAY 2022

The undersigned, appointed by the dean of the Graduate School,

have examined the dissertation entitled

COULOMB EXPLOSION DYNAMICS

Presented by S. Tahereh Alavi,

a candidate for the degree of Doctor of Philosophy of Chemistry,

and hereby certify that, in their opinion, it is worthy of acceptance

_____

Professor Arthur G. Suits

_____

Professor Tommy Sewell

_____

Professor Sheila N. Baker

_____

Professor Paul F. Miceli

I dedicate this dissertation to my lovely parents and brothers who have been always supporting me.

ACKNOWLEDGEMENT

I wish to express my deepest appreciation to my advisor, Professor Arthur G. Suits, whose guidance, and support has greatly assisted me throughout my research. Starting a PhD in the field of chemistry despite my passion for science, was quite challenging with an engineering background at first, but with a patient and resourceful advisor it became a joyful journey.

I wish to thank Professor Wen Li, a faculty member of Wayne state university who has generously shared their experimental techniques with our lab and helped us in many ways.

I also wish to thank Dr. Casey Foley, a previous PhD student of our group, who I worked with during my first year of PhD, he has helped me in becoming familiar with the fundamentals of reaction dynamics studies. I would like to show my great appreciation to the previous postdoctoral fellows of our research group who I worked with in femtolab, Dr James Thompson who set up the femtolab and introduced me to the field of femto-chemistry, taught me the fundamentals of mass spectrometry, nonlinear optics, and ultrafast lasers, as well as Dr Graham Cooper who has greatly assisted me in upgrading our spectrometer for Coulomb Explosion experiments, programming and analyzing data.

I am also very grateful to our new postdoctoral fellow, Dr Briony Downes-Ward who has benefited our lab with her great knowledge in this field and assisted me in building optical setups.

I would like to thank other members of our group who were not only great friends to me and made my stay far from family easier, but always helped me in many ways.

I would like to thank our machine shop in the department of physics (Rod Schlotzhauer and Cheston Callais) who has helped us with building various instrumental parts.

At the end, I wish to thank my committee members, Professor Tommy Sewell, Professor Sheila N. Baker and Professor Paul F. Miceli for their time, patience and intellectual collaboration throughout my PhD.

The presented projects here were financially supported by the Defense Threat Reduction Agency (DTRA), the Office of Science, Office of Basic Energy Sciences, Division of Chemical Sciences, Geosciences and Biosciences of the U.S. Department of Energy, and the SLAC National Accelerator laboratory.

TABLE OF CONTENTS

LIST OF TABELES

LIST OF FIGURES

PREFACE

This dissertation is based on the following publications. Chapter 5 will be published in near future.

Chapter 3- J. O. Thompson, **S. T. Alavi**, J. R. Walensky and A. G. Suits. “Time of flight mass spectrometry with direct extraction of a uranium plasma." Int. J. Mass spectrom. 445, 116190, 2019.[1]

Chapter 4- G. A. Cooper, **S. T. Alavi**, W. Li, S. K. Lee and A. G. Suits. "Coulomb Explosion Dynamics of Chlorocarbonylsulfenyl Chloride." J. Phys. Chem. A. 125 (25), 5481, 2021.[2]

Chapter 4- S. T. Alavi, G. A. Cooper and A. G. Suits. “"Coulomb explosion dynamics of methoxycarbonylsulfenyl chloride by 3D multimass imaging." Mol. Phys. 120 (1-2), e1988170, 2022.[3]

ABBREVIATIONS

PES	Potential Energy Surface
HHG	High Harmonic Generation
ATI	Above Threshold Ionization
MPI	Multi-Photon Ionization
IB	Inverse Bremsstrahlung
OTBI	Over the Barrier Ionization
CE	Coulomb Explosion
CEI	Coulomb Explosion Imaging
MCP	Microchannel Plate
TOF	Time of Flight
DC	Direct Current
PEEK	Polyether Ether Ketone
AR	Anti Reflection
MS	Mega Sample
VMI	Velocity Map ion Imaging
CW	Continuous Wave
KLM	Kerr-Lens Mode-locking
SAM	Self Amplitude Modulation
CPA	Chirped-Pulse Amplification
TPF	Two Photon Fluorescence
SHG	Second Harmonic Generation
FWHM	Full Width at Half Maximum
SPM	Self Phase Modulation
HCF	Hollow Core Fiber
PMT	Photo-Multiplier Tuber

PEPECO	Photoelectron-Photoelectron Coincidence
PEPIPICO	Photoelectron-Photoion-Photoion Coincidence
PIPICO	Photoion-Photoion Coincidence
UED	Ultrafast Electron Diffraction
MeV	Mega electronVolt
LIBS	Laser-Induced Breakdown Spectroscopy
LA-ICPMS Spectrometry	Laser ablation Inductively Coupled Plasma Mass
CCSC	chlorocarbonylsulfenyl chloride
MCSC	mthoxycarbonylsulfenyl chloride

Abstract

Chemical reaction dynamics studies emerged with the advent of quantum mechanical theories in 1920s which have the capability of predicting the atomic motions by calculating potential energy surfaces. Experimental studies in this field began to flourish with the advances in molecular beam generation and laser beam technologies many years later leading to the Nobel prize awarded to Herschbach, Lee, and Polanyi in 1986.

Later in 1980s, advances in the production of frequency tunable ultrashort laser pulses with the temporal resolution of femtoseconds led to the birth of the field of femto-chemistry which is the study of molecular dynamics in real time. In the last few decades, various spectroscopic techniques exploiting ultrashort laser pulses have been developed to study the non-adiabatic dynamics of molecules in real time and space.

Laser-induced Coulomb Explosion Imaging (CEI) is a powerful probe technique now emerging in this field, to unravel the structural changes of molecular systems in real time. Extracting structural information from CEI requires imaging of multiple fragments at each experimental cycle which allows us to obtain their relative velocity distribution.

In this work, we successfully coupled a three-dimensional multi-mass coincidence detection technique with CEI to study the dissociation dynamics of complicated polyatomic molecules. Covariance imaging, which is a statistical technique yielding correlated information, was used to find the related momenta of various pairs of ions and reveal different dissociation channels of the parent multi-cation.

Using the combination of these techniques, the strong field dissociative ionization of chlorocarbonylsulfenyl chloride (CCSC) and methoxycarbonylsulfenyl chloride (MCSC) (belonging to thioester family) were studied.

The ultrafast electron diffraction (UED) technique is a complementary method to ultrafast laser spectroscopy, capable of directly resolving the electronic and nuclear dynamics in real time and space due to sensitivity to the spatial atomic distribution in the system.

MeV UED facility is a newly developed apparatus at the SLAC National Accelerator Laboratory offering femtosecond time resolution and sub-Angstrom spatial resolution in the study of gas phase molecular systems. Using this facility, we performed a time-resolved UED experiment to study the UV photodissociation of oxalyl chloride. Previous theoretical and experimental studies have suggested non-consistent results for the UV dissociation of this molecule which results in four fragments upon absorption a single photon. Here, with the initial analysis of diffraction images, and comparison with the theory, we confirmed a concerted four-body dissociation channel as the main mechanism.

Chapter 1

Introduction

1.1 Photoinduced Reaction Dynamics

In molecular reaction dynamics studies, the aim is to understand chemical, physical, and biological reactions from a microscopic point of view. These studies provide us with the necessary information to not only predict and control reactions but also to validate the existing theoretical models[4, 5]. With the advent of quantum mechanical theories in 1920s[6] which were used to calculate the potential energy surfaces, it has become possible to look into the molecular level reaction dynamics as such theories could predict the atomic motion by calculating their interaction energies based on the internuclear distances. Experimentally, introduction of the molecular beam[7] techniques was the starting point of such studies. The molecular beam generation was first experimentally shown by Dunoyer in 1911[8], and later modified by Stern[9] which became the basis of later developments in this field. The significant advances in the laser beam technologies in the mid 1960s[10] and later efforts in the generation of ultrashort laser pulses with the frequency tunability and stability[11, 12]led to the unprecedented progresses in the field of chemical reaction dynamics.

In terms of theory, the most simplified quantum mechanical model describing reaction dynamics is the Born-Oppenheimer approximation where the nuclear and electronic

motions are treated independently due to much shorter time scale of the latter[6]. With this approximation, the potential energy surface (PES) at a given internuclear distance is obtained by simply solving the electronic part of the Schrödinger equation. However, this assumption is not valid in the case of electronic degeneracies where two PES intersect[13]. Non-Born-Oppenheimer dynamics such as potential energy curve crossing[14, 15], charge transfer and [16, 17]quantum tunneling[18-21] happen at ultrafast time scales, making it challenging to be investigated experimentally as they require atomic scale spatial resolution and ultrafast temporal resolution.

The advent of ultrashort laser pulses with picosecond, femtosecond and attosecond time resolution has enabled scientists to unravel the ultrafast photo-induced reaction dynamics by taking snapshots of molecular geometrical changes in real time[22]. In such experiments pioneered by Ahmed Zewail,[23] who was awarded the Nobel prize for this work in 1999, an ultrafast laser beam is used to initiate a non-equilibrium state in the molecular system, and the structural changes are subsequently probed in real time. There are various probing techniques in the realm of ultrafast spectroscopy, making the study of more complicated molecular dynamics possible.

Ultrafast laser spectroscopy techniques have been successful in revealing the electronic dynamics, while the nuclear trajectories and geometrical changes are acquired indirectly by analyzing the spectroscopic features with the help of theory. Recent advances in diffraction-based spectroscopy techniques have enabled us to resolve such changes in real time and space and therefore, have become complementary to the existing laser spectroscopy methods.

1.2 Strong Field Dynamics

With the advent of ultrashort laser pulses (with the duration of femto- and attoseconds), different experimental techniques have been developed to study the dynamics of photoinduced processes in atomic and molecular systems in real time. The electric field strength associated with an ultrashort laser pulse is comparable to the atomic and molecular Coulomb binding forces which leads to many interesting nonlinear phenomena such as high harmonic generation (HHG), above threshold ionization (ATI), multiphoton ionization (MPI) and tunnel ionization.[24-27]

In multiphoton ionization (MPI), electrons are excited from a bound state to the continuum through absorption of multiple photons simultaneously (Figure 1.1(a)). This phenomenon was modeled by Fabre et al.[28] using the lowest order perturbation theory where the ionization rate is calculated through following equation:

$$\Gamma_n = \sigma_n I^n \qquad (1.1)$$

Here σ_n is the generalized cross section, n is the minimum number of photons required for excitation from the initial state to the free state (continuum) and I is the intensity of the beam.

Above threshold ionization (ATI) first investigated by Agostini et al.[29] happens when the ionizing photoelectrons absorb more photons required for ionizations due to the Inverse Bremsstrahlung (IB) effects in the vicinity of the nascent ion field (Figure 1.1(b)).

At higher beam intensity, the field is capable of distorting the atomic and molecular PES and creating a finite barrier energy where the tunnel ionization occurs.[30, 31] In this case,

the electric field of the beam is comparable with the atomic or molecular potential field and cannot be considered as a small perturbation to the system anymore. Tunnel ionization has been shown experimentally[32]. Theoretically we can use Keldysh parameter[33] to determine if tunnel ionization takes over based on the laser beam characteristics:

$$\gamma^2 = 2\omega^2 \frac{I_P}{I} \qquad (1.2)$$

Here, I_P is the ionization potential, ω is the field frequency and I is the laser pulse intensity. For $\gamma>1$ multiphoton dynamics is the main ionization mechanism while for $\gamma<1$ tunnel ionization dominates. In other words, for the tunneling to be the dominant mechanism, the tunneling time through the barrier needs to be shorter than the laser field wave period[34].

High Harmonic Generation (HHG) first experimentally observed by Ferray et al.[35] is a result of ATI, where the produced free electrons recollide with their atomic core after being accelerated in the strong laser field. As a result of this return of electrons and transition to the ground state, high order harmonics of the driving field are emitted. The most popular model for HHG introduced by Corkum et al.[36, 37] is based on a semiclassical approach called the "recollision" model that explains this nonlinear phenomenon in three steps: 1. Release of electron wave-packet into the continuum 2. Acceleration of electrons in the strong field away from the atomic core 3. Return of part of the electron wave packet to the ionic core with high kinetic energy after half an optical cycle which results in energy release in the form of high harmonics of the fundamental beam. The driving field

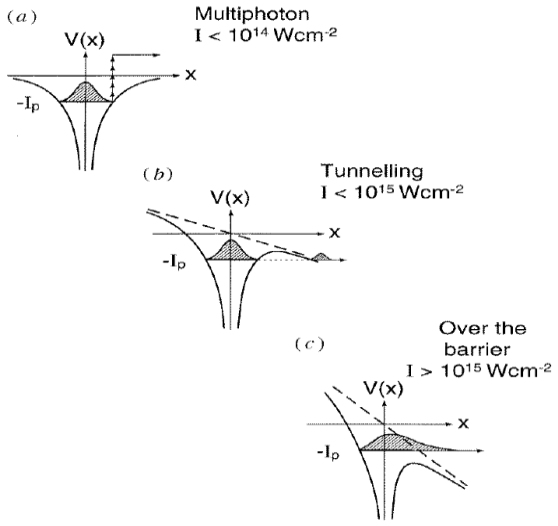

Figure 1.1: (a) at high laser intensities around 100 TW/cm^2 multiphoton ionization is the dominant ionization mechanism (b) at higher intensities the potential energy surface is distorted enough for the tunnel ionization to take place and (c) after a threshold inetnsity, the barrier gets small enough such that the state is no longer bound and over-the-barrier ionization dominates. Adapted with permission from M. Protopapas, C. H. Keitel and P. L. Knight, Rep. Prog. Phys. **60**, 389 (1997) .©IOP Science.

needs to be short enough so that the electron transition to the continuum state happens during one or two optical cycles.[38] High harmonic spectra produced from multi cycle laser beams show a sudden decrease of the conversion efficiency for a few low order harmonics and a plateau of equal intensity with small variations for the rest of high harmonics until reaching to a saturation intensity where a sharp cut-off is observed. Lewenstein et al.[39]

confirmed this model by taking quantum mechanical approaches. The highest harmonic energy can be obtained by the following expression developed from numerical calculations by Krause et al.[40]:

$$E_{max} = I_P + 3.17U_P \quad (1.3)$$

Where I_P is the ionization potential of the atom and U_P is the pondermotive (quiver) energy which is the averaged energy of an electron oscillatory motion gained in the laser field.

As the peak intensity of the pulse increases, the distortion of the potential surfaces continues until the over-the-barrier ionization (OTBI) phenomenon dominates where the initially bound state becomes dissociative (Figure 1.1(c)). The critical laser beam intensity for OTBI is estimated by[41]:

$$I_{OTBI}[\frac{W}{cm^2}] = 4 \times 10^9 (I_p[eV])^4 Z^2 \quad (1.4)$$

where Z is the charge state of the atom and I_P is the ionization potential. If the saturation of ionization intensity (I_{sat}) for a given pulse duration is smaller than I_{OTBI} for a given atom, then the ionization mainly happens through normal MPI due to slow rise of pulse intensity to the peak.[41]

"Coulomb Explosion" (CE) first introduced by Carlson and White[42] as employed here is the phenomenon during which the molecular potential energy surface is distorted in the presence of a strong electric field associated with ultrashort laser pulse and subsequently several electrons escape from the molecule. Various ionization mechanisms have been proposed to explain CE including tunnel ionization and over-the-barrier ionization. Initially CE was induced by accelerating molecular ions (flying with a few percent the

speed of light) toward an ultrathin foil leading to ejection of several electrons and creation of positively charged particles that repel each other strongly. The repelling fragments are then projected onto a time and position sensitive two-dimensional detector to acquire their relative momenta and determine the static structure of the system accordingly. This spectroscopic technique is called "Coulomb Explosion Imaging" (CEI). Most commonly now CE is induced using tabletop intense ultrashort laser pulses where multiply charged parent cations are produced and rapidly dissociate due to repulsion coulombic forces among their constituents' charged fragments (Figure 1.2). Coulomb explosion typically happens faster than the molecular rearrangement [43] making it a powerful technique for extracting the static and dynamical structures of the system of interest. There are different theoretical models introduced to simulate laser-induced Coulomb explosion in molecular systems including coherent electron motion model where the initially ionized electrons cause further ionization through electron impact ionization. [44] In the ionization ignition mechanism model, the ionization is assumed to happen at higher ionization states of the molecule. Here the main mechanism is the barrier suppression. [45] Laser-induced CEI technique is commonly used to reveal the static structure of complicated molecular systems, unravel the multi-channel dissociation dynamics, and monitor the structural changes of polyatomic molecular systems in an ultrafast pump-probe experiment.

To infer such information from CEI we need to first acquire the relative momenta of fragments produced from the same dissociation channels. Therefore, it is essential to use experimental techniques capable of acquiring the velocity distribution of multiple fragments at each experimental cycle.

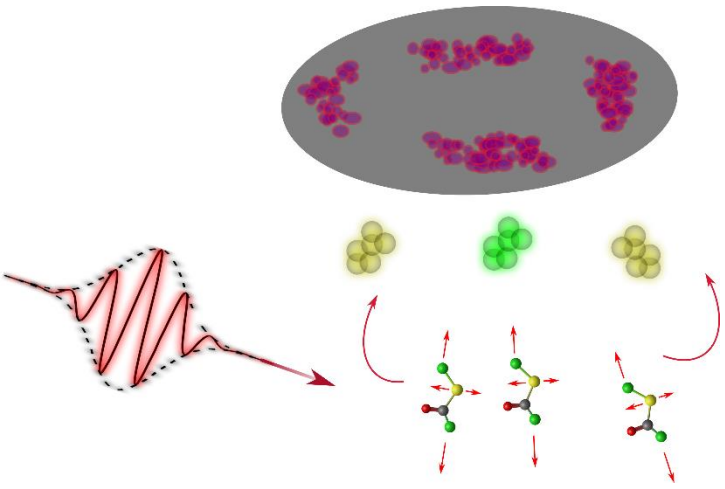

Figure 1.2: Coulomb Explosion Imaging (CEI) of chlorocarbonylsulfenyl chloride.

Chapter 2

Experimental Methods

2.1 Laser-Induced Plasma Mass Spectrometry

The apparatus in these studies consists of a source chamber, main chamber and a time-of-flight (TOF) drift tube at the end of which a microchannel plate (MCP) detector coupled to a phosphor screen is mounted (Figure 2.1). The whole apparatus is under high vacuum using turbomolecular pumps (Varian,T-551 and Osaka,TG1300MCW) backed by a dry scroll pump (Edwards, nXDS 20i). These experiments were carried out under vacuum at a base pressure of 10^{-7} Torr. The source chamber which is equipped with a pulsed piezoelectric valve and skimmer was not used in this experiment. For the laser-induced

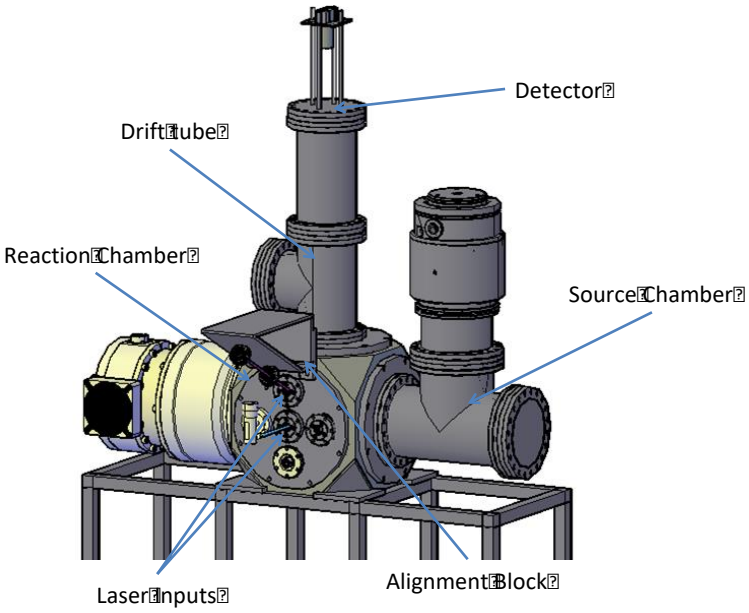

Figure 2.1: The experimental setup used in laser-induced plasma studies.

plasma mass spectrometry studies we used a Nd:YAG laser (Quantra-Ray DCR 3, Spectra Physics) which provides up to 1 J/pulse (10 Hz repetition rate) at 1064 nm with a pulse duration of 8 ns. The laser has an optional frequency conversion unit to provide the second and third harmonics of the fundamental (532 and 355nm respectively). The laser beam is then sent to a set of folding mirrors into a periscope to raise the beam above the ion optic assembly within the apparatus. The main chamber of the apparatus is where the plasma is formed and accelerated into the TOF drift tube region using a modified Wiley-McLaren accelerator[46] composed of four electrodes shown in Figure 2.2. The distances between the electrodes are the same as those described by Townsend et al.[47] for direct current (DC) sliced velocity map ion imaging (employed in other experiments) and are noted in the figure. The flight time of the generated ions can be acquired using Wiley-McLaren equations shown below:

$$U = U_0 + qsE_s + qdE_d \tag{2.1}$$

$$T = T_s + T_d + T_l \tag{2.2}$$

$$T_s = \frac{\sqrt{2m(U_0+qE_s)}}{qE_s} \tag{2.3}$$

$$T_d = \frac{\sqrt{2m}}{qE_d}[\sqrt{U} - (U_0 + qsE_s + qdE_d)] \tag{2.4}$$

$$T_l = L\sqrt{\frac{m}{2qU}} \tag{2.5}$$

Here, U_0 and U are the initial translational energy and the post acceleration total translation energy of the particle, q is the elementary charge, s is the distance from the position where the ions are extracted to the extractor electrode, d is the distance between the extractor

electrode and the grounded electrode and L is the length of the field free region of the flight tube. E_s is the strength of the electric field at position s and E_d is the potential of the extractor electrode. Finally, T_s, T_d, T_l and T are the times the particle spends traveling from the acceleration region to the extractor electrode, from the extractor electrode to the grounded electrode, from the grounded electrode to the detector, and the total flight time respectively. The electrodes were constructed of a mirror-polished stainless steel and a thin nickel mesh (Precision Eforming, MN12, 45 lines per inch with 88% transmission) used to cover the orifice of each electrode except for the repeller to provide a uniform electric field for higher mass resolution. The plasma density is reduced in two steps from the ablation region to the acceleration region.

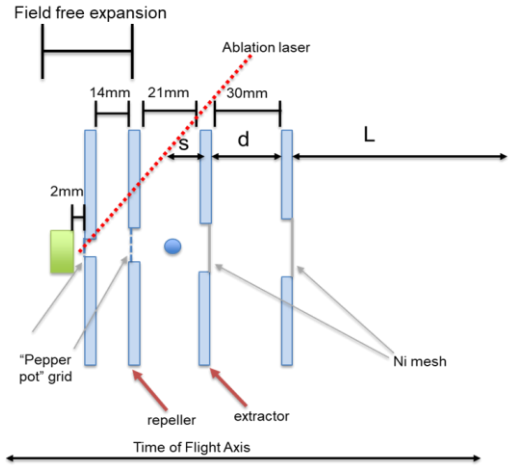

Figure 2.2: The ion optic assembly layout. The red line indicates the path of the ablation laser. The blue circle indicates the center of the accelerator volume.

As shown in Figure 2.1, the first electrode features a single aperture (of 75 ± 20 μm in diameter) in the center of the plate that reduces the initial density. Taking inspiration from Nakajima et al.[48] a "pepper pot" style grid consisting of 9 holes (3 ×3, 1mm spacing, 50 ± 20 μm in diameter each) was fashioned on a 0.004 inch thick plate of stainless steel

mounted on the repeller. The diameter of each aperture was confirmed by optical microscopy. During the acceleration, the two middle electrodes of the assembly (repeller and extractor electrodes) are pulsed to 1500 V and 1220 V respectively from ground while the other electrodes are grounded for the entire experiment. The electrodes were pulsed using a high voltage pulser (DEI, PVX-4140, rise time~100 ns), for 50 μs to provide a constant energy impulse to accelerate the ions. Additionally, resistors of 150 and 50 Ohms were placed inline from the pulser to these two electrodes. For the target, a 25mm×25mm × 1mm gadolinium sheet (693723, Sigma-Aldrich), aluminum foil (99.9%) and natural uranium plates (425-349-30, Goodfellow) were used. No additional cleaning or polishing of the surfaces was performed aside from that of the ablation itself as discussed for the uranium surface below. In each experiment the target plate was mounted in the PEEK (Polyether Ether Ketone) assembly onto a motorized 2D translational stage within 2mm of the entrance electrode of the accelerator located in the reaction chamber. The light was focused onto the target using a 30 cm AR (Anti Reflection) coated fused silica lens through a pair of externally mounted irises prior to entering the chamber through a 1-inch diameter 2mm thick fused silica window. To allow the light to pass through the ion optics, 0.5 cm diameter holes were cut into the electrodes at an angle of 27° to the electrode surfaces. Based on our focusing conditions, we estimate the highest power density of our 8 ns pulsed laser beam to be ~5×10^{11} W/cm^2 at the target, assuming a diffraction limited beam spot at the focus. Due to the geometry of the experiment, the laser does not produce ions directly in the accelerator region, therefore any ions detected must be formed either during the ignition event in the laser focus or from collisions with the plasma as it expands. They also

can result from electron impact ionization during the initial acceleration as the electrons are torn from the neutral plasma.

Once produced, the plasma travels from the target into the assembly in a field-free condition. After some time delay (extraction delay), the accelerator is pulsed to accelerate the ions into the TOF drift tube. The ions were ultimately detected using an 40mm dual microchannel plate (MCP) imaging detector (Beam Imaging Solutions) with the front plate grounded and the back plate biased to 1900-2200 V. The time-of-flight was recorded directly from the MCP using a home-built signal decoupler fed to a 250 MS/s digitizer (NI, PCI-5114). The data acquisition was controlled using the NI Scope software on LabView 2017. The mass spectrum was then recorded and averaged typically for 50 laser shots at each delay. Furthermore, in order to investigate the effect of the field-free propagation time, the delay of the HV switch relative to the laser Q-Switch was controlled by a delay generator (BNC). The change of the delay and acquisition of the mass spectrum was then automated using a program written in LabVIEW by Dr James O.F Thompson.

2.2 Coincidence Momentum Spectroscopy

The experimental setup in these experiments is based on a conventional Velocity Map Imaging (VMI) spectrometer modified to do multi-mass photo-ion coincidence momentum imaging. Here, we successfully coupled Coulomb explosion imaging technique to multi-mass coincidence momentum spectroscopy. The coincidence detection technique utilized in these experiments was initially developed by Lee et al.. [49] The apparatus consists of a source and a reaction chamber along with a Time-of-Flight (TOF) tube all of which are

under high vacuum. Turbo molecular pumps (Agilent technologies, TV551 NAV, Osaka,TG1300MCW, Edwards EXT255H) backed by a dry scroll pump (Edwards, nXDS 20i) were used to generate high vacuum in the chambers (~10^{-7} in the source and ~10^{-9} in the main chamber). In the Coulomb Explosion experiments an additional liquid Nitrogen cold-finger was installed to further decrease the main chamber's pressure. The reaction chamber is equipped with an ion optics assembly consisting of a repeller, extractor and additional electrodes in order to focus the produced ions onto a position sensitive detector which is mounted at the end of the TOF tube. The ion optics assembly used in these experiments has a direct current (DC) slicing configuration which will be discussed further in this chapter. Here, The Coulomb Explosion experiments have been performed in the gas phase where the molecule of interest is first seeded in He (carrier gas) and then is introduced into the source chamber through a pulsed piezoelectric disc valve[50] and passes through a skimmer (Beam Dynamics, Inc.) with an orifice size of 0.2 mm to be collimated before entering the reaction chamber. The two chambers are separated by an aluminum flange onto which the skimmer is mounted. The produced molecular beam in the reaction chamber is intersected perpendicularly with a focused pulsed laser beam in the interaction region (between repeller and extractor electrodes) and goes through dissociation/ionization. The laser pulses in these studies are the output of an ultrafast Ti:Sapphire (KMLabs, Wyvern-1000) which will be discussed further. The produced ions are then extracted and sent toward a dual microchannel plate (MCP) detector coupled to a phosphor screen (P47). As the ions impinge on the detector, their positions are recorded by a CMOS camera. The TOF information is simultaneously collected by a photomultiplier tube (PMT) and transferred to a high-speed digitizer where the full waveform of each PMT

trace is acquired and analyzed. The detection procedure will be discussed in more detail below.

2.3 Ultrafast Laser System

We use a Ti:Sapphire ($Ti:Al_2O_3$) (Titanium-doped sapphire) laser system (KMLabs, Wyvern-1000) to study strong field ionization dynamics of molecules. Ultrashort laser pulses (in the range of femtosecond and picosecond) are normally generated through solid state lasers where a continuous wave (CW) mode-locking technique is used to lock several longitudinal modes in phase and generate high peak intensity pulses.[51-53] Such pulses can be generated through either active mode-locking[54, 55] where an electro-optic or acousto-optic modulator is used for energy transfer to adjacent modes or passive mode-locking[56, 57] where Self Amplitude Modulation (SAM) leads to the phase locking of the modes. Ti:Sapphire laser systems first introduced in 1986 has dominated the field of ultrashort pulse generation due to their huge gain medium and wavelength tunability.[58]

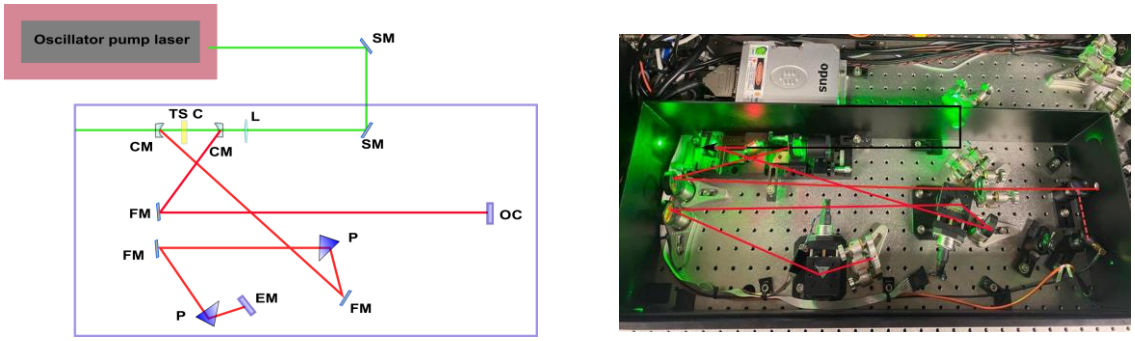

Figure 2.3: Beam path inside the Griffin-W oscillator. SM: steering mirror, L: lens, CM: curved mirror, TS C: Ti:Sapphire crystal, FM: fold mirror, P: prism, EM: end mirror, OC: output coupler.

In our Ti:Sapphire laser system the oscillator (Griffin-W) which is integrated inside the KMLabs Wyvern amplifier system (Figure 2.3) generates the ultrashort pulses through a Kerr-lens Mode-locking (KLM) technique where there is no need to use an external fast saturable absorber (a device with lower loss for higher pulse intensities)[51, 59]. Rather the self-focusing of the beam in the gain medium is exploited. In such self-mode-locking technique, the high intensity part of the beam gets self-focused through Kerr lens effects while the low intensity part remains unfocused, then the beam is passed through an aperture where the unfocused low intensity beam is attenuated and therefore shortening of the pulse is achieved.[52] The oscillator is pumped by a diode laser with 3-3.5 Watts of CW 532 nm beam with a clean TEM_{00} mode.

The Chirped-Pulse Amplification (CPA) technique[60] introduced in 1985 is used to amplify ultrashort pulses coming out of the CW mode-locked oscillators. In this technique the pulse is temporally stretched before entering the amplifying medium in order to prevent the

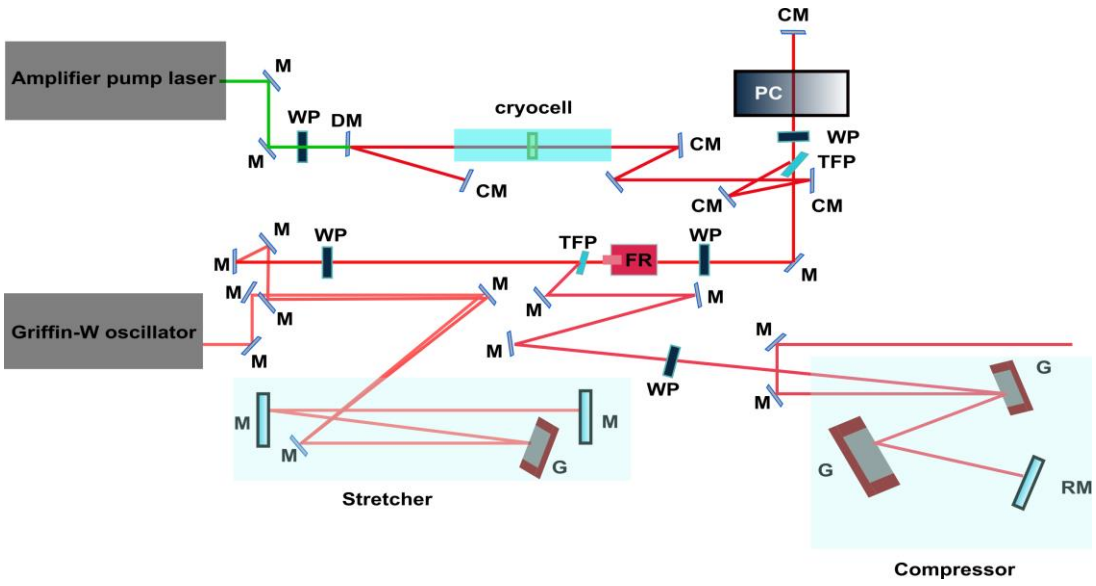

Figure 2.4: Ti:Sapphire amplifier system layout (KMLabs, Wyvern 1000). M: mirror, WP: wave plate, TFP: thin film polarizer, FR: Faraday rotator, G: grating, CM: cavity mirror, PC: Pockels cell, DM: dichroic mirror, RM: roof mirror.

potential damages caused by high intensity pulses to the gain medium or other optical components inside the cavity. In our KMLabs laser system (Figure 2.4), the oscillator pulse train with a repetition rate of ~80 MHz with sub-picosecond temporal width and ~50 nm bandwidth enters the amplifier system. The initial short low energy pulse from the CW mode-locked oscillator is stretched temporally through a single-grating stretcher design. A combination of a half-wave plate and a Pockels cell (a device consisting of an electro-optic crystal) is used to trap inside and reject pulses from the cavity. The amplifying crystal (Ti:Sapphire) is mounted inside a cell under high vacuum (~10^{-10} Torr) using an ion pump and kept at low temperature (~ -220°C) using a cryo-compressor in order to maximize the damage threshold. The amplified pulse is then sent toward a so-called Treacy compression system[61] containing two gratings and a roof mirror to be compressed back to the initial pulse duration.

2.4 Optical Autocorrelator

Since there is no optoelectronic device (e.g. photodiodes) with fast enough response to be able to measure the temporal behavior of ultrashort laser pulses, the pulse itself is used for such measurements through autocorrelation.

Various methods have been developed since the advent of ultrashort pulses (picoseconds/femtoseconds) to measure the pulse duration directly and indirectly. Two Photon Fluorescence (TPF) is one of these methods first introduced by Bell Telephone laboratories scientists[62]. In the TPF method the beam is divided into two identical pulses

and sent through an organic dye cell in opposite directions. The emitted fluorescence is proportional to the square of the input pulse peak intensity, showing a maximum at positions where the two pulses are coincident in time. Therefore, a photograph of the fluorescence track provides information about the pulse autocorrelation.[63] High background interfering with the measurement is the main drawback of this technique.

The more commonly used autocorrelation method which shows higher contrast and accuracy compared to TPF is based on a nonlinear optical correlation where the spatial distribution of second harmonic generation (SHG) through overlapping two replicas of the beam inside nonlinear crystal (Barium borate (BBO) or Potassium dihydrogen phosphate (KDP)) is used to acquire the temporal width of the fundamental pulse. A noncolinear geometry in BBO or orthogonal polarization of two pulses in KDP is used in order to produce background-free signal. The idea of designing an optical autocorrelator is to infer the temporal behavior of the fundamental pulse from the intensity autocorrelation which is measurable by a detector (spectrometer or camera).[63-66] Both TPF and SHG methods are only used to get a good estimate of the pulse duration but they do not provide any information about the pulse shape.

The second order intensity autocorrelation can be obtained from the following equation:[67]

$$A(\tau) = \int_{-\infty}^{+\infty} I(t).I(t+\tau)dt \qquad (2.6)$$

Where I(t) is the intensity distribution of the pulse as a function of time.

Here, in our lab we set up a noncollinear SHG autocorrelator (Figure 2.5) where two identical beams were produced through a 50% beam splitter and sent through two separate optical paths with one containing a motorized translational stage in order to change the delay between pulses. The beams are then focused inside a thin (100 μm thickness) BBO crystal through 10 cm lenses. Here, having the noncolinear geometry enabled us to block the produced SHG from individual pulses as they were traveling in different directions, therefore the integrated SHG signal (emitted along the bisector of the crossover angle[68]) is only observed when the two beams coincide inside the BBO and it has a maximum intensity when the delay between two pulses is zero and vanishes at large delays (depending on the temporal width of the input pulse). Then the second harmonic beam (400 nm) is sent through a filter which blocks the remaining fundamental and is subsequently observed by a detector (spectrometer) to measure the autocorrelation intensity at each delay. A program written in C# by Dr Graham Cooper was used to automatically move the stage and record the signal intensity at each stage position. Then the output data was used to plot the autocorrelation intensity as a function of delay (stage position). The autocorrelation intensity must be symmetric with respect to delay (regardless of the original pulse shape) and any non-symmetrical feature is indicative of a misalignment in the autocorrelator.[67]

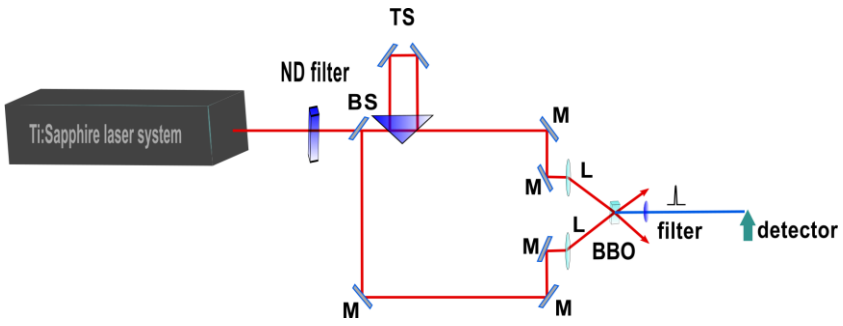

Figure 2.5: Optical design of a single shot intensity autocorrelator based on second harmonic generation. M:mirror, L: lens, BS: beam splitter, TS: translational stage.

$$A(\tau) = A(-\tau) \tag{2.7}$$

Depending on the pulse shape, the pulse duration can be inferred from the Full Width at Half Maximum (FWHM) of the spatial intensity distribution.[69] For $sech^2$ pulse shapes the pulse duration is ~0.65 times of the autocorrelation intensity width while for Gaussian shape pulses this factor is ~0.71.[68] We fit the autocorrelation signal with a Gaussian curve and calculated the FWHM based on it (Figure 2.6). According to this plot and assuming that the output of our tabletop Ti:Sapphire laser system has a Gaussian pulse shape , the temporal width of the pulse is ~90 fs.

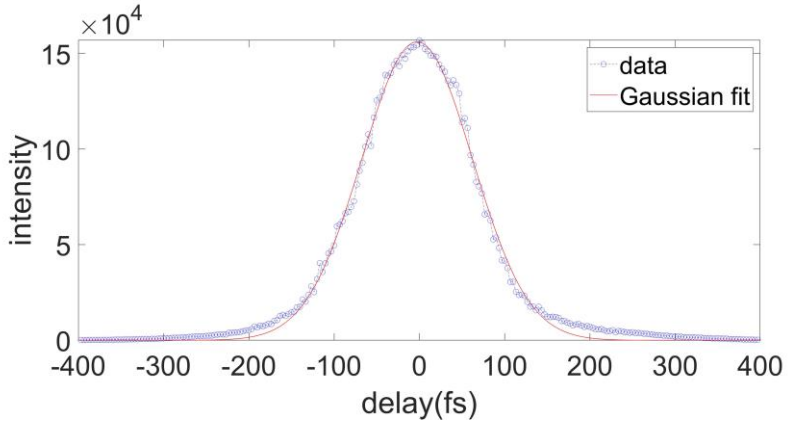

Figure 2.6: Intensity autocorrelation of an ultrashort pulse fit with a Gaussian curve.

2.5 Hollow Core Fiber Compression Setup

Various temporal pulse compression techniques have been devised[70-74] mainly with the purpose of achieving higher temporal resolution in ultrafast spectroscopy experiments and high harmonic generation. To acquire few cycle pulses, it is necessary to have an external optical pulse compressor as the output of a typical CPA system possess a limited frequency

bandwidth. Propagation of high intensity laser pulses through a medium lead to various nonlinear phenomena such as self-focusing, self-phase modulation (SPM) and self-steepening of the pulse governed by nonlinear refractive index of the medium induced by the strong field and varying with the beam intensity. The polarization density of a given material is proportional to the electric field of the laser beam:

$$P = \varepsilon_0 \chi E \tag{2.8}$$

Where E is the electric field associated with a laser source, ε_0 is the permittivity of free space and χ is the susceptibility.[75] When the laser beam intensity increases such that its electric field becomes comparable with the Coulombic forces between atoms within the medium, the polarization is no longer linear and it can be described with a Taylor expansion of the above term:[76]

$$P(t) = \varepsilon_0(\chi^1 E(t) + \chi^2 E^2(t) + \ldots) \tag{2.9}$$

Where χ^n is the n^{th} order susceptibilities. A non-zero χ^n terms shows we have a $(n+1)^{th}$ order nonlinearity in the system. As an example, SPM is a second order nonlinear phenomenon leading to a symmetric spectral broadening of the pulse, while a self-steepening is a third order optical nonlinearity providing asymmetric broadening of the frequency spectrum.[77]

The total refractive index of a medium through which the high intensity laser beam propagates is calculated through the following equation:

$$n = n_0 + n_2 I \tag{2.10}$$

where I is the laser beam intensity, n_0 and n_2 are the linear and second-order nonlinear refractive indices of the material respectively. The nonlinear refractive index of gasses is dependent on the gas type and the pressure.[78]

There are two common steps in any pulse compression technique: 1. Spectral broadening of ultrashort pulses in hollow core fibers, hollow capillary, standard single and multi-mode fibers, photonic waveguides, or filaments created in a gas-filled cell driven by SPM. 2. Subsequent dispersion compensation of the broadened spectrum through optical elements with negative dispersion such as diffraction gratings, prism pairs and chirped mirrors. [79]

Initially frequency-chirped pulses were temporally compressed through SPM in single mode optical fibers followed by optics producing negative dispersion in the pulse. Although, this technique has shown promising pulse compression results down to a few femtoseconds[80-82], it is limited to relatively low input intensity (a few nanojoules/pulse) due to the potential damage to the fiber and higher order nonlinearity which adversely affect the SPM.[83] Hollow core fibers (HCF) filled with noble gases are an alternative pulse compression technique first introduced by Nisoli et al.[83] and have been used widely subsequently.[84-86] Such a setup not only supports high energy throughput (several μJ/pulse) but also it is easier to control the nonlinearity by choosing the gas type and pressure. A long enough fused silica capillary guarantees the exclusive propagation of the fundamental mode.[87]

Noble gases are normally used in HCF compression setups due to their high ionization potential which is necessary to avoid ionization-induced dispersion and loss of intensity. They also show high nonlinearity required for SPM. HCF filled with molecular gasses has been also investigated mainly with the motivation of compressing lower energy input

pulses with longer duration.[88-91] The delayed nonlinearity arising from rotational and vibrational excitations (the laser induced alignment and bond stretching[92]) of such gases can lead to stronger nonlinear phenomena in the case of longer pulses (>100 fs). The nonlinearity of molecular gasses of linear molecules mainly arises from the rotational excitation.[88] In such cases, the nonlinear refractive index contains instantaneous (arising from Kerr effect) and delayed (arising from rotational excitation) components. The delayed rotational nonlinearity temporally overlaps with the multi-cycle pulses (<100 fs) resulting in higher spectral broadening. Beetar et al.[90] has examined the propagation of multi-cycle laser pulses (~280 fs) in various linear molecular gasses and Ar. Their results showed that the strong field-induced alignment in such media leads to enhanced nonlinearity which acts in favor of spectral broadening.

Filamentation based techniques are simpler methods of compressing ultrashort pulses which are solely based on electronic Kerr nonlinearity. Here, unlike HCF based method, multiphoton ionization is exploited to acquire few cycle pulses from ultrashort input pulses. As the optical pulse power propagating in a medium exceeds a critical threshold ($P_{critical} = \frac{\lambda^2}{8\pi n_0 n_2}$) which is dependent on the beam wavelength, and the material refractive indices, the beam starts to self-focus due to Kerr lens effect.[93] Once the self-focusing of the beam overcomes the linear diffraction, a plasma filament is produced due to multi-photon ionization which defocuses the light and the dynamic equilibrium between self-focusing and defocusing continues until defocusing overcomes and the filament stops. Filamentation leads to spectral broadening [38, 94-96] as a result of self-phase modulation and subsequent self-compression of the pulse without the need of using any external optical components for negatively dispersing the pulse. Filamentation in a gaseous medium is used

as a self-optical wave guide where the input pulses with a temporal width of a few tens of femtosecond with sufficiently high intensity can generate pulses close to one optical cycle limit[94] (transform-limited pulse). Although, self-compression of the ultrashort pulses in gas-filled cells through filamentation sounds to have a simple experimental implementation in terms of less sensitivity to the beam alignment and not using any external optical compressors, due to the output beam instabilities arising from the multi-filamentation[97] and better spatial modes of the output beam resulting from the gas-filled hollow core fibers, still in many cases HCF based methods are being used.

Here in our lab we used a flexible fused silica hollow core fiber with Polyimide coating (500 µm internal and 794 µm external diameter) as the wave guide filled with various molecular and atomic gases (Ar, N_2, SO_2, CO_2) with the goal of compressing the output of our Ti:Sapphire laser system (~100 fs) for future time-resolved pump-probe experiments.

The compression setup shown in Figure 2.7 is inspired by a design suggested by Wen Li. The fiber (Polymicro Technologies) is mounted using a couple of reaction column tees

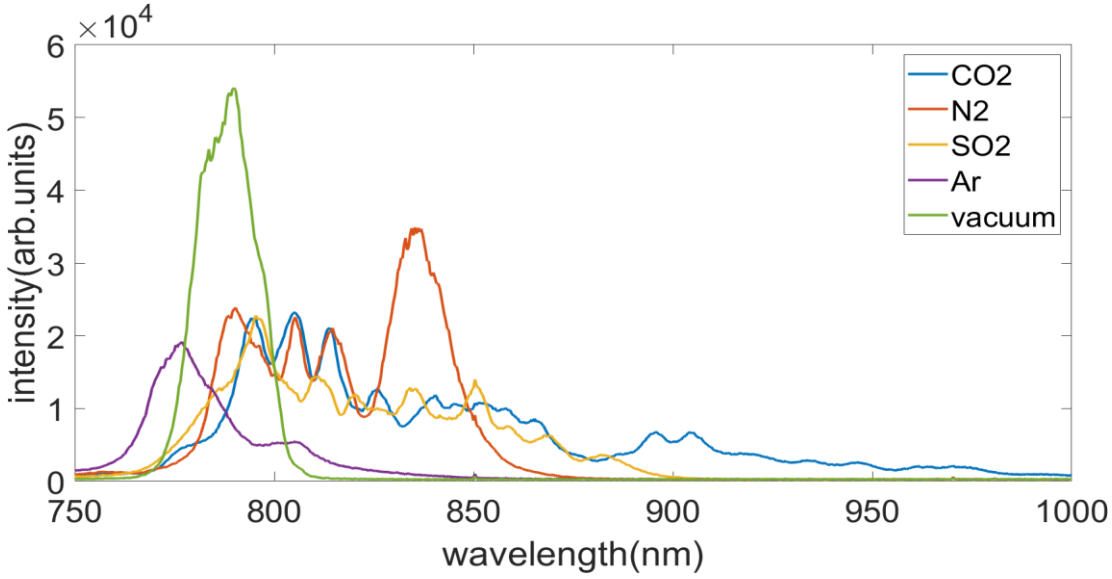

Figure 2.8: Spectral broadening of the input pulses using different gases.

(Valco Instruments) mounted on three-dimensional translational stages. The pulse enters and exit the setup through two 1 mm thick fused silica windows. In order to avoid multiphoton ionization and self-focusing of the beam in the fiber entrance which negatively impact the coupling of the beam with it, we have used a gradient pressure of gas in the system by applying vacuum (~ 1 Torr) in the entrance while gas enters from the other side of the setup. Different length of the fiber was used to get the optimum length for best coupling while getting enough intensity throughput. We got the highest spectral broadening along with a decent Gaussian profile output beam when using a length of 70-90 cm of the fiber and a gas pressure of 15-20 psi of CO^2. The spectral broadening resulted from different gas types is shown in Figure 2.8. The next step is using a set of chirped mirrors to temporally compress the broadened pulse down to a few optical cycles. By fitting a Gaussian model to each spectrum and subsequent Fourier transformation we get the transform limited duration for each pulse summarized in Table 2.1.

Table 2.1: Spectral and Transform-limited temporal width of broadened pulses.

Gas type	Spectral width (FWHM) (nm)	Temporal width (fs) (Transform-limited)
Vacuum	17	55
Ar	26	36
N_2	63	15
SO_2	81	12
CO_2	86	10

2.6 Pulsed Molecular Beam

In the gas phase experiments the sample of interest is first seeded in a carrier gas to minimize clustering. In the cases where the sample is in liquid phase, the carrier gas (He) is passed through a bubbler containing the degassed liquid sample and then enters the source chamber with a backing pressure of about 500 Torr through a pulsed piezoelectric disc valve with an opening time of ~30 μs. The source chamber is at a rest pressure of about 10^{-7} Torr. As the collimated gas beam enters the reaction chamber which is at much lower pressure (6×10^{-9} Torr) through the skimmer orifice, it expands supersonically. The result of such adiabatic expansion is an internally cold molecular beam with narrow velocity distribution and minimum intermolecular interactions.

2.7 Velocity Map ion Imaging (VMI)

The photofragment imaging technique initially was introduced by Chandler and Houston[98] in 1987 where the recoil velocity and angular distribution of fragments produced in a photo-induced process is acquired by sending them toward a two-dimensional position sensitive detector at the end of a TOF tube. The detector is coupled to a phosphor screen which is illuminated as charged particles hit the detector and subsequently imaged using a video camera at each laser shot. In this technique, full three-dimensional velocity distribution of photoproducts is reconstructed from two-dimensional ion images using mathematical methods such as inverse Abel transform. The advantage of such techniques over previous TOF and mass spectrometry techniques, is that they provide the position of

ions at the detector along with their TOF information enabling us to acquire the full velocity distribution of fragments for a given state of interest.

However, the original imaging techniques were limited in terms of translational energy resolution due to using a couple of grids as extractor electrodes which was adopted from the Wiley McLaren Time of Flight accelerator[46] to provide parallel and uniform electric field lines. The distortion in the ion trajectory caused by the grids as well as projection of the whole ionization volume on the detector by the parallel field lines lead to a blur ion image with low velocity resolution. To address such technical issues, Eppink and Parker introduced the Velocity Map ion Imaging (VMI) technique [99] where they used open aperture electrostatic lenses. Such an ion optic assembly creates an electrostatic immersion lens which maps all fragments with the same initial velocity onto the same point on the detector regardless of their initial position in the ionization region. This configuration enhanced the velocity resolution by one order of magnitude and deblurred the images. Also, the transmission of ions in such configuration is 100%, unlike using grids as extraction electrodes.

Although, VMI technique has significantly enhanced the resolution of photofragment images, the necessity of having a cylindrical symmetry parallel to the imaging plane to be able to use the Abel inverse transform method for full momentum reconstruction purposes, limits the applicability of this technique to a certain type of experiments where both pump and probe laser beam polarizations are parallel to the detector plane. Also, using such mathematical methods introduces artifacts to the reconstructed images specially along their symmetry axis. In 2001 Gebhardt et al.[100] introduced Slice Imaging technique to directly acquire the equatorial slice of Newton ion sphere which includes the full translational

energy information. In this experimental technique, a pulsed electric field is used in the acceleration region after a field free expansion leading to a temporal stretching of the ionic cloud along TOF tube by several hundred of nanoseconds. Thus, applying a narrow time gate of about 10-25% of the longest stretch of the Newton sphere at the MCP detector allows for an exclusive imaging of the ion cloud central slice. Such images provide us with the full angular and recoil velocity distribution of the photofragments. Therefore, there is no need of using inversion methods to reconstruct the three-dimensional images. The slice of interest can be easily found by changing the timing of MCP until we get the images with largest radius. Although slice imaging was a significant progress in ion imaging field, due to using a fine grid as an extractor and pulsing the electric field in the acceleration region, the intrinsic high velocity resolution of the conventional VMI method was reduced. In 2003, Townsend et al.[47] introduced a new approach called "direct current (DC) Slice Imaging" where a lower voltage ratio between repeller and extractor was used to stretch the ion cloud temporally without the need of using a pulsed electric field. Since the lower electric field strength in the acceleration region could slightly reduce the velocity resolution, they added a couple of additional ion lenses to refocus the ion beam and thus recover the velocity resolution. According to their ion trajectory simulations in such ion optic design, the stretching mainly occurs between the repeller and first ion lens which makes it possible to be adapted to the instruments with shorter TOF tubes and smaller MCP detectors. With this new ion optic configuration the VMI method became more universal and applicable to most atomic and molecular fragments with any translational energy release.[101]

After acquiring images, the velocity of each component is extracted using a radial spectra to velocity calibration factor that is obtained by velocity map imaging of a well-studied fragment with known energetics.

The angular distribution of each component in a photofragment image can then be extracted by fitting the component to the following equation:[102]

$$I(\theta) = 1 + \beta P_2(cos(\theta)) \tag{2.11}$$

Where P_2 is the second order Legendre polynomial calculated by the following expression:

$$P_2 = \frac{1}{2}\left(3cos^2(\theta) - 1\right) \tag{2.12}$$

Here θ is the angle between the fragment' recoil direction and the laser beam polarization axis and β is the anisotropy parameter having two limiting values of -1 and +2 for pure perpendicular and parallel distribution respectively. A β value of zero correspond to an isotropic distribution of fragments which is an indicator of slow dissociation process compared to the molecular rotational period.[103]

2.8 Three dimensional Multi-Mass Coincidence Detection Setup

As discussed in previous sections, we have modified a conventional velocity map ion imaging spectrometer in our laboratory to acquire 3D multi-mass photo-ion images using a coincidence detection method initially introduced by Lee et al.[49].

In this approach, charged photofragments are focused onto a MCP detector using a VMI ion optic assembly in a DC slicing configuration[47]. The MCP detector acts as an electron multiplier where the intensity of each particle's hit is increased by several orders of

magnitude[104]. As the ions impinge on each detector's channel, the emitted electrons are ejected from the opposite side of the plates hitting a phosphor screen (P47) coupled to them which subsequently generates visible emissions (peaking at 400 nm). These bright spots on phosphor screen are observed by a CMOS camera (Basler ac-A720-520 um) and a single-anode Photo-Multiplier Tube (PMT) connected to a high-speed digitizer (NI PCI-5114) to collect positional and temporal information of ion spots respectively. Both camera and the digitizer are connected to the same computer. The data acquisition and analysis are performed through a program written in LabVIEW (National Instruments, version 2013, 64 bit) by Lee et al.[49] and modified based on our experimental requirements by Dr. Graham A. Cooper. In the data collection section, each camera frame is analyzed and the location of ion events which have an intensity higher than a specified threshold (the threshold is set based on the dark current) is centroided (center-of-mass calculations[101] written in C language and compiled as DLL) and recorded at each laser shot along with its intensity. The MCP timing gate (pulsed using DEI PVX-4150 pulse generator) can be set narrow enough to only acquire the central slice of one ionic fragment Newton sphere or wide enough to include all the produced ionic fragments at each laser shots. We have performed the experiments at both modes to acquire 3D coincidence multi-mass images or individual ionic fragment images.

The data acquisition program simultaneously records the TOF spectrum transferred from the PMT to the digitizer at each laser shot and a peak detection algorithm is used to find the location and amplitude of peaks for each spectrum. To make the coincidence algorithm more efficient the digitizer is triggered (synchronized) with the camera while the camera, the valve and the MCP are triggered with the laser system working at 1 kHz, although the

experiments were performed at 250 Hz due to the inability of the computer to keep up with the data collection at higher repetition rates.

After the acquisition data step, these data are inputted in an analyzing program where the number of events recorded by the camera and digitizer are compared on a shot-by-shot basis. The laser shots in which the number of recorded events is not equal for both sides (false coincident events), are skipped, otherwise, they are kept for further analysis (true coincident events). The correlation between the ion spot intensity recorded by the camera and the peak amplitude recorded by the digitizer is used to associate each TOF peak with an ion spot detected by the camera. If the matching between camera signal intensity and the digitizer peak amplitude shows a strong correlation, we move on to the next step which is the reconstruction of 3D multi-mass momentum images from the list of true ion events. This list of ion events includes 2-dimensional positional (X-Y spot coordinate on the detector) and temporal (arrival time of the ion at the detector) information of each event.

Acquiring multi-mass images is the necessary step in studying the fragmentation path of polyatomic molecules. To determine the dissociation dynamics of the system, it is crucial to find the correlation between the recoil velocity vectors of various pairs of ions produced from the same dissociative ionization/Coulomb Explosion event. Coincidence detection techniques have been the principal method in determining such correlations where the full momenta distribution of photofragments (photoelectron-photoelectron (PEPECO), photoelectron-photoion-photoion (PEPIPICO), photoion-photoion (PIPICO)) are detected in coincidence while the number of fragmentation events is kept lower than one to ensure that all fragments are produced from the same process.[105-108] For instance in an electron-ion coincidence experiment, a double sided TOF mass spectrometer is used where the

electrons and ions produced from the same fragmentation event are detected using two separate position sensitive detectors at opposite sides of the spectrometer. The ions at each laser shot are extracted and sent toward the ion detector after a delay of t_d only if an electron is detected in that specific cycle. The time delay t_d is short enough to assume that the extracted ion is produced alongside the detected electron from the same process.

Two-dimensional coincidence maps are then generated where the TOF spectra (or any variable of interest) of the electron-ion pair (ion-ion, electron-ion-ion) are plotted with respect to each other. These 2D maps reveal useful information on the dissociation dynamics which are not accessible from 1D TOF spectrum. The dissociation mechanism can be inferred from the structure of the cross peaks on the 2D coincidence maps. Peaks with a slope of -1 represent a two-body or a concerted dissociation pathway while a deviation from this slope is a result of a third fragment ejection or vibrational bending and stretching of the excited molecule.[108] This dependence of the cross peak slope and shape to the fragmentation mechanism will be explained later in this section.

In a coincidence experiment, as the number of events per experimental cycle increases, the number of false coincidences (coincidences/misassignment of uncorrelated fragments produced from different processes) increases. The background noise arising from such false coincidences blur the coincidence maps and makes it impossible to extract any useful information from them. Therefore, the key experimental condition for a coincidence experiment is to keep the number of events lower than one at each laser shot. Due to low count rate in coincidence techniques, it is important to operate the experiment at high repetition rates (several kHz) to accumulate the data and make the correlations statistically

meaningful otherwise the data acquisition time is comparatively long.[109] Also it is more favorable to use coincidence techniques for processes with large cross sections.

In strong field ionization where multiple fragmentation happens at each laser shot, the coincidence technique is unable to resolve the correlations. In such high-count rate regime, covariance map analysis is used.

The Covariance analysis is a statistical method that measures the linear correlation between two random variables. Originally, Frasinski et al.[110] applied this method to multiphoton multiple dissociative ionization data to determine the correlation between various TOF mass peaks with the motivation of removing the background noise arising from the false coincidences. In this method, the covariance values between all pairs of TOF peaks acquired at each laser shot are calculated and averaged over total number of laser shots (by calculating the covariance between the TOF spectrum and itself) yielding a covariance matrix which is then plotted as a 2-dimensional covariance map:[107, 110]

$$Cov(X,Y) = \langle (X - \langle X \rangle)(Y - \langle Y \rangle) \rangle = \langle XY \rangle - \langle X \rangle \langle Y \rangle =$$

$$\langle X(x)Y(y) \rangle - \langle X(x) \rangle \langle Y(y) \rangle \qquad (2.13)$$

$$= \frac{1}{N} \sum_{i=1}^{N} X_i(x) Y_i(y) - \left[\frac{1}{N} \sum_{i=1}^{N} X_i(x) \right] \left[\frac{1}{N} \sum_{i=1}^{N} Y_i(y) \right]$$

In this equation X and Y are the signals of interest, x and y are the coordinates of the covariance map (random variabl es), the angled brackets represent the mean (expectation) value of observables (over N laser shots). According to this equation, the covariance analysis calculates the difference between the correlated $\langle XY \rangle$ and uncorrelated $\langle X \rangle \langle Y \rangle$ products. A positive or negative covariance between two mass peaks implies that the fragments corresponding to the peaks are produced from the same dissociation channel.

Both axes in a 2D covariance map can represent the same variable (same TOF spectrum) which is called auto-variance (with a mirror symmetry) or two TOF spectra recorded simultaneously.[110] Figure 2.9 is an example of an "auto-variance" map constructed from TOF spectrum acquired in a Coulomb Explosion experiment of CO molecules. The positive feature in the diagonal line of an auto-variance map is called "auto-covariance" (variance) which arise from the fact that each TOF peak is covariance with respect to itself. On the other hand, each non-zero cross peaks represent a correlation between fragments corresponding to the TOF peaks and consequently a fragmentation channel.

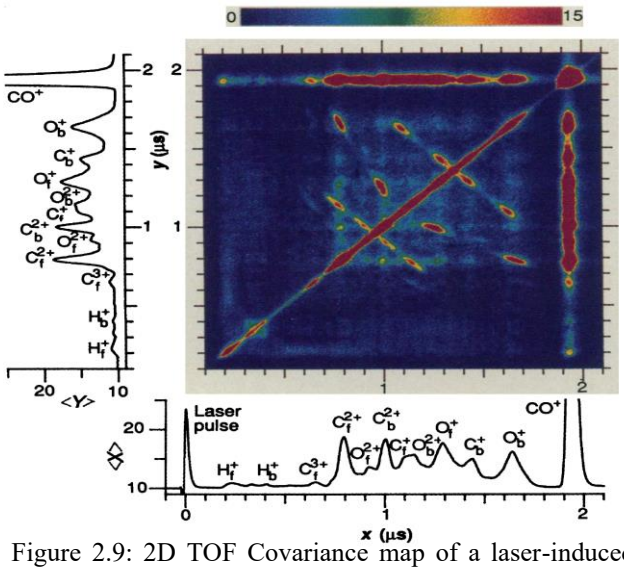

Figure 2.9: 2D TOF Covariance map of a laser-induced Coulomb explosion of CO. Adapted with permission from L. Frasinski, K. Codling and P. Hatherly, Science **246** (4933), 1029 (1989).©Sceince.

As explained for a coincidence map, here also the cross peak's structure gives information about the fragmentation channel. The velocity of the photofragments along the TOF axis (V_z) has two components: one given by the acceleration field (determined by the central location of the TOF peak) and one from the fragmentation process (determined from the TOF width):[107, 110]

$$V_z = \frac{2qU}{m} + V_0 cos(\theta) \tag{2.14}$$

Where U is the electric potential in the acceleration region, m and q are the photofragment mass and charge respectively, V_0 is the initial velocity of the particle given by the fragmentation process, θ is the angle between initial velocity and the TOF axis.

By a realistic assumption that the first term is much greater than the second term the width of each TOF peak can be calculated from the following equation:

$$\Delta t = \frac{xmV_0}{2qU} cos(\theta) \tag{2.15}$$

Where x is the ion flight distance. This equation shows that each peak has a width which is linearly proportional to the ion initial momentum along TOF axis. Therefore, the slope of cross peaks on TOF covariance maps gives the relative initial momenta of the corresponding pairs of ions along z axis (TOF axis). For example, momentum conservation requires a pure two-body dissociation process to produce two fragments with the same momentum magnitude flying in opposite directions resulting in a cross peak with a slope of -1 for such processes. In the case of three-body dissociation depending on the process mechanism a deviation from the two-body dissociation cross peak shape is observed. In

the case of concerted mechanism where the bonds rupture occurs simultaneously, the produced neutral fragment possess very little momentum and this has negligible effects on the charged fragments' trajectories.[111] In this case the cross peak still is similar to a two-body dissociation channel with a slope close to -1. In the case of two step mechanism (deferred and initial charge transfer) the deviation of the cross peak from a pure two-body dissociation gets more significant.

Although TOF Covariance mapping gives new insight into the reaction dynamics by providing the correlation between fragments' momenta along z axis, it does not give any information regarding the relative ions' momenta along other coordinates. To exploit covariance map analysis further, it has been coupled to 2D velocity map ion imaging.[112-117]2D Covariance imaging first showed by Slater et al.[114] has the potential of unraveling the multi-body dissociative ionization dynamics of complicated molecular systems. In this case the random variables are defined as the signal intensity changes of pixels in the two ionic fragment images whose correlations are investigated. One of the ions is assigned as a "reference" ion and the other as the "partner" ion. The covariance between signal intensity of each pixel in the reference ion image and all pixels in the partner ion image are calculated yielding covariance matrices for each pixel. By rotating and confining all covariance maps along a specified axis and summing them together (reducing the dimensions for simplicity), a recoil frame image is created where the velocity vector of the partner ion is shown with respect to the recoil direction of the reference ion. Depending on the structures we see in such covariance images we can infer the fragmentation dynamics with more details compared to what we could extract from conventional velocity map ion images and 2D TOF covariance maps.[118] If two ions are correlated then we expect to see

positive and negative features in the covariance image. The reason we see negative regions, is the fact that the covariance analysis calculates the signal variation in each pixel of the partner image with respect to mean when a signal in a specific pixel of the reference image is observed. Therefore, in the recoil frame covariance image in which the velocity vector of the reference ion image is rotated and restricted along a single axis, the probability of having signals arising from the partner ion in some specific area of the covariance image increases with respect to mean while other regions has less intensity than the mean.[107, 119, 120] Zhaunerchyk et al.[121] developed a method to correct for false correlations arising from fluctuating experimental parameters (partial covariance mapping) and showed the validity of the three-fold covariance mapping for variables with Poisson statistics (the variation of fragmentation events at each laser shot) by simply extending the two-variable equation. Their theoretical results showed that the four-fold covariance analysis based on the same extension is not valid.

Later Pickering et al.[118] extended the covariance imaging to three-fold correlations based on the Zhaunerchyk et al. formulation. Three-fold covariance can be calculated through the following equation:

$$Cov(X,Y,Z) = < XYZ > - < XY >< Z > - < XZ >< Y > \\ < X >< YZ > + 2 < X >< Y >< Z > \quad (2.16)$$

$$< XYZ \geq \frac{1}{N}\sum_{i=1}^{N} X_i(x)Y_i(y)Z_i(z)$$

Where N is the total number of laser shots, X,Y and Z are the observables (signal intensity of each pixel in this case), x,y and z are the pixel coordinates. Here, similar to two-fold covariance imaging, one ion is assigned as a reference ion and one as a partner, while the third ion is designated as a "constrained" ion. Again, a recoil frame covariance image where the velocity vector of the partner ion is plotted with respect to the reference ion is created where the third fragment is confined to recoil in a specific area of the image. This artificial 2-fold vector restriction ("reference" ion and the "constrained" ion) in three-fold covariance imaging can provide meaningful information regarding the fragmentation path and the molecular structure. If the structure observed in such images depend on the recoil direction of the third fragment it is indicative of a three-fragment correlation.

2.9 Time-Resolved Ultrafast Electron Diffraction (UED)

We have carried out a remote gas phase time-resolved experiment using MeV Ultrafast Electron Diffraction (UED) facility at the SLAC National Accelerator Laboratory (part of Linear accelerator Coherent Light Source user facility (LCLS)) to study the UV photodissociation dynamics of oxalyl chloride ($(COCl)_2$). The experimental setup shown in Figure 2.10 is described in this section.

In order to investigate the dissociation dynamics of oxalyl chloride at short and long time scales two sets of experiments at low and high electron charge modes were performed. In high charge mode, each electron bunch contains 20-30 k electrons (~2-5 fC) providing a total temporal resolution of ~500 fs while in low charge mode this reduces to 5-10 k

electrons (~0.5-2 fC) with ~200 fs time resolution. The electron beam is propagated with a relativistic energy of 4.2 MeV and little energy spread of 3-4 $\times 10^{-4}$ rms.

The gaseous oxalyl chloride enters the high vacuum chamber through a 500 µm orifice flow cell which is heated to 77° C to avoid the line clogging. A mass flow controller in the gas line is set below ~1 Torr to prevent the vacuum from tripping.

Part of the output of an 800 nm Ti:Sapphire laser system with temporal width of ~70 fs produces forth harmonic generation (200 nm, ~100 fs, ~300 µm) which is then used as the pump beam to induce excitation in the molecular gas. The third harmonic of the beam (266 nm) is used as the trigger pulse for S-band photocathode RF electron gun described elsewhere [122]. The laser and electron beams are propagated with a small angle of ~5° to

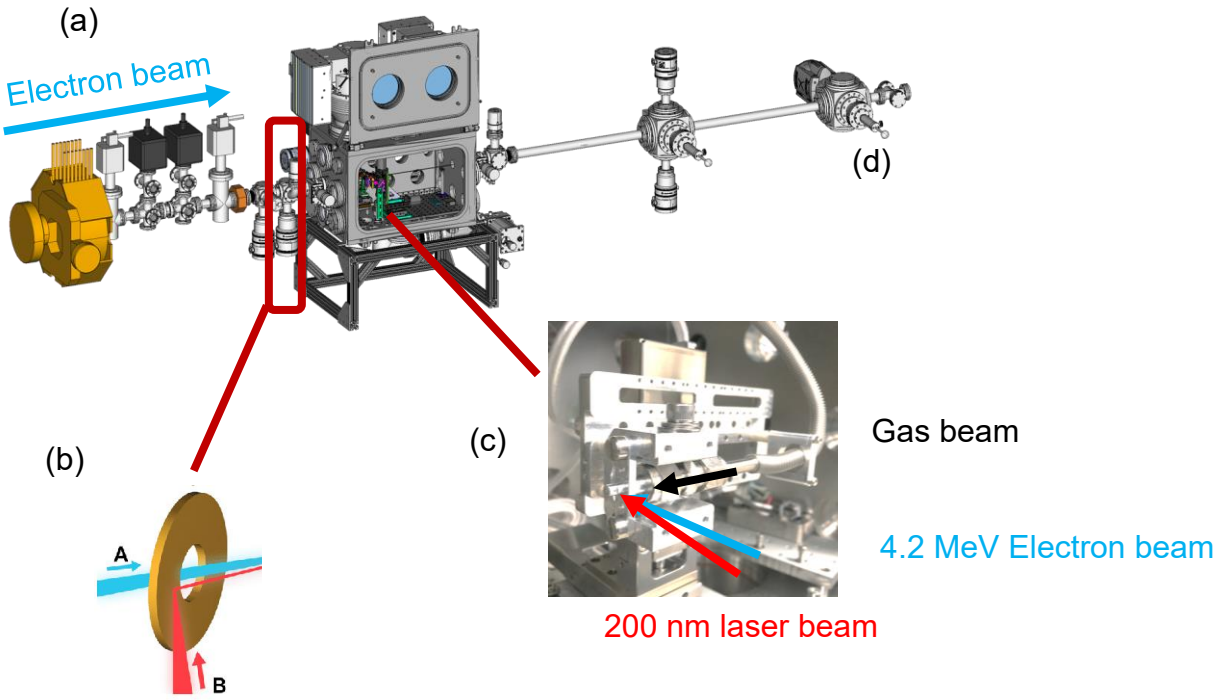

Figure 2.10: (a) MeV UED beamline Schematic Adapted with permission from UED, SLAC, LCLS. (b) incoupling mirror (c) interaction region inside the sample chamber. (d) electron detector (P43 phosphor screen) coupled to a charge-coupled device (CCD) camera.

minimize the velocity mismatch. The experiment was carried out at a 360 Hz repetition rate. The *s* (momentum transfer) to pixel calibration and time zero between laser and electron beam were obtained from well-known diffraction patterns of a single bismuth crystal.

A varying delay between pump and probe electron beams is applied to study geometrical changes in the excited oxalyl chloride molecules. High charge mode data sets were acquired at the pump powers of 10, 16 and 25 μJ (the power measured before the window). Here, since we are interested in single photon absorption dynamics, the data analysis is focused on lower powers data sets (10 and 16 μJ) where no signs of multi-photon contribution were observed in the diffraction data. All images in low charge modes were recorded at 16 μJ of the pump power.

In high charge mode, on average 40 delay points (up to 300 ps) with 200 fs-500 fs-5 ps-10 ps and 100 ps time steps with an approximate exposure time of 12 minutes for each delay were scanned. In low charge mode same number of delay points (up to 5 ps) was scanned.

The diffracted electrons at each delay are projected onto a phosphor screen (P43) and imaged using a charge-coupled device (CCD) camera. A small hole is drilled in the center of the detector to let the non- scattered highly focused electrons through and avoid the potential damage to the detector.

The pair distribution function (PDF) is then extracted from the acquired diffraction images which reflect structural changes of the system.

Chapter 3

Time of Flight Mass Spectrometry of Laser-Induced Plasmas

3.1 Introduction

Laser ablation plasmas have been investigated widely during last few decades. One of the main goals of these studies has been to develop laser ablation methods and laser induced plasma spectroscopy as a tool for elemental analysis[123-128]. An important application of studies in which laser ablation based analytical techniques have been used is to nuclear forensic investigations[129-131]. Laser ablation based mass spectrometry techniques are among the chief analytical approaches used in nuclear forensic investigations because they can provide highly accurate elemental and isotopic information while requiring less mass compared to alternative analytical methods available for such studies[132]. Direct characterization of actinide laser ablation plasmas has rarely been pursued, although it can provide conditions approaching those of a nuclear fireball. Such studies thus offer a tool for investigating reactions and condensation of materials relevant to nuclear forensics investigations.

Given that the internal temperatures of a plasma can be on the order of hundreds to many thousands of kelvins[133-137], understanding the dynamics of such systems can be challenging. Additionally, laser induced plasmas typically have a non-Boltzmann energy distributions, adding further complexity to any modeling of the plasma system[138]. Even though laser ablation is used in a number of fields, there are still significant gaps in the

understanding of how these ablation events progress. Plasma properties are typically experimentally studied either through optical emission spectroscopy or mass spectrometry methods. In optical emission spectroscopy methods, the produced plasma is studied directly during its ignition and initial expansion by recording the light emitted from the plasma which provides a fingerprint for both the species in the spectra and electronic temperature[139-141], while in mass spectrometry methods the plasma is studied using debris or soot collected from the plasma, providing insight into the species ultimately formed after the plasma has cooled[142-144]. Optical emission studies of the laser induced plasma are referred to as laser-induced breakdown spectroscopy (LIBS). There are a number of examples of this technique used to study the ablation of transition metals [145], inorganic materials[146] and alloys[147]. Although the focus is generally on atomic species, recently, Russo et al. have utilized LIBS to identify many spectral lines of diatomic molecules[148]. Through this, they were able to use the isotopic shift of these emission lines to characterize the abundance of different isotopes present in the plasma. However, this is only possible in plasmas with a well-characterized target and a small number of elements present due to the inevitable spectral congestion that would occur in a complex plume when detecting molecular emission. In the mass spectrometry technique, post ablation debris of the plasma is studied to understand its composition. Typically, this involves collecting the particulates from the plasma into a free jet or a molecular flow, cooling the particles in the process, and transporting the material to a mass spectrometer[149]. The most commonly used approach is laser ablation inductively coupled plasma mass spectrometry (LA-ICPMS) [150-155]. In comparing the two methods briefly, the principal difference is that such mass spectrometry-based methods do not provide any direct diagnostic information regarding the initial

plasma conditions, although they can give efficient elemental composition and isotopic ratio information. In contrast to this, optical emission-based methods can identify the conditions of the plasma. Furthermore, in nuclear forensic studies, using a portable LIBS unit is more time efficient and less expensive than a mass spectrometric approach[156]. However, such methods have lower detection sensitivity compared to mass spectrometry-based methods and show difficulty in identifying isotopic information of the species inside the plasma. The other significant drawback of LIBS methods is that they are limited to identifying the composition at early part of the plasma (around a few hundred ns), while the dynamics of the plasma evolution continues over a much longer period of time.

To overcome this, typically modern instruments combine both of these techniques together and work in tandem[157], which is extremely successful given the non-invasive nature of the emission spectroscopy detection. Nevertheless, there are some issues with this dual functionality set-up. Firstly, there is a cost to setting up a dual function spectrometer such as the iCCD cameras required for the capture of the LIBS emission and the vacuum system required for the mass spectrometer. Secondly, where the interest is in hot plasmas, conventional explosives or indeed a nuclear fireball, line broadening happens and results in a loss of information due to the overlapping of spectral features.

In this work, we present an alternative approach using a modified Wiley-McLaren Time of Flight (TOF) mass spectrometer[46, 158] to directly extract ions formed in the plasma during the ablation event. This setup is capable of overcoming many of the aforementioned issues whilst maintaining the principal advantage of LA-ICPMS which is observing dynamics in the plume over a much longer time period. With this instrument we were able to probe the plasma directly and extract translational energy distributions of the plume alongside its ion

composition. There are a number of challenges in attempting to extract ions directly from a plasma in this way. The biggest issue is that the plasma is so dense that high voltage extraction of ions causes massive space charge effects. This leads to a reduction in mass resolution of the spectrometer and can lead to potential damage of the ion detector. Also, as there is no resistance to the plasma expansion, the plasma maintains extremely high initial particle velocity which can blur the mass spectra. These technical challenges must be overcome to facilitate accurate ion detection, and the solutions we employed are discussed here. In this work, we used the aforementioned laser ablation-based mass spectrometry method to produce a high temperature uranium (U) plasma in order to gain insight into the chemistry of a nuclear fireball. Characterization of a U plasma using high laser power can provide useful nuclear forensic information: Isotope ratio characterization, and quantitative and qualitative analysis of radioactive samples. These signatures have been studied using LAICP-MS and LIBS techniques[159-161], however, these approaches do not probe the conditions of the expanding plume directly. In the present study, we extracted the plume through small apertures to gain direct access to the conditions in the plasma. Although this approach did not yield mass resolution adequate for isotope ratio analysis under high power ablation, it is complementary to the more established techniques in gaining direct access to ion charge state and translational energy distributions. Here, we first calibrated our mass spectrometer using Al and Gd solid samples and then performed the same experiment on U to investigate the hot actinide plasma properties.

3.2 Experimental Methods

The experimental apparatus has been introduced in previous chapter. Briefly, a mass spectrometer consisting of a main chamber where the laser ablation occurs and a TOF tube at the end of which a MCP/Phosphor detector is mounted, was used. An ion optic assembly with slightly modified Wiley-McClaren configuration (Chapter 2, Figure 2.2) is mounted in the main chamber to directly extract the produced plasma. The accelerator is pulsed after some time delay (extraction delay) to extract different regions of plasma (shockwave, reflected shock and the thermalized regions) and accelerate it into the TOF tube (Figure 3.1). The target is mounted in the main chamber on a two-dimensional translational stage to be evenly ablated as irradiated by the focused output of a ND:YAG laser system.

The TOF spectrum at each laser shot is collected directly from the MCP back plate through a home-built signal decoupler and transferred to a high-speed digitizer.

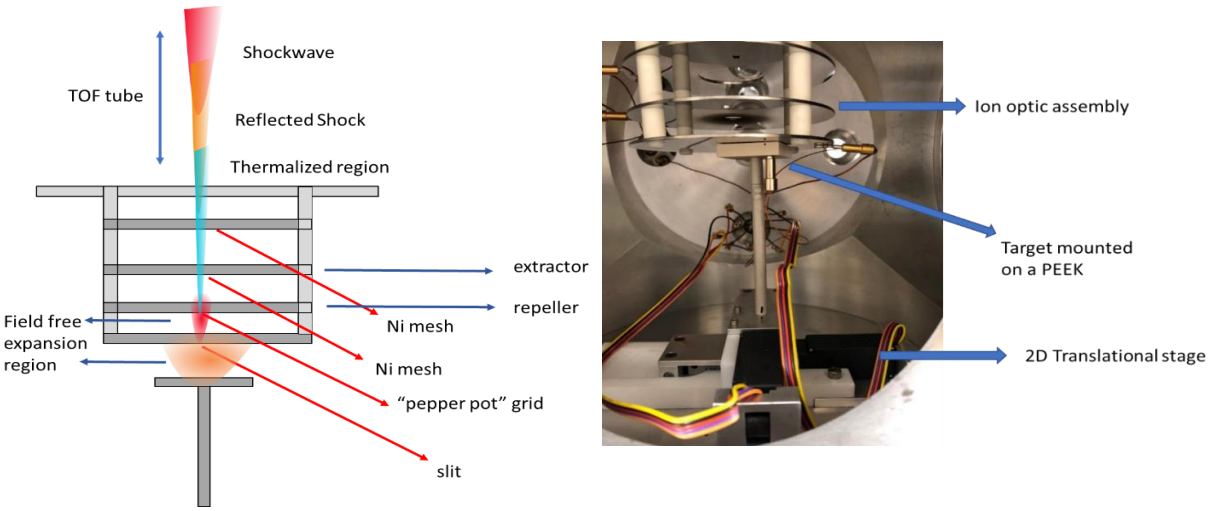

Figure 3.1: (left) The ion optics assembly and the target mount. Different regions of the plasma are shown at a given delay after irradiation. (right), The solid target mounted in the vacuum chamber on a two-dimensional translational stage below the ion optic assembly.

3.3 Results and Discussion

3.3.1 The Spectrometer Performance

To determine the overall performance of the spectrometer we performed laser ablation experiments on Al using 1064 nm at 30 mJ/pulse. The TOF spectrum of the Al target at an extraction delay of 6 μs is shown in Figure 3.2. The mass spectrum has been cropped to show only the singly charged Al^+ peak, however, the doubly charged Al^{2+} peak is present and found at 5.8 μs. The temporal width of the Al^{2+} peak is larger than typical single isotope mass peaks acquired from Wiley-McLaren spectrometer. The origin of this width can be understood by considering the dispersion of the initial translational energy of the particles within the accelerator acquired from the ablation process, and the range of velocities of the ion packet formed over the full length of the acceleration region. To model this, we reproduced our accelerator using SIMION 8.2[162]. In these simulations (Figure 3.3), we recorded the arrival time of a number of Al ions starting from 22 different positions within the accelerating volume in 1mm increments between the 2nd and 3rd electrodes (repeller

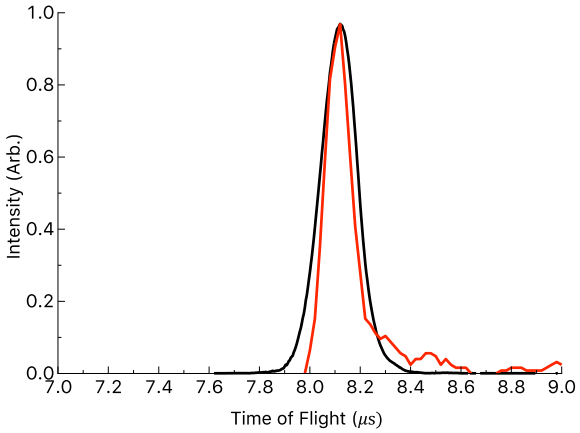

Figure 3.2: TOF mass spectrum of Al. The spectrum shown in black is the experimental spectrum and the spectrum shown in red is that produced from the SIMION simulations.

and extractor). The ions at each position were given a distribution of initial translational energy in the z-direction (along the TOF axis) centered on the energy required to reach their starting position within the accelerator in 6 μs. The FWHM of this distribution was also equal to the same translational energy (i.e., 100% spread) in order to model dispersion of ion energies within the accelerator. These (440 in total) ion trajectories were recorded and counted in bins of 20 ns. This built up a TOF profile of the Al ions in the plasma within the accelerator. A 5-point moving average smoothing was applied to account for the 100 ns rise time of our accelerator field ramping. The simulation, shown as the red curve in Figure 3.2, is in fair agreement with the experimental data.

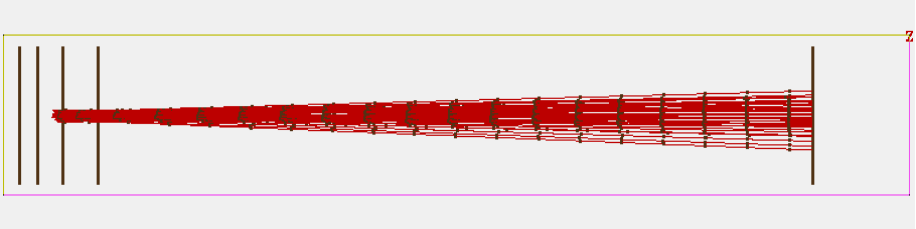

Figure 3.3: Ion trajectory simulation using SIMION 8.2. the red lines represent the trajectories with the positions of ions sampled (black dots) every 0.5 μs.

3.3.2 Gadolinium Ablation Results

In order to demonstrate the abilities of the apparatus and characterize the TOF mass spectrometer, we chose gadolinium (Gd) metal as the target. Gd was chosen due to its large number of isotopes at a high mass-to-charge ratio (around m/z = 157). This metal has also

been studied before using a combination of direct plasma extraction mass spectrometry and laser induced breakdown spectroscopy at vastly lower ablation energies than employed here[163]. Song et al. mounted a Gd plate directly onto the accelerator of the TOF mass spectrometer, in a manner similar that of most MALDI (Matrix- assisted laser desorption/ionization) type instruments. They demonstrated the ability to maintain isotopic resolution at this high m/z ratio under very low power of laser ablation and DC extraction of ions. However, in their study, the mass resolution was compromised even at moderate laser powers, and they did not investigate the plasma conditions at high power. Before recording the gadolinium TOF mass spectrum we investigated the mass loss of Gd via laser ablation at our high-power condition (30mJ/pulse) to estimate the particle density within our accelerator. To do so, the sample was ablated a number of times for an hour and the total mass removed was recorded. The mass loss was determined to be 63.1 ± 8.6 ng per laser shot. This is on the same order as that reported by Wen et al.[164] for a copper surface under similar ablation conditions, except that plume expanded against gases at atmospheric pressure. However, they noted the volume of material ejected was found to be independent of gas for He, Ne and Ar, so we do not expect this to be different for expansion into the vacuum. Our determination corresponds to 2.4×10^{14} atoms (or 0.4 nmol) ablated in a single shot. Assuming a hemispherical expansion, and that all the removed mass went into the initial plume, we calculate that the total density of the plasma before the first slit is ~1.4×10^{16} atoms/cm^3. We estimate that the total amount of material that passes through the first slit is approximately 4×10^{10} atoms per laser shot (about a 6 order of magnitude reduction in total number). Furthermore, we estimate that through the second slit (the pepper pot grid) the number of atoms is further reduced another factor of 10^3 to 4×10^7. At these reduced

densities we do not observe any Coulomb repulsion when extracting the ions from the plasma using the accelerator. To characterize our modified TOF mass spectrometer we performed a laser ablation experiment on a Gd sample using 1064 nm, 30 mJ/pulse. Figure 3.4 shows the extraction delay dependent TOF mass spectrum of the Gd plasma. The spectrum was recorded at delays from 0 to 60 μs in 0.5 μs steps. In addition to the two main expected signals at m/z = 158 and m/z = 79 of Gd^{+} and Gd^{2+}, there are a number of additional peaks in the data that vary as a function of extraction delay. These additional signals are identified as background gases ionized in the chamber by plasma species. This is most likely through either collisional ionization from charged species within the plume or from electron impact ionization during the acceleration process (with a maximum available energy around 300 eV). These signals generally appear at delays consistent with the thermalized region of the plasma except for m/z = 18 (water) and 40, which persist for much longer times. We assign m/z= 40 to argon, which is used in the production of Gd. This mass was also seen by Song et al. in their Gd ablation and curiously assigned to potassium without comment[163].

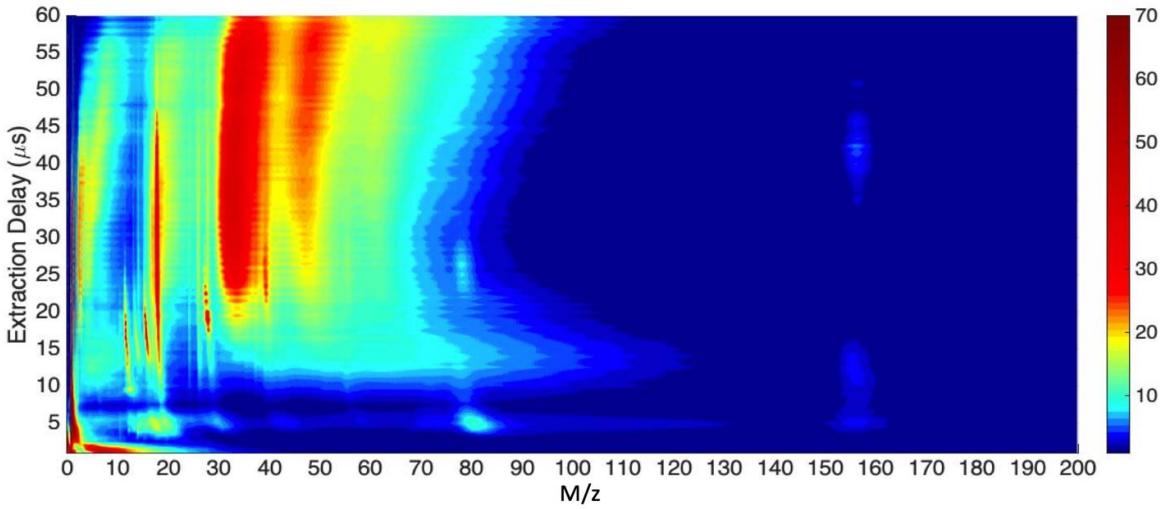

Figure 3.4: Extraction delay-dependent time-of-flight mass spectrum of gadolinium laser ablation plasma.

It seems that it is trapped in the foil giving signals that persist to much longer times than other background signals such as m/z = 28. It is interesting that the water signals also show a much longer appearance profile much like argon, perhaps suggesting some is also trapped in the sample. The data shows that prior to acceleration in the mass spectrometer, the Gd ions have three distinct arrival times centered at 5 μs, 12 μs and 42 μs, indicating a distribution of ion velocities within the plasma plume. We suggest that these three regions correspond to those ions found within the hot initial shockwave layer of the plasma (5 μs) which may be followed by a reflected shock from the back of the first electrode and some attenuation. Finally, there is the colder thermalized part of the plasma (42 μs). This cooling we suggest comes mainly from collisions within the plume itself behind the first aperture. The identification of the regions as either shockwave or partially thermalized is further supported by the data. The early time region (around 5 μs) has an intense non-Boltzmann distribution of Gd^+ and Gd^{2+} ions that would indicate a region of the plume that is extremely hot/energetic. It also has very high translational energy. The late time region identified as the thermalized core of the plume is supported by comparing the average translational kinetic energy of the Gd^+ to that of the background and will be discussed later in this section. Based on our initial measurement of the accelerator performance using the Al target, we would expect a significant reduction in the width of the G^+ peak as a function of extraction delay as the colder parts of the plume have lower translational energy dispersion shown exactly in Figure 3.5. Figure 3.5(a) shows the Gd^+ channel at 5 μs whilst 5(b) depicts the TOF signal at 45 μs. The data does not show any clear indication of the various isotopes of Gd, ^{154}Gd (2.18%), ^{155}Gd (14.80%), ^{156}Gd (20.47%), ^{157}Gd (15.65%), ^{158}Gd (24.84%), and ^{160}Gd (21.86%), but a small shoulder in Figure 3.5(b) spectrum is from ^{160}Gd. Previous

laser ablation studies of Gd have been able to identify these isotopes but with a different configuration mass spectrometer at significantly lower power, 1.2 MW/cm^2 previously compared to our 500 GW/cm^2. Once again, however, the simulations of the Gd^+ TOF spectrum are in fair agreement with what we record. The simulations were run in the same manner as for Al described above, but in this case, we ran the simulation for each isotope separately and scaled the results by their abundance within the sample. Therefore, we infer that the translational energy distribution within the Gd^+ at 5 μs and 45 μs are 40.6 eV, and 0.5 eV, respectively, roughly matching the spread of the translational energy of the particles within the accelerator based on the arrival time. The simulations do suggest that we should be able to resolve the ^{160}Gd isotope partially at 45 μs extraction delay, which appears as a shoulder in the experimental data. In addition to determining the spread of the translational energy within the accelerator using the width of the mass spectrum, the data in Figure 3.4 can also be used to determine the translational energy distribution of the plasma directly, by measuring the Gd^+ signal as a function of extraction delay. As we know the path length of the plasma prior to acceleration, we can calculate the velocity required for the ions to arrive in the accelerator at different times; this is in fact the same basis used for determining the translational energy distribution given to the ions in different regions

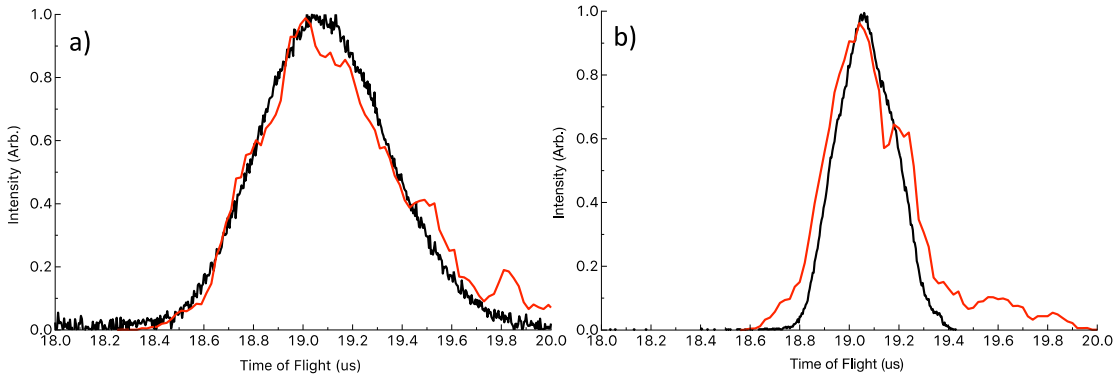

Figure 3.5: TOF mass spectra of Gd^+ at delays of (a) 5 μs and (b) 45 μs between laser ablation and ion extraction. The spectrum in black shows the experimental TOF and the simulation is in red.

in the accelerator in our SIMION simulations above. For Gd^+, the translational energy distribution obtained directly based on the field free flight times (i.e., extraction delay), and the one based on the peak width of the mass spectra, are in good agreement. In these simulations, we use a single ion position within the accelerator, the one at which the focusing of the ions onto the detector is optimized for our applied potentials, as our position to calculate the subsequent time of flight of the Gd^+ ions using the Wiley McLaren equations. The use of a single ion position is both to simplify the analysis of the SIMION trajectories and also to focus on the ions which will be readily detected by our apparatus. This is due to a) ions accelerated in regions away from the central volume will either not focus as tightly and been seen as a structureless background to the mass spectrum and b) due to the geometric constraints of the electrodes, ions are unlikely to have much transverse momentum to take them away from the central axis of the spectrometer. Additionally, in order to correctly fit the experimental data, we must apply a scaling factor of 0.75 to the calculated TOF. This correction may be due to plasma screening the full effective field of the accelerator, leading to a longer ion TOF (and contributing to some additional blurring of the TOF as mentioned above). The results of this simulation are shown in Figure 3.6. In panels 3.6(a) and 3.6(b) the experimental and simulated data are shown, while in panel 3.6(c) the translational energy distribution of the Gd^+ over the entire plume expansion is depicted. The simulation shown in this figure was produced by modeling the arrival time distribution in the field-free TOF axis with three Gaussians to correctly capture the intensity distribution of the particles. One of the key features of the simulation is a predicted curvature in the arrival time of the Gd^+ particles in the early time window. This bend arises from the fact that for the Gd^+ ions to arrive in the accelerator within such a short time, the

initial translational energy of the particles U_0 must be comparable to the translational energy given to them after acceleration. This curvature in fact, is a direct measure of the change in translational energy as a function of the field-free plasma flight time. Using this, a translational energy spectrum of the Gd^+ particles within the plasma is obtained and shown in panel 3.6(c). A scaling factor of t^3 was incorporated to correct for the Jacobian in the transformation of the intensity as a function of time to intensity as a function of translational energy. The translational energy distribution spectrum shows two main peaks. These are located around 0.55 eV and 6 eV, but the latter extends to well beyond 50 eV. After converting from energy to temperature, assuming this energy is placed in only a single translational degree of freedom, these regions correspond to translational temperatures of 1.2×10^4 K, 1.4×10^5 K and 8.1×10^5 K. Wen et al. simulated ablation of a

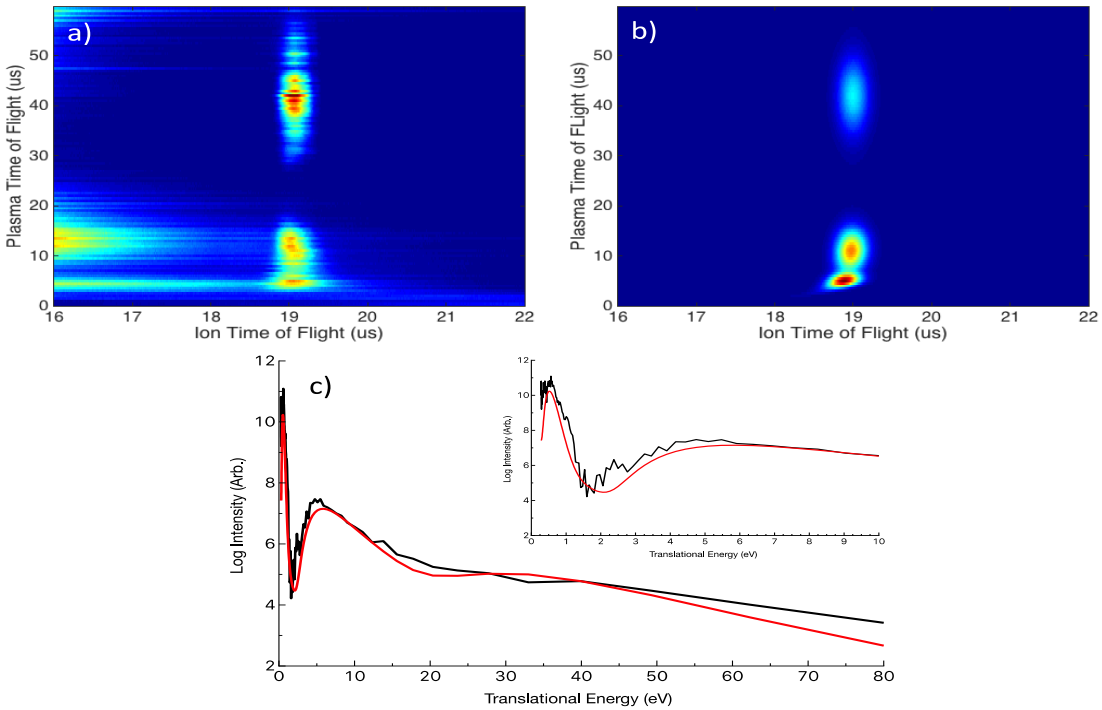

Figure 3.6: (a) TOF mass spectrum of the Gd^+ channel acquired at 30 mJ/pulse using a 1064 nm laser source. (b) Simulation of this data using the Wiley-McLaren equations. (c) Translational energy distribution of the Gd^+ channel over all extraction delays with the experimental distribution in black and the simulation in red. The inset in (c) shows the same distribution and fit between 0 and 10 eV.

copper surface against argon at atmospheric pressure under very similar laser conditions to those reported here. They observed the peak temperatures at the contact surface of the plume with the background gas to be 3×10^5 K, on the same order as that observed here. However, they found that this was somewhat in excess of experimental measurements, and assigned the discrepancy to omission of energy dissipating processes such as ionization[165, 166]. It is important to note that we do not see any evidence of ion cluster formation in any of our measurements. We believe that this is due to the fact that the plasma is too hot (translationally) and no such stable clusters are being formed under the conditions of our study. However, we have not employed any post ionization methods (such as an additional laser pulse to ionize neutrals in the plasma) in our current data, so we cannot infer any information about neutral cluster formation within the plasma that could be occurring as the plasma cools down.

3.3.3 Uranium Ablation Results

We now turn to the uranium plasma, which is the focus of these studies. To characterize the uranium plasma, we performed a laser ablation experiment with two different wavelengths, 1064 and 355 nm, and at different laser powers (3,10 and 30 mJ/pulse). Figure 3.7 shows the extraction delay dependent TOF mass spectra of uranium ions under these different ablation conditions. In this case the uranium surface was cleaned by prior ablation to be free of oxides. The two main features in all laser powers and wavelengths belong to U^+ and U^{2+} channels. Just as is the case in the Gd data, we see no signs of cluster formation. The TOF mass spectra obtained at different conditions show that the plume composition changes as a function of laser power and wavelength. At higher power the uranium signal becomes bimodal with ions arriving both at short and long extraction time

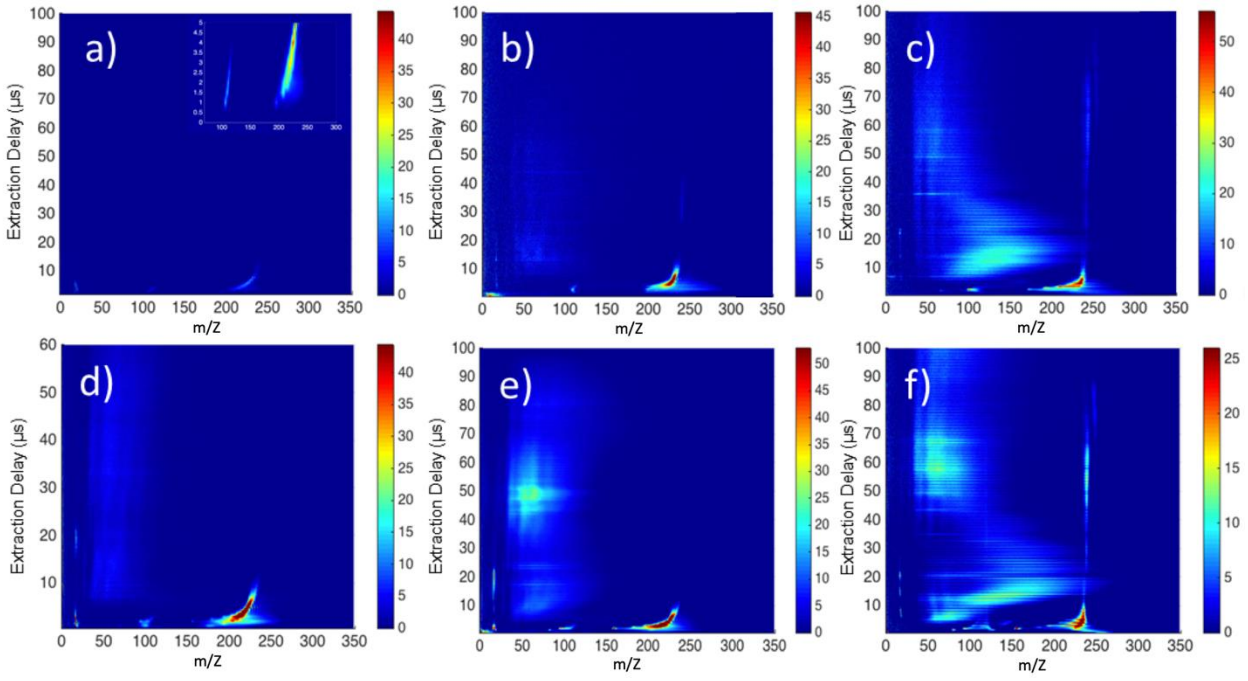

Figure 3.7: Extraction delay-dependent TOF mass spectra of uranium plasma. The 1064 nm ablation at 3, 10 and 30 mJ/pulse are shown in panels (a) to (c) and the 355 nm ablation also at 3, 10 and 30 mJ/pulse are shown in panels (d) to (f) respectively.

delays. In addition, we see an increase in background signals with laser power. The production of doubly charged uranium ions as well as background signals also increases at the shorter wavelength. We did not observe any evidence of separation of the two uranium isotopes because of the wide range of initial translational energies that the accelerator compresses as discussed further below. In all cases, the arrival time of the U^+ is the same if not slightly earlier than the Gd^+ suggesting that the uranium plasma formed in these conditions is much hotter, more energetic plasma. In either case we can assign the peak at 4 µs and 55 µs as belonging to the initial shockwave and the thermalized part of the plume, respectively. The translational energy of these two components were calculated to be 90 eV and 0.5 eV. Again, assuming energy partitioning into one translational degree of freedom this would indicate temperatures of 2.1×10^6 K and 1.1×10^4 K. Although the initial

impulse peaks at 4 μs, it begins to appear as early as 2 μs implying a kinetic energy that is much higher, up to 350 eV. The thermalized temperature agrees well with our calculation for the later component of the Gd^+ temperature. It is interesting to note that we do not see the contribution identified as a reflected shock in the U data. This could be due the reflected shock signal becoming merged with the initial shock and unresolvable, but more detailed modeling will be needed to confirm this. On comparing the uranium plasma signal in the late extraction delay region (>20 μs) we observe that a slower U^+ signal develops and grows more intense with increasing laser power. In addition, the distribution of the ions grows broader, visible over a much larger range of extraction delays. We attribute this to an increase in the fraction of the ions retaining their charge after passing through the high collision region before the first aperture on the accelerator. This would suggest a higher ratio of ion to neutral species in the plasma at higher ablation energies, consistent with the general picture that higher ablation energy leads to a hotter and more excited plasma. Figure 3.8 shows the U^+ mass peak obtained at different laser powers at 1064 and 355nm and the early extraction delay of 6 μs. Additional smoothing of the data was done in the case of 3 mJ/pulse to remove a ringing artifact from the data. At each wavelength the data is compared with a simulation (red curve) performed by SIMION 8.2 as explained before.

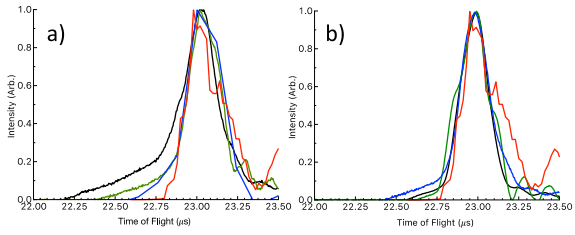

Figure 3.8: TOF mass spectrum of uranium plasma, ablated at 1064 nm (a) and 355 nm (b). In each plot we show results at three different laser intensities: 3 mJ/pulse (black), 10 mJ/pulse (green) and 30 mJ/pulse (blue). In each case the simulation is overlaid in red.

Here, to model the data, we consider a 15% dispersion of translational energy around each position in the accelerator, while for modeling Gd this was much larger. This suggests that this dispersion is more closely related to the spread in ion velocity at each position rather than spread in initial translational energy. This figure shows that change in the laser beam intensity does not change the overall peak width of the uranium signal significantly,

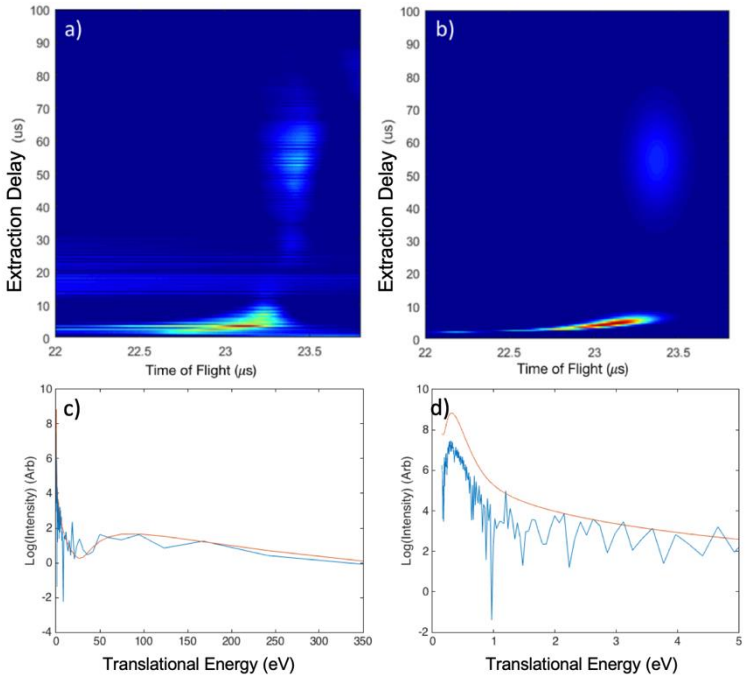

Figure 3.9: (a) Uranium mass spectra as a function of extraction delay (b) Simulation of the data in (a), (c) Translational energy distribution of U^+ over the entire plume expansion with the raw data in blue and the fit in red, (d) Expanded view of the distribution between 0 and 5 eV.

although there is a tail to shorter times (higher energy) that is especially apparent in the 1064 nm data. In addition, we see a narrower width for UV laser ablation compared to IR. In the U^+ channel we see a curvature at early times similar to the one observed in Gd^+ data but much more pronounced. Again, we ascribe this curvature to the initial velocity of uranium ions in the TOF direction adding to the imparted momentum gained from the

accelerator. The simulation was done using Wiley-McLaren equations as discussed above. Figure 3.9 shows the experimental and simulated delay dependent TOF mass spectra of the U^+ channel along with its inferred translational energy distribution over the entire plume.

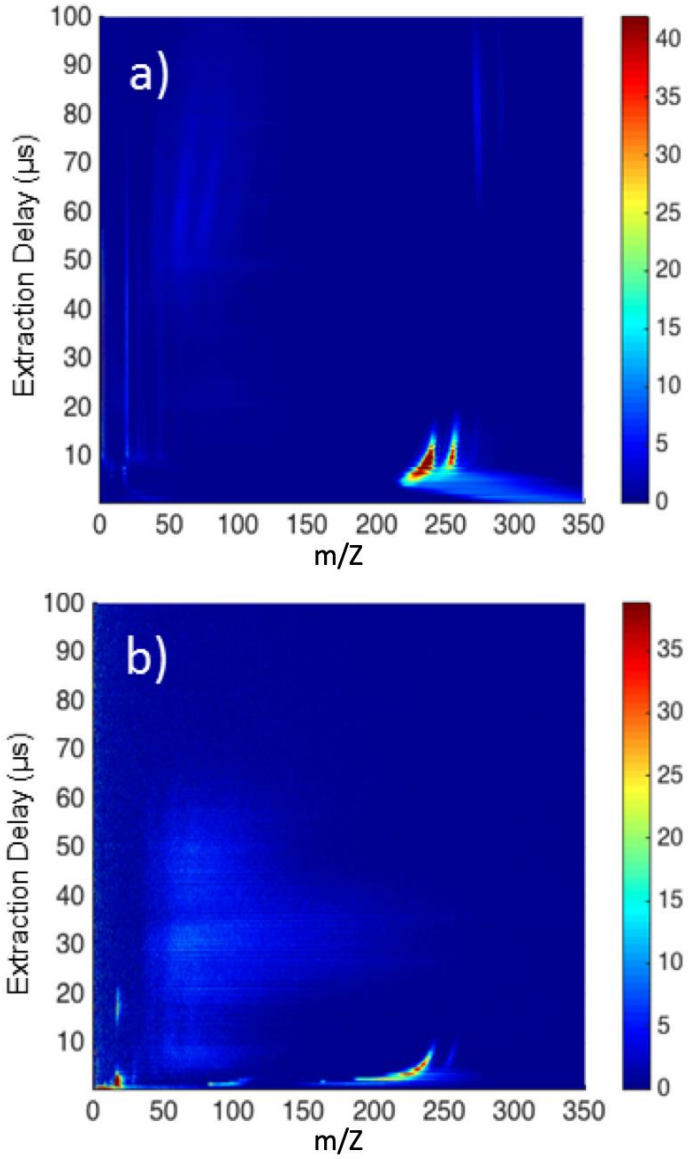

Figure 3.10: Delay dependent TOF mass spectrum of oxidized uranium metal. Ablation is performed at (a) 1064 nm and (b) 355nm. Laser power in both cases is 10 mJ/pulse.

The experimental spectrum is the same as that shown in Figure 3.8(c) but plotted in TOF rather than m/z ratio, over the region of the U^+ channel. Two Gaussians were used to model the intensity profile of the U^+ channel centered at 90 and 0.5 eV. The experimental data (in panel 3.9(a)) shows a very clear bend in the early plasma TOF, even more apparent than the Gd^+ in Figure 3.5, which is captured correctly by the simulation shown in panel 3.9(b). Panel 3.9(c) shows the translational energy distribution of the experimental and simulated data. The overall trend of the distribution is very similar to the Gd^+ results. While we do not observe the formation of clusters in the uranium plasma, we are able to observe the effects of oxidation on the metal surface. Figure 3.10 shows the TOF mass spectra of an oxidized uranium surface ablated with a 10 mJ/pulse beam of 1064 and 355nm (panels 3.10(a) and 3.10(b) respectively). In both cases we observe that the UO^+ is the dominant uranium oxide species observed with a small amount of UO^{2+} also seen in the 1064 nm data. The oxidized target plasma is broadly consistent with observations of the cleaned uranium metal plate with some minor differences.

The 1064 nm data shows no formation of U^{2+} at this laser intensity. In contrast, the 355nm data does show the production of U^{2+} but with a reduced amount of UO^+ present in the plume.

3.4 Conclusion

We have demonstrated a modified Wiley-McLaren Time of Flight mass spectrometer, designed to perform direct extraction of ions from an intense laser induced plasma at high ablation powers. This approach demonstrates our ability to identify the effects of various

experimental parameters on the plasma plume over a long period of propagation time. We examined the evolution of the plasma composition as a function of field-free time-of-flight of the laser plume and obtained a measure of the translational temperature of the plasma. We first characterized the performance of the system with Aluminum and Gadolinium targets combined with ion trajectory simulations. After characterization of the apparatus, similar sets of experiments were carried out with Uranium sample to study its energetic ablation plasma as a first step toward investigation of conditions approaching those of a nuclear fireball.

Chapter 4

Coulomb Explosion Dynamics of Thioesters

4.1 Introduction

The ability of Coulomb explosion imaging (CEI) to directly probe the structure of a molecule following multiple ionization by ultrafast methods has led to significant interest in both the technique itself and its application in time-resolved experiments[167-172]. In favorable cases, the molecular structure and dissociation dynamics can be inferred from the ionic fragments' momentum images recorded in a CE experiment. In order to acquire the full picture of the dynamics, it is necessary to determine the correlation between various fragments' momenta. This can be done using multi-mass imaging techniques along with correlation-based analysis methods. Developments over the past decade in time dependent imaging sensors such as the PImMS sensor have simplified the acquisition of multi-mass imaging data[112, 173-178]. However, it has been shown that multi-mass detection can be accomplished using fast cameras and digitizers in a coincidence detection setup, with advantages in both temporal and spatial resolution[179, 180]. In this chapter, we demonstrate that the 3D (time and position) coincidence detection approach is capable of successful CEI experiments for structural determination, holding promise for future pump−probe studies.

In the case of an ultrafast laser-induced CE experiment, since multiple molecules dissociate at each laser shot, to get the correlation between ion momenta we need to use statistical methods. Covariance imaging, first introduced by Hansen et al.[113] and Slater et al.,[114] is a useful statistical analysis method that can obtain such correlations. As explained in previous chapter, in this method, covariance mapping is coupled to three-dimensional ion momentum images[181] to produce covariance images.

The 3D multi-mass coincidence detection technique coupled to covariance imaging in a femtosecond laser-induced CE experiment enabled us to study the dissociation dynamics of two compounds belonging to thioester family (chlorocarbonylsulfenyl chloride and methoxycarbonylsulfenyl chloride) which show interesting double-ionization decay pathways[2]. Thioester compounds are related to many important biosynthetic reactions[182].

Chlorocarbonylsulfenyl chloride (ClC(O)SCl; hereafter CCSC) (Figure 4.1) is a synthetic reagent used primarily to create cyclic thioesters or for carbonyl coupling[183-185]. The structural and spectroscopic parameters of CCSC and similar compounds, and their photochemical behavior, have been studied multiple times over the course of several decades[186-195]. These have shown that the dominant conformer of CCSC is planar with the C=O and S−Cl bonds in a syn orientation[186, 191] and that it exhibits a rich photochemistry when exposed to ultraviolet irradiation[192]. Two studies have also previously examined the dynamics of ionized CCSC produced by valence and core synchrotron ionization[193, 195]. These showed that while $CCSC^+$ undergoes C−S, S−Cl, or C−Cl bond rupture processes to produce molecular fragments[195], removal of further electrons opens up a wide range of other fragmentation pathways with increasing degrees of atomization as the excitation energy increased[193]. These pathways from multiply ionized CCSC were identified through

ion−ion coincidence measurements, including several involving Coulomb explosions (CE), where multiple cationic fragments are produced and subsequently accelerated apart under the effect of electrostatic repulsion. In this study, we examine the energetics and dynamics of $CCSC^{n+}$ ($n \geq 2$) produced by strong field ionization.

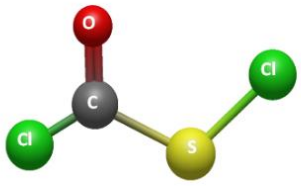

Figure 4.1: The most stable conformer of CCSC.

Methoxycarbonylsulfenyl chloride ($H_3COC(O)SCl$; hereafter MCSC) (Figure 4.2) is another compound belonging to sulfenyl carbonyl group showing multiple fragmentation channel as it interacts with a high intensity laser beam. The structural and spectroscopic properties of this molecule were reported previously by Erben et al.[190] through gas phase electron diffraction and low temperature X-ray diffraction. According to their experimental and theoretical results, this molecule has a planar backbone structure with a mixture of *syn-syn* and *syn-anti* conformers. Later, its dissociation dynamics was studied through electron-ion-ion coincidence time of flight (TOF) mass spectrometry by Erben et al.[196] They identified several dissociation channels following inner shell excitation using synchrotron radiation. These studies suggested interesting ionic decay pathways for our investigation

and provide a useful contrast to our approach, highlighting some of the advantages of the CEI method.

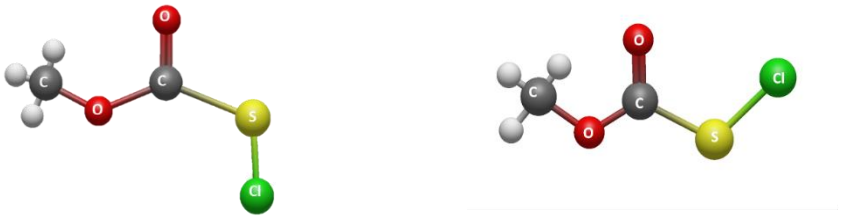

syn-anti conformer *syn-syn* conformer

Figure 4.2: The two most stable conformers of MCSC.

In the present study, we acquired ion momentum images of individual fragments as well as multiple fragments produced in a CE event induced by a femtosecond laser field in order to determine the correlation between their momenta. We then exploited covariance imaging analysis to determine both the energy and relative orientation of multiple fragments produced from the same dissociation event and extract meaningful correlations between various pairs of ions. *Ab initio* calculations were carried out to determine the starting structures. The results of these calculations combined with the experimental data were used to study the dynamics of the dissociative ionization processes. Here, we mainly aim to demonstrate the capability of multi-mass coincidence detection of our apparatus for future time resolved pump-probe experiments.

4.2 Experimental Methods

The detailed experimental apparatus and detection technique have been reported in Chapter 2. Briefly, the setup consists of a 3D multi-mass coincidence spectrometer (Shown in Figure 4.3) and a Ti:Sapphire laser system producing femtosecond laser pulses.

Both samples, CCSC (Sigma-Aldrich, 96%) and MCSC (Fisher, 97%) which are liquid phase at room temperature, are degassed and seeded in He (Airgas, grade 4.5) by passing the carrier gas through a bubbler containing the liquid sample. Then the gas beam containing ~1% of the sample is introduced into the source chamber through the piezoelectric disc valve with a backing pressure of ~500 Torr and opening time of 30 μs which is controlled by DEI PVX-4150 Pulser with timing from a BNC Model 577 Pulse Generator. The gas jet enters the source chamber at a resting pressure of ~10^{-7} Torr and passes through a 0.2 mm skimmer into the main chamber which is at a resting pressure of ~5×10^{-9} Torr.

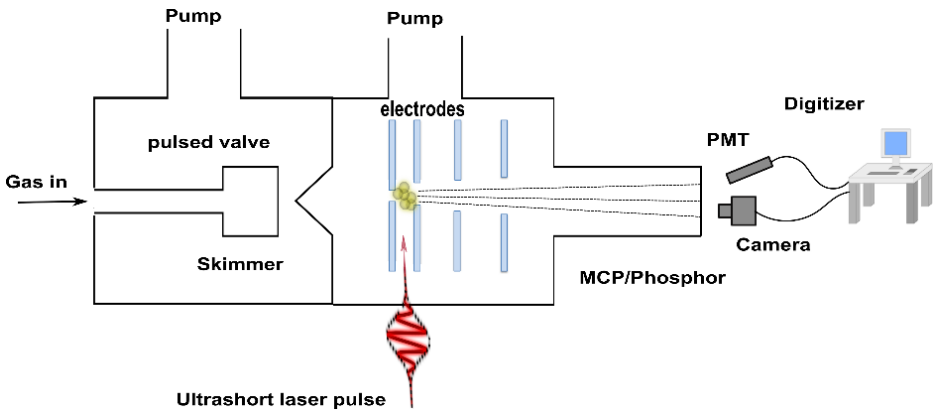

Figure 4.3: Schematic diagram of the experimental apparatus in CEI experiment.

The molecular beam is then intersected in the interaction region of a VMI electrode array by the ionization laser pulse which is the output of a KMLabs Wyvern-1000 Ti:sapphire laser (central wavelength of ~800 nm, temporal width of ~100 fs, ~2 mJ/pulse, 1 kHz repetition rate).

The experiments are performed at a ~250 Hz rate, limited by the speed of the PC collecting the data through the method described before. The power of the laser pulses was reduced using a combination of beam splitters and neutral density filters, before being focused into the vacuum chamber using a 25 cm lens to produce a strong field with intensities varying in the $7-20 \times 10^{13}$ W/cm^2 range.

This strong field ionizes the target molecules, producing ions that are projected onto the detector using VMI electrodes in a DC slicing configuration. The detector is gated to selectively detect the desired fragments (using another DEI PVX-4150 pulser), and the screen is observed using both a CMOS camera (Basler acA720-520um) and a photomultiplier tube (PMT) connected to a digitizer (NI PCI-5114), which are controlled using the same computer.

In the CCSC experiment images were acquired at a resolution of 480 ×480 pixels (260 ×260 pixel resolution at 1kHz) where a 75 mm diameter MCP was used. In the MCSC experiment the images were acquired at a lower resolution of 392 ×392 pixels due to using a smaller MCP detector (Beam Imaging Solutions, BOS40-6/P-47) with a 40 mm diameter. Here, due to the high intensity of signal at the center of the detector which arose from the ionized parent molecules and dissociative ionization events with close to zero translational energy, we masked this spot in order to better detect ion spots of interest which result from

CE events. We took care to adjust the position of the central mask such that it did not cover any signals with off-axis momentum.

For each experimental set, the coincidence detection technique described before was used to obtain a list of true ion events with both time and position data allowing for multiple fragments to be observed simultaneously by determining which fragment is responsible for each event detected by the camera.

Images were calibrated using the well-studied CE behavior of CH_3I[172, 178] under similar conditions, such that radial spectra could be converted to velocity distributions. These were subsequently transformed to fragment translational energy (fE_T) space, or, in the case of two body fragmentations, to total translational energy (E_T) space using conservation of momentum. Throughout this chapter, $p(fE_T)$ and $p(E_T)$ denote the fragment and total translational energy distributions, respectively.

4.3 Computational Methods

Supporting calculations for both molecules were performed at a density functional theory (DFT)[197, 198] level using the ωB97X-D functional[199] and Dunning's aug-cc-pVTZ basis set[200-202]. These consisted of optimizing the ground state geometry of the neutral parent molecule and relevant fragments and producing scans of electronic energy along various bond-stretching coordinates. These scans were also conducted on excited electronic states using time-dependent (TD) DFT[203-209]. CCSC and MCSC calculations were performed using the Gaussian 09 and 16W software package[210, 211] respectively.

Gas phase conformational equilibria of thioesters determines their properties on the ground and electronic excited states. The planar nature of these compounds result in syn and anti conformational forms[191]. The structural and spectroscopic studies of CCSC by several groups revealed that the most stable form of this molecule has a syn conformer (Figure 4.1) with less than 6% of anti form.[186, 191]

Erben et al.[190] performed quantum chemical calculations at a Density Functional Theory (DFT) level using the B3LYP functional[212, 213] and the 6-311++G** basis set to determine the minimum energy of four possible conformers of MCSC.

According to their theoretical calculations, two of these conformers (Figure 4.2) are the most stable geometries of MCSC: syn-syn (S-Cl and H_3C-C bonds synperiplanar with respect to C=O bond) and syn-anti (S-Cl synperiplanar and H_3C-C antiperiplanar with respect to C=O bond). The energy difference of these conformers was calculated and later confirmed by gas phase electron diffraction results which specifically gave the conformer ratio in the sample (72% / 28%). Here we used the same level of theory in order to compare our results with theirs. We successfully reproduced their results and then performed theoretical calculations using the more modern functional (including long-range and dispersion correction) and basis set (ωB97X-D functional and Dunning's aug-cc-pVDZ) to get the equilibrium distance of atom pairs in the optimized geometry of the parent molecule and other intermediate fragments.

4.4 Results and Discussion

4.4.1 Chlorocarbonylsulfenyl chloride (CCSC)

Figure 4.4 shows the distribution of fragments resulting from strong field ionization of CCSC at ~7 × 10^{13} W/cm^2, illustrating that the most intense product peaks (CO^+, S^+, and Cl^+) are those which would arise from cleavage of all the single bonds in the molecule (although other processes likely also contribute to their occurrence), while larger fragments are present in lower abundance. The intensity of the parent mono-cation peak is lower than expected, and peaks from $CCSC^{n+}$ ($n \geq 2$) are absent, due to reduced sensitivity in the center of the detector used, resulting in preferential detection of ions with off-axis momentum.

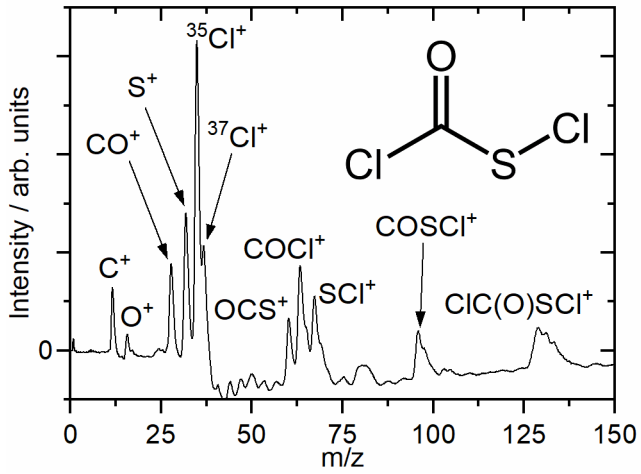

Figure 4.4: Time-of-flight mass spectrum resulting from strong field ionization and fragmentation of chlorocarbonylsulfenyl chloride (structure shown in inset). Spectrum is Jacobian-corrected and background-subtracted to show only intensity arising from species in the molecular beam. Inset: skeletal structure of the CCSC parent molecule

Images were recorded while gating the MCP voltages over each fragment ion separately; these are shown in Figure 4.5. The dark spot observed in the center of each image results from the region of reduced sensitivity mentioned above, arising from damage incurred prior to this project. Due to this damage, the experiment was subsequently repeated with a newer detector without this spot, and the corresponding images can be seen in Figure 4.6. These show similar results, although the images are at a different size and lower resolution (392 × 392) due to the smaller size of the replacement detector.

The major difference between the two sets of images is increased intensity in the area previously affected by the damaged spot, as expected. This intensity is primarily the result of dissociative ionization from $CCSC^{+}$ and would also be where $CCSC^{n+}$ and other non-fragment ions would primarily be observed at the corresponding delay times. Due to this damage, it is not possible in this study to comment on these low translational energy processes, that is, for fragment recoil speeds below 1.5-2 km/s. However, the processes of interest for Coulomb explosion, arising from multiply charged ions, tend to occur with higher off-axis velocities and these result in features less affected by the damaged spot.

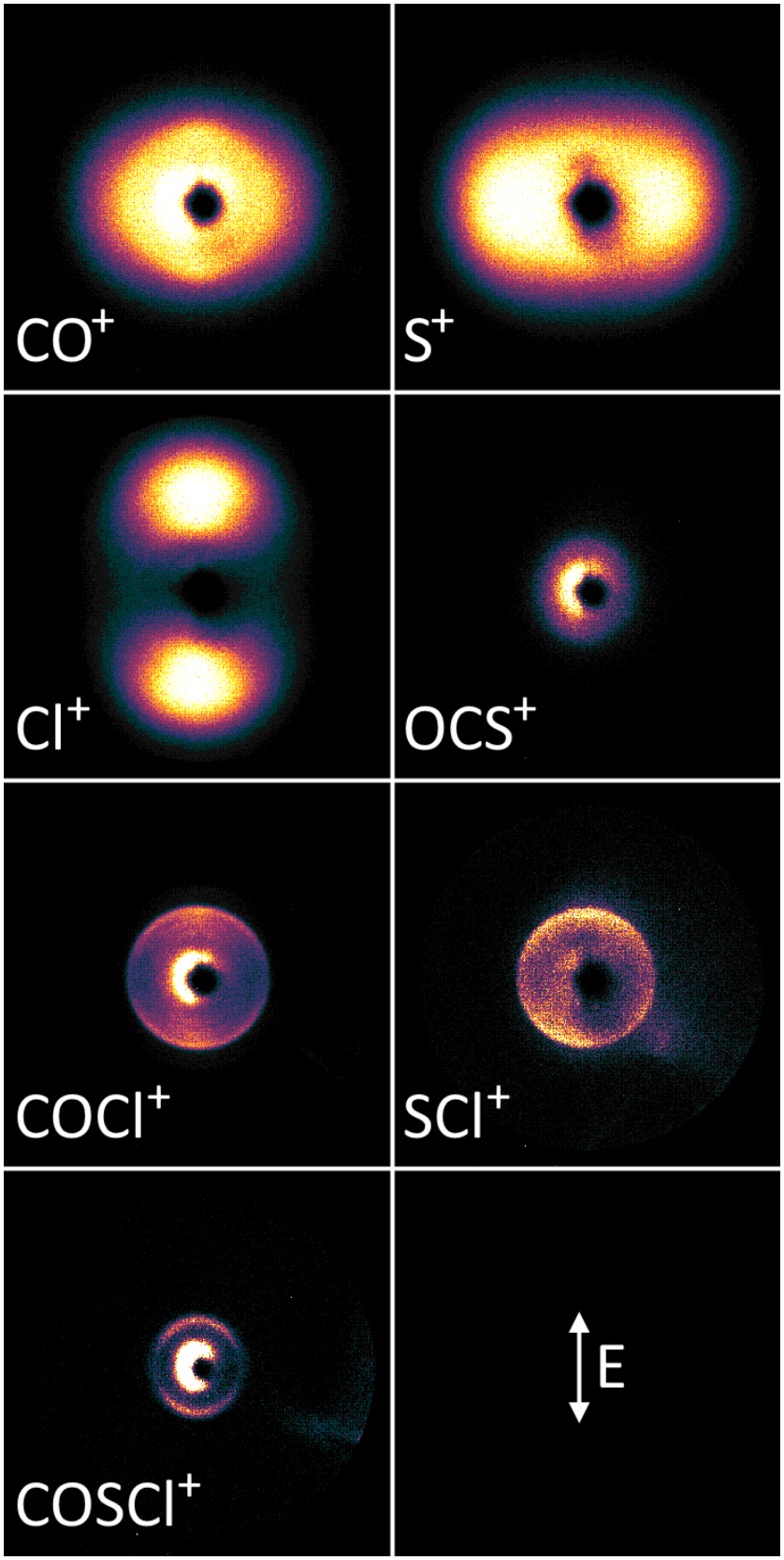

Figure 4.5: Velocity map images for individual fragments, as labelled, recorded with a field intensity ~70 TW/cm^2. The orientation of the laser polarization is indicated by the arrow in the bottom right panel.

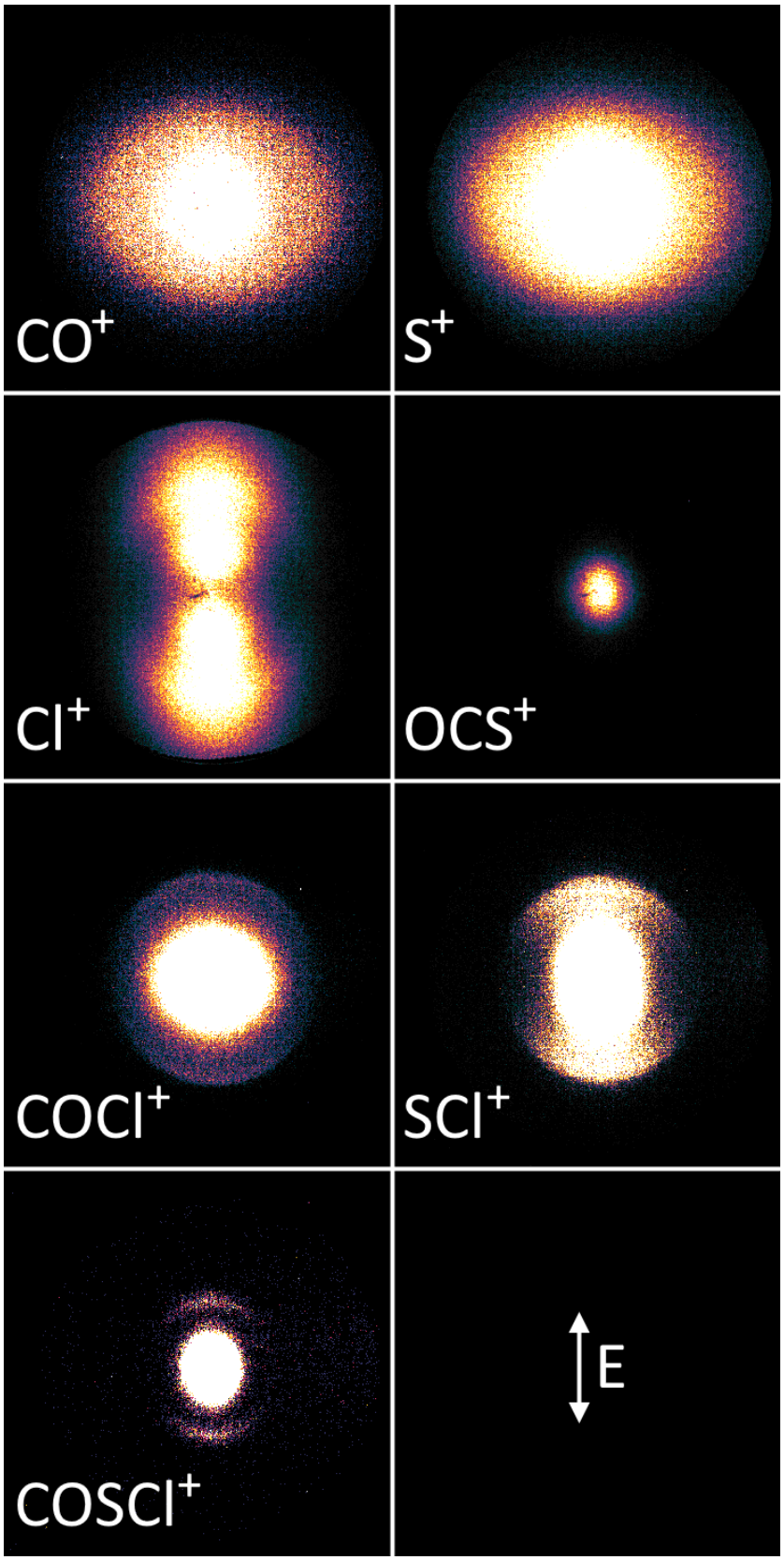

Figure 4.6: Velocity map images for individual fragments, as labelled, recorded with a field intensity ~70 TW/cm^2 with the new detector. The orientation of the laser polarization is indicated by the arrow in the bottom right panel.

When performing multi-mass coincidence experiments, it is impossible to resolve the positions of multiple ions observed too close temporally, which produce a single peak in the TOF spectrum but more than one spot on the camera. It was found that the data recorded with the newer detector, with the ability to observe extra events which would previously have fallen within the damaged area, caused the mismatch to occur more frequently, and steps needed to be taken to reduce the number of ions observed. These included manually obscuring the center of the image (using a piece of black tape) in order to block out ions with low off-axis momenta corresponding to non-CE dynamics, such that ions from the processes of interest with similar TOF could be successfully observed. Given these issues, as well as the reduced detector area and resulting decrease in camera image resolutions, it was found that the data collected with the damaged detector were superior for coincidence detection. While the damaged spot appears unsightly in Figure 4.5, the features of interest are not obscured, and the reduced sensitivity in this area was in fact a benefit, and thus all subsequent data analysis in this publication are based on those acquired with the older, larger detector.

Three fragments show clear rings in the images in Figure 4.5, most prominently $COCl^+$ and SCl^+. The central slices of these images were reconstructed using Finite Slice Analysis (FinA)[214], and the total translational energy spectra are shown in Figure 4.7.

The intensity close to the center of the images (obscured or blocked by the less sensitive area of the detector) results from dissociative ionization processes via $CCSC^+$. The rings in both images are momentum matched and correspond to the same peak E_T value of 6.1 eV when the features are assumed to arise from two-body fragmentation of $CCSC^{n+}$, suggesting t hey arise from the same fragmentation event shown below (process 1):

$$ClC(O)SCl^{2+} \rightarrow COCl^{+} + SCl^{+} \quad (1)$$

The rings shown in Figure 4.7 show significant anisotropy, with β_2 values from the FinA reconstruction of 0.6 – 0.8 indicating a parallel distribution. While the CO^+, S^+, and Cl^+ images (seen in Figure 4.5) show more diffuse intensity without clear rings, they likewise show anisotropic distributions, perpendicular to the polarization vector of the laser field in the first two cases and parallel in the latter. These features arise from the well-studied alignment effects in strong field ionization, where molecules are preferentially ionized when the molecular axis is oriented parallel to the laser polarization vector (geometric alignment), or where molecules are rotated by the field such that the axis points in that direction (dynamic alignment)[215]. Given the duration of the pulse, it is likely that there is a

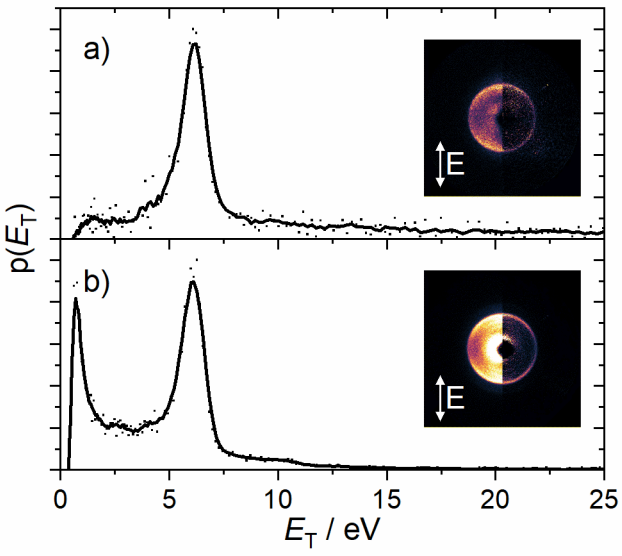

Figure 4.7: Translational energy spectra from FinA-reconstructed images of (a) SCl^+ and (b) $COCl^+$. E_T values were calculated using momentum conservation assuming $COCl^{0/+}$ and $SCl^{0/+}$ co-fragments respectively. The dots indicate the raw values, with the lines representing a 5-point running average. Inset: VMI images corresponding to the displayed spectra, with the raw image on the left and the reconstructed central slice on the right; the arrows indicate the direction of the laser polarization.

significant dynamic alignment effect, but the exact nature of the observed alignment is not certain.

The observed images indicate that the molecule is preferentially ionized with the axis along the molecular backbone (between the terminal Cl atoms) parallel to the polarization of the laser field. For processes (1), this results in the product ions travelling primarily parallel to the polarization vector. For the Coulomb explosions of more highly charged $CCSC^{n+}$ which substantially contribute to the smaller fragment images (as examined below), the observed anisotropic distributions arise from the Cl^+ ions being propelled along the molecular axis while CO^+ and S^+ are pushed to the sides by electrostatic repulsion.

To confirm the assignment of process (1), the multi-mass imaging capabilities of the experiment were utilized to simultaneously observe fragments in the mass spectrum (seen in Figure 4.4) between CO^+ and $COSCl^+$, inclusive. From these, the covariance maps for the relationship between pairs of fragments were calculated using the process described in Chapter 2.

The covariance maps are calculated between pairs of 'reference' and 'plotted' ions which show where the plotted ions are more likely to be seen in a frame in which the reference ions are oriented along a specified axis from the center (here always vertically upwards). The map for covariance of $COCl^+$ referenced to SCl^+ was calculated and is shown in Figure 4.8(a). A very sharp feature centered around 180° is observed in both this map and the reverse case, indicating that there exists a two-body fragmentation producing these ions. Given that these features are observed at the same radii as the rings shown in Figure 4.7, this confirms that process (1) (C–S bond cleavage from $CCSC^{2+}$) is responsible for these

rings. Covariance of Cl^+ referenced to $COCl^+$ is shown in Figure 4.8(b) to facilitate comparison, but this will be discussed in the three-body section below.

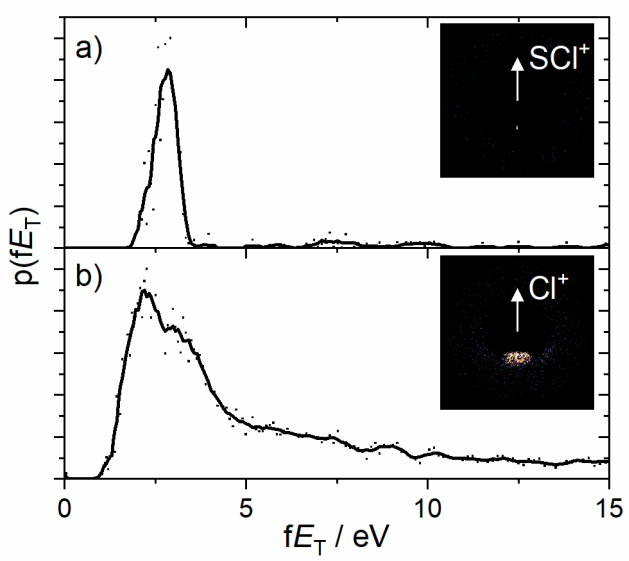

Figure 4.8: Fragment translational energy distributions from covariance maps of $COCl^+$ referenced to (a) SCl^+ (within angles of 176 – 183° to the reference ion vector) and (b) Cl^+ (at 144 – 216° angles). Points represent raw data while the lines indicate the five-point running average. Insets: the covariance maps from which the spectra are extracted, with adjacent pixel smoothing and arrows showing the orientation vector of the reference ion.

Computational scans were conducted along R_{C-S} for $CCSC^{2+}$ in the lowest-lying singlet and triplet states, as shown in Figure 4.9 (additional curves are shown in Appendix A (Figure A1) for further excited states). These illustrate that the two lowest energy singlet states are dissociative along this coordinate, with little or no barrier to fragmentation. The difference in energy between the parent di-cation states in the neutral ground state

equilibrium geometry and the relaxed products of process (1) in the lowest spin-allowed electronic states are 6.6 or 6.3 eV from the triplet or singlet states respectively, which agrees well with the E_T value of 6.1 eV observed from the images in Figure 4.7. These calculations thus suggest that these rings arise from C–S cleavage after ionization to ground or low-lying states of $CCSC^{2+}$, driven by Coulomb repulsion between the product fragments. A simple model treating the product ions as simple point charges moving only under electrostatic repulsion would predict E_T = 7.8 eV, significantly higher than both the DFT treatment and the experimental value. This may arise from multiple contributing factors: firstly, the bonding forces in the di-cation may have a non-negligible impact, requiring additional energy to overcome. However, it is also possible that the difference may arise from distortion of the molecule during the process of ionization; previous studies have observed experimental energy releases substantially lower than those expected from pure Coulombic repulsion, potentially attributed to stretching during ionization[216, 217]. The difference is less significant than that observed in those cases, potentially due to the shorter laser pulses and thus reduced time for deformation. This bond stretching can be driven or selected for by the nature of the ionization process, where increasing bond length can decrease the ionization threshold[218].

The third image in Figure 4.5 shows a clear ring at m/z = 95 corresponding to either Cl–C(O)–S^+ or C(O)–S–Cl^+, which arises from loss of a single Cl atom at either end of the molecule. However, the two potential fragments produced by C–Cl and S–Cl cleavage cannot be distinguished by TOF and thus either or both may contribute to the image. This image, and the corresponding E_T spectrum, is shown in Figure 4.10, where the central intensity again arises from dissociative ionization via $CCSC^+$, and the faster ring at 5.1 eV

seems likely to arise from Coulomb-explosion loss of Cl^+ from the di-cation shown below (process 2):

$$ClC(O)SCl^{2+} \rightarrow COSCl^+ + Cl^+ \qquad (2)$$

This ring shows similar anisotropy to those in Figure 4.7, with a β_2 value of 1.1, for the same dynamic alignment reasons. A similar covariance map to that in Figure 4.8(a), showing a sharp feature centered around 180°, was found for $COSCl^+$ referenced to Cl^+, as shown in Figure 4.10(b). The radial spectrum shows that this feature peaks at similar radii

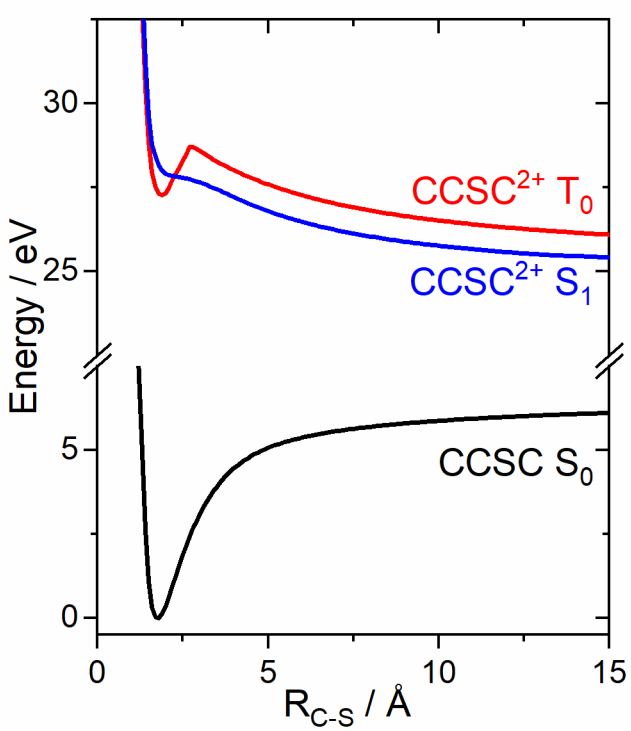

Figure 4.9: Potential energy curves for CCSC along the C–S elongation coordinate in the neutral ground state (black), triplet ground state of $CCSC^{2+}$ (red), and lowest-lying singlet state of $CCSC^{2+}$ (blue), calculated at the ωB97X-D/aug-cc-pVTZ level. All other coordinates were fixed at their values from the ground state neutral equilibrium geometry.

to the ring in the images shown in Figure 4.10(a), confirming that process (2), the loss of Cl^+ from $CCSC^{2+}$, gives rise to this feature. The reverse map does not show any significant structure, suggesting the fraction of Cl^+ arising from this channel is a small fraction of the total, such that it is not resolved in the calculated map. A comparison of the intensity of the number of Cl^+ ions observed in the image in Figure 4.5 to the number of counts in the ring in Figure 4.10(a) suggests that this channel accounts for less than 0.5% of Cl^+ ions observed, supporting this assertion.

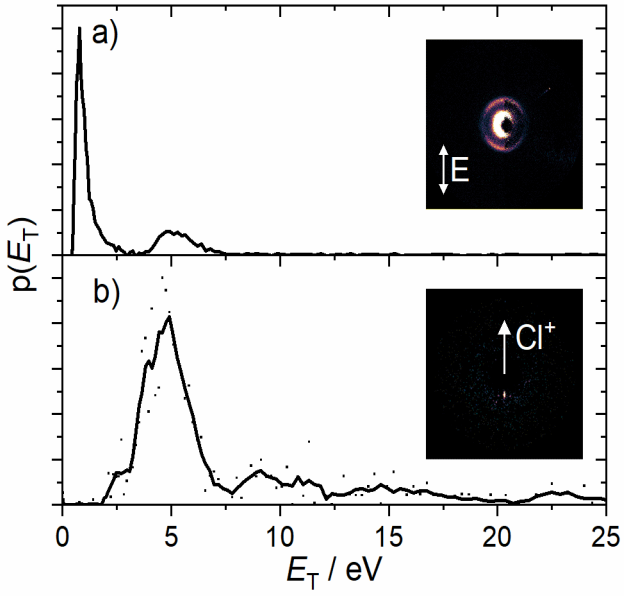

Figure 4.10: Translational energy spectra (assuming a $Cl^{0/+}$ co-fragment) from (a) the FinA-reconstructed image of $COSCl^+$, shown in the inset (with the raw image on the left and the reconstruction on the right; the arrow indicates the laser polarization orientation) and (b) the covariance map of $COSCl^+$ referenced to Cl^+, gated over angles 177 – 183° to the reference vector, shown in the inset (with adjacent pixel smoothing; the arrow indicates the direction of the reference ion). Points indicate raw data, with a five-point weighted average shown by the line.

It remains ambiguous which Cl atom is lost in this process, and similar potential energy curves to those shown in Figure 4.9 were calculated along $R_{C–Cl}$ and $R_{S–Cl}$, as shown in Appendix A (Figure A2). The computed curves show that relative to the triplet ground state

of $CCSC^{2+}$ at the starting geometry, the relaxed products of C–Cl and S–Cl cleavage are 2.9 and 1.2 eV lower in energy, respectively, with corresponding barriers to dissociation of 1.5 and 2.8 eV (the maximum energy releases from the lowest singlet state are reduced to 1.2 and 0.0 eV). The low-lying states studied via TD-DFT also show barriers along these coordinates. The fact that the translational energy measured for the process is noticeably higher, at 5.1 eV, and that the di-cation ground state is bound with respect to Cl-loss but not C–S cleavage, suggests that process (2) instead results from ionization to an excited state which preferentially loses a Cl^+ ion, rather than the singlet ground state which is likely to promptly follow the pathway of process (1). While C–Cl cleavage results in the more stable product ion, further computational work at a higher level of theory beyond the scope of this work would be required to identify the excited state which best explains the observed behavior in order to determine conclusively which Cl atom is lost.

In order to identify further fragmentation pathways of $CCSC^{2+}$, covariance maps were calculated between other pairs of ions. The map of $COCl^+$ referenced to Cl^+ shows a particularly significant feature, centered around 180° but broader than those observed for the two-body dissociations described previously. This is accounted for by the additional momentum of the unobserved third fragment. This map, and the corresponding fragment translational energy spectrum, are compared in Figure 4.8 to the map and fE_T spectrum from $COCl^+$ referenced to SCl^+ (i.e., resulting from process (1)).

These spectra show that the radial profiles of the two features are similar but distinct; process (1) produces a sharp peak at 3.1 eV, while the spectrum in Figure 4.8(b) shows a broader feature peaking at 2.4 eV but which is relatively flat in the 2.1 – 3.6 eV range (the higher background level at higher radii results from a lower signal to noise ratio in this map

as it corresponds to a lower proportion of the $COCl^+$ ions). Given the lack of data on the momentum of the third fragment ($S^{0/+}$), it is impossible to convert this to total E_T, but the range of angles observed in the covariance map allow for some limits to be placed on the possible values. The observed feature covers the angles 145 – 180°, so given this and equations for conservation of momentum (equation 4.1), a lower bound can be placed on E_T of 4.1 – 8.4 eV. Here the lower bound corresponds to the slower $COCl^+$ ions at 2.1 eV with an angle to the reference vector close to 180° and the upper bound corresponds to an fE_T of 3.6 eV and angles closer to 145°.

$$m_{COCl}V_{COCl} = m_{Cl}V_{Cl}sin(\theta) + m_SV_Ssin(\varphi) \qquad (4.1)$$

$$m_SV_Scos(\varphi) = m_{Cl}V_{Cl}cos(\theta)$$

This lower bound occurs when the angle between the sulfur and chlorine momenta is acute, and the actual total translational energy could be higher. DFT calculations suggest an overall change in energy from the T_0 or S_1 states of $CCSC^{2+}$ of only –0.2 or –1.1 eV for process (3),

$$ClC(O)SCl^{2+} \rightarrow COCl^+ + S + Cl^+ \qquad (3)$$

Given the large translational energy observed experimentally, compared to the small energy release for this process, two plausible explanations arise. The first is that strong field ionization accesses one or more excited states of $CCSC^{2+}$ which are 5 – 10 eV above the di-cation ground state, similar to but higher in energy than the states responsible for pathway (2), which undergoes dissociation along this pathway; the second involves the removal of an additional electron by the laser field to reach $CCSC^{3+}$, which promptly produces $COCl^+$, S^+, and Cl^+ with a calculated release of 10.8 eV of energy in process (4),

$$ClC(O)SCl^{3+} \rightarrow COCl^{+} + S^{+} + Cl^{+} \quad (4)$$

To examine the possibility of the tri-cation assignment, the three-fold covariance analysis described by Pickering et al. was used[174]. This approach yields a map analogous to that in Figure 4.8(b) with the added constraint that an S^{+} ion must also be observed in the same camera frame; the relative orientation of this third ion with respect to the reference can also be constrained.

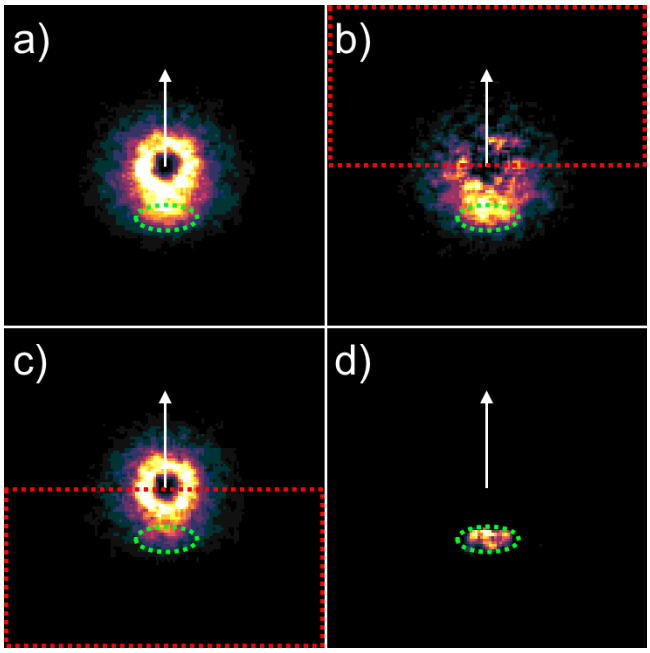

Figure 4.11: Covariance maps for $COCl^{+}$ referenced to Cl^{+} (the orientation of which is indicated by the arrows). (a) Three-body map with no constraints on position of the third ion, S^{+}; (b) & (c) three-body maps with S^{+} constrained to the areas within the red boxes; (d) two-body map without any S^{+} requirement. The green ellipses indicate the same area in all images and all images use adjacent pixel smoothing. Images are scaled independently.

These maps are shown in Figure 4.11; note that they are calculated at reduced resolution due to the prohibitive time costs of the calculations at full resolution. Figure 4.11(d) shows how the map from Figure 4.8(b) appears at this resolution, and this map bears a significant resemblance to that in Figure 4.11(b), featuring intensity in the same region shown by the

green ellipse. This intensity is also present in panel (a) but is absent in (c). This behavior, with the same feature appearing in the 2- and 3-body maps but being dependent on the constraints placed on the third ion, is in keeping with that expected for a three-body dissociation featuring all three ions, strongly suggesting that process (4) is responsible for the feature observed in the two- and three-fold covariance maps.

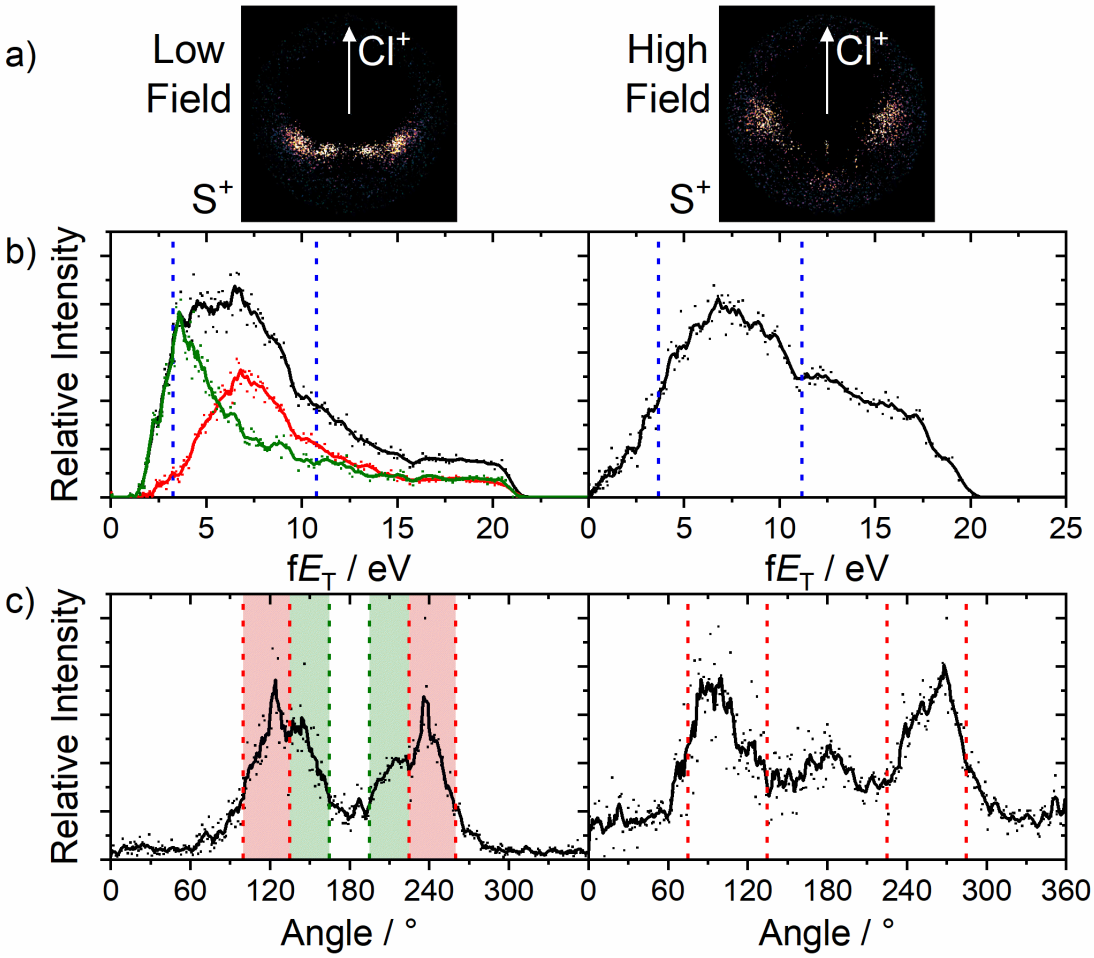

Figure 4.12: (a) Covariance maps for S^+ referenced to Cl^+ in weaker (left) and stronger (right) laser fields, with adjacent pixel smoothing and arrows indicating the orientation vector for the reference ions; (b) fE_T distributions corresponding to the above maps within the angular ranges indicated on the lower panels. In the left hand column, the red and green lines correspond to the ranges highlighted in the bottom panel, with the black trace the total across both ranges; (c) angular distributions for the respective images within the radial ranges indicated in blue on the middle panels. Points represent raw data while the lines are five-point running averages.

Other anisotropic features were observed in covariance maps calculated between other pairs of fragments, but in most cases the signal-to-noise ratio in these features is not sufficient to enable proper analysis. However, they strongly imply the existence of other potential exit channels from the di- and tri-cation of CCSC. One other map which shows a strong covariance pattern is that of S^+ referenced to Cl^+. This is compared in Figure 4.12 to the corresponding covariance map when the intensity of the laser field was raised to 2×10^{14} W/cm^2 in order to increase the average charge state reached by the CCSC molecules. This change resulted in the number of smaller fragment ions (CO^+, S^+, and Cl^+) increasing relative to the larger molecular fragments, and doubly ionized products also being

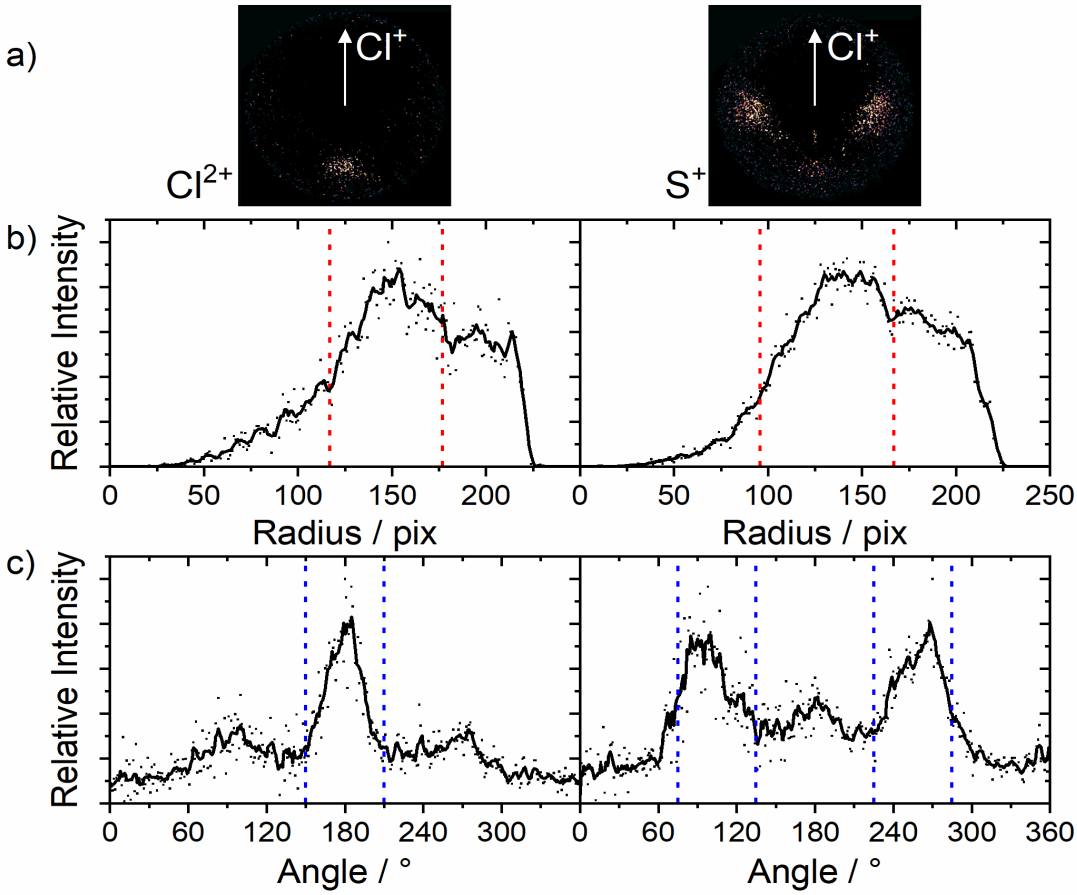

Figure 4.13: (a) Covariance maps for Cl^{2+} (left) and S^+ (right) referenced to Cl^+, with adjacent pixel smoothing and arrows indicating the orientation vector for the reference ions; (b) radial distributions corresponding to the above maps within the angular ranges indicated by the blue lines on the lower panels; (c) angular distributions for the respective images within the radial ranges indicated in red on the middle panels. Points represent raw data while the lines are five-point running averages.

increasingly observed. Multi-fragment images were recorded over these ions, covering the 16 – 37 m/z range (S^{2+} to $^{37}Cl^{+}$). Attempts to include lighter or more highly charged fragments in the gated range were frustrated by light organic ions originating from background contaminants in the chamber.

In Figure 4.12 it can be seen that in both cases the S^{+} is primarily observed to the sides. This is in contrast to the covariance maps for Cl^{2+} reference to Cl^{+} recorded under the higher intensity conditions, as can be seen in Figure 4.13. This is as expected based on the starting geometry of the molecule: for $CCSC^{n+}$ ($n \geq 3$), if there are charges localized on both Cl atoms and the S atom (and additionally on the C or O atoms), then the Cl ions will be expelled in opposite directions while the S^{+} is 'squeezed' out perpendicularly by the repulsion from the Cl on either side. This

link between starting geometry and Coulomb explosion covariance maps is similar to that previously demonstrated on other molecules[112, 173], and is an important step in establishing the viability of Coulomb explosion imaging in this experiment as an instantaneous probe of molecular structure for pump-probe experiments.

The increasing laser field strength changes the shape of the covariance map significantly. In the lower field case, more intensity is seen closer to 180°, and the plots in Figure 4.12(b) show that these ions are observed with lower translational energy. As the field strength is increased, this intensity diminishes in favor of more ions being observed at more acute angles, and these ions peak closer to 90° than even the peaks within the range highlight in red on the left panel of Figure 4.12(c). These observations suggest that in the lower field intensity, there is significant contribution from fragmentation of lower charge states of CCSC, where the unobserved Cl atom may be neutral or carrying a low charge, resulting

in the angle between Cl^+ and S^+ being closer to 180° and the translational energy being lower. In the high field case, more electrons are removed, and the angle gets significantly more acute as the increasing charge on the unobserved Cl fragment increases (for fixed charges on the observed ions in this case). The covariance map on the right of Figure 4.12 thus shows a 'purer' Coulomb explosion, with fragment ions moving primarily under the effects of Coulomb repulsion and their trajectories closely reflecting the starting geometry of the molecule. Simple Coulomb-only simulations suggest that the fragmentation of $CCSC^{5+}$ to Cl^+, Cl^{2+}, S^+, and CO^+ might be expected to yield S^+ ions with a translational energy release of ~8 eV and a relative angle to Cl^+ of 90°, in keeping with the results observed here.

Interesting covariance maps are also observed for CO^+ referenced to S^+ or vice versa, as shown in Figure 4.14. These maps show a sharp feature centered around 180°, similar to those observed from two-body dissociations such as processes (1) and (2). This feature is only observed under the higher laser field intensity used. The most plausible explanation for these features appears to be a two-step fragmentation of $CCSC^{4+}$, where two Cl^+ ions are ejected approximately in concert to leave behind OCS^{2+} with relatively low momentum, which subsequently undergoes explosive dissociation to give the observed products. It is also potentially possible, within the duration of the pulses used in this experiment, that the initial loss of $2Cl^+$ occurs from $CCSC^{3+}$, with an additional ionization of OCS^+ triggering the dissociation. Figure 4.14 also shows that if the dissociation is treated as a two-body fragmentation of OCS^{2+}, the two features are well momentum-matched, with peaks appearing around 6.0 eV (excluding the additional translational energy of the Cl^{n+} fragments). This matches well to the predicted energy release of 6.2 eV in a Coulomb-only

model for the fragmentation of OCS^{2+} (starting from the equilibrium geometry of CCSC without Cl atoms) but is significantly higher than the predicted energy release to optimized products of ca. 3.1 eV in ωB97X-D calculations. This suggests that the observed features can be best explained as arising from a primarily Coulomb-driven process from a high charge state of $CCSC^{n+}$ wherein the Cl^{n+} fragment momenta nearly offset, allowing for two-body-like behavior of the remaining product ions.

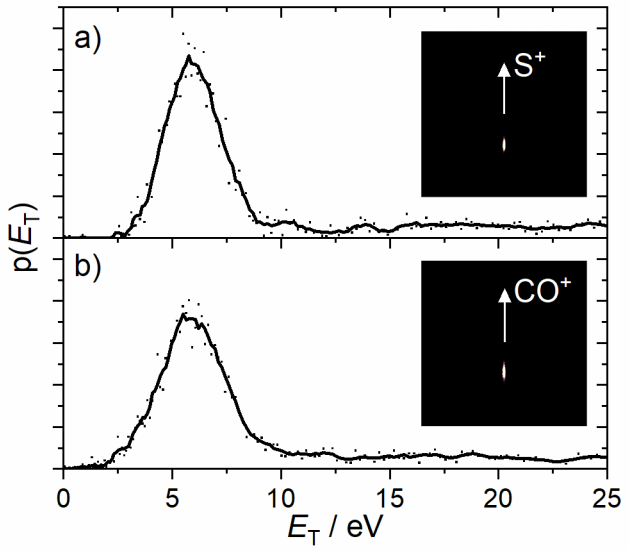

Figure 4.14: Translational energy distributions from covariance maps of (a) CO^+ referenced to S^+ and (b) S^+ referenced to CO^+ (both within angles of 170 – 190° to the reference ion vector), assuming that the reference ion is the co-fragment for conservation of momentum. Points represent raw data while the lines indicate the five-point running average. Insets: the covariance maps from which the spectra are extracted, with adjacent pixel smoothing and arrows showing the orientation vector of the reference ion.

4.4.2 Methoxycarbonylsulfenyl chloride (MCSC)

We now turn to an analogous study of CEI in MCSC. The TOF mass spectrum resulting from Coulomb explosion of MCSC with an intensity of ~ 2×10^{14} W/cm^2 is shown in Figure 4.15. Just as in the previous experiment, here the velocity map ion images of multiple fragments were recorded by defining a delay time window for the MCP such that it includes the TOF of all our fragments of interest. This way we were able to block highly abundant light background fragments ionized by the high intensity laser beam in the spectrum. All

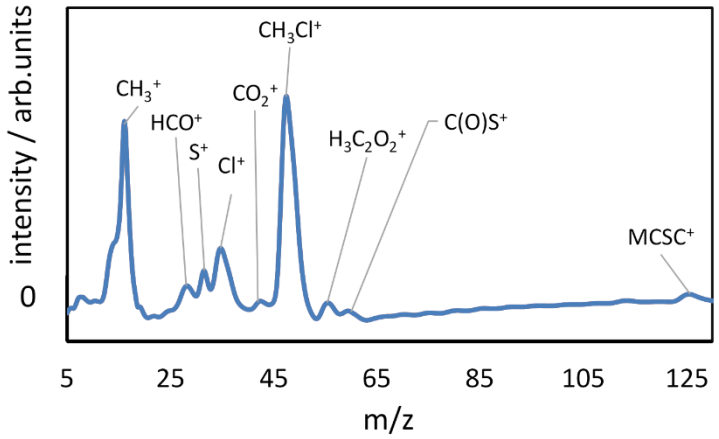

Figure 4.15: Background subtracted (Jacobian corrected) TOF mass spectrum of methoxycarbonylsulfonyl chloride (MCSC).

the images in this experiment were recorded with the new detector with its center masked manually to eliminate the signal from background ionization events with no associated translational energy release. As explained earlier, by correlating the ion spot intensity on the images with the peak amplitude in the TOF spectrum, coincident events were identified and subsequently the images for each ionic fragment were reconstructed from the correlated events on the camera and digitizer. We also acquired velocity map ion images

of individual ions in order to compare with the reconstructed images and verify the observed structures (Figure 4.16).

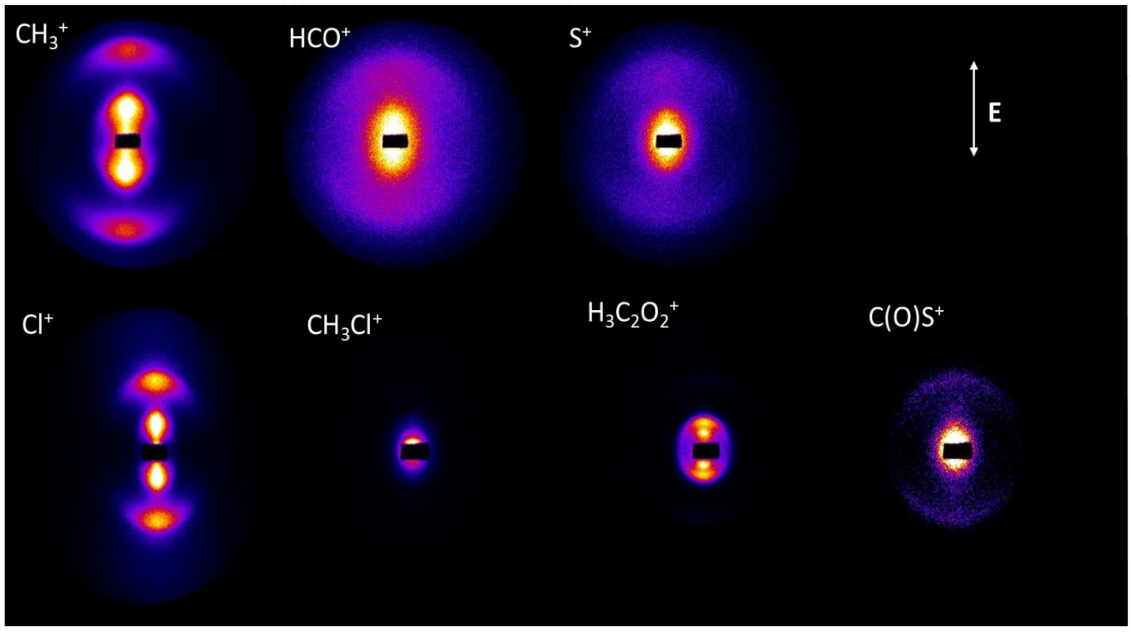

Figure 4.16: The corresponding VMI of each detected ion in the Coulomb explosion event. The polarization direction of the laser beam is shown with the white arrow.

In these raw VMI images we can see clear ring-like structures for CH_3^+, Cl^+, $C_2O_2^+$ and COS^+. Following VMI calibration, we were able to extract the translational energy distributions for individual fragments (fE_T) from these images. Also, in the case of two-body fragmentation events, we calculated total translational energy distributions (E_T) using conservation of momentum. The rings observed in CH_3^+ and Cl^+ images (assuming they are co-fragments) peak at the same value of E_T indicating that these fragments likely result from a two-body like dissociation event (Figure 4.17). The total translational energies are extracted from the reconstructed images using Finite Slice Analysis (FinA)[214]. Using multi-mass velocity map ion images, covariance maps between various pairs of ion momenta

were calculated. These calculations showed that there is a correlation between CH_3^+ and Cl^+ momenta as was observed by Erben et al.[196] in photoinduced fragmentation following an inner shell excitation of MCSC.

Covariance images of the CH_3^+/Cl^+ pair are shown in Figure 4.18 along with the angular distribution of their intensity as well as total translational energy extracted from the images. Both cases where Cl^+ and CH_3^+ ion velocity vectors are taken as reference vectors are shown in Figure 4.18(a) and (b). The angular distribution of the intensity in both images are identical as expected (Figure 4.18(c) and (d)). The very sharp feature at 180° indicates that these two fragments are likely produced from a two-body-like channel (process 1).

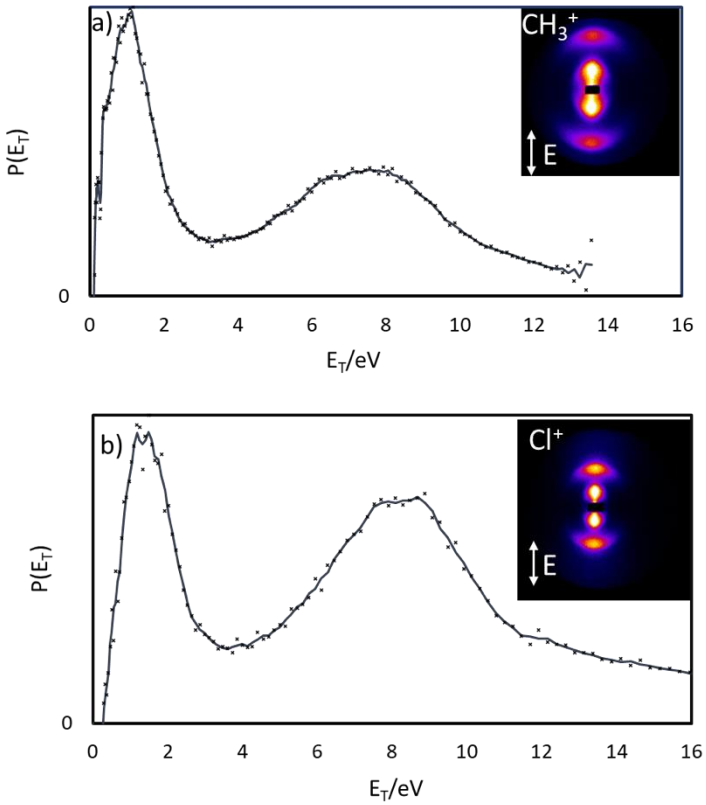

Figure 4.17: Total translational energy extracted from (a) CH_3^+ and (b) Cl^+ velocity map ion images. the cross markers indicate the raw values, and the curves are results of 3-point moving average smoothing.

$$CH_3Cl^{2+} \rightarrow CH_3^+ + Cl^+ \qquad (1)$$

Erben et al.[196] assigned this correlation to a three or four body dissociation channel with a deferred charge separation mechanism (DCS)[111] where an intermediate CH_3-SCl^{2+} or CH_3-Cl^{2+} is formed along with an ejected neutral co-fragment. Similarly, the formation of BrSF and ClSF as a result of FC(O)SBr and FC(O)SCl irradiation has been reported previously[219]. On the other hand Vallance et al.[107] showed that the covariance images for a three-body DCS mechanism has an oval shaped distribution which is in contrast with the sharp features in Figure 4.18(a) and (b). Therefore, we suspected that the correlation between this pair of ions is a result of pure two-body dissociation of methyl chloride formed as an impurity in the gas line or the source chamber before MCSC goes through dissociation.

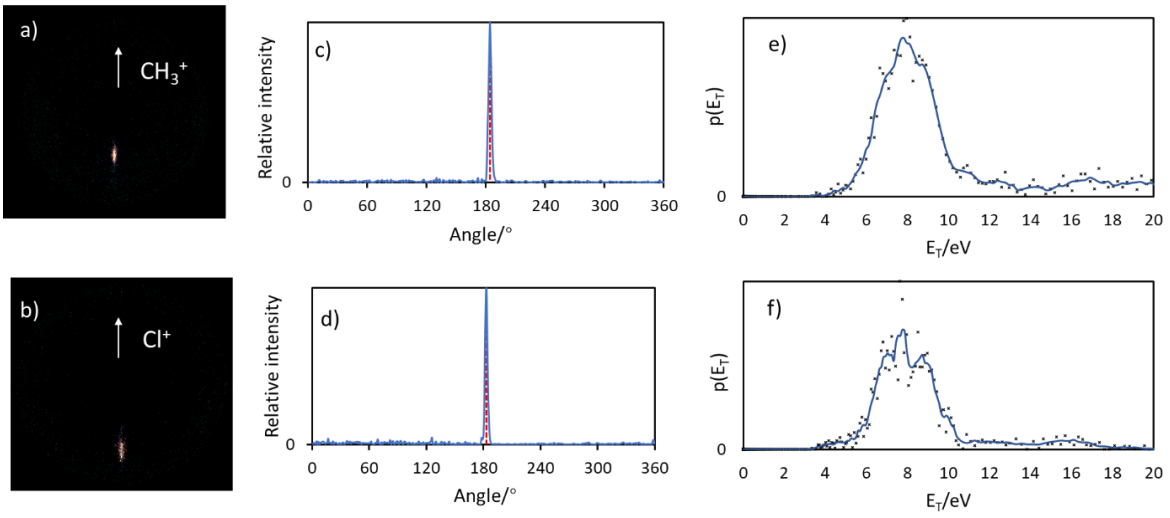

Figure 4.18: Covariance images of CH_3^+/Cl^+ pair along with their intensity angular distributions and total translational energy. (a) Cl^+ momentum vectors plotted with respect to CH_3^+ momentum vectors which are rotated and restricted to a single vertical direction showed with the white arrow, (b) CH_3^+ momentum vectors plotted with respect to Cl^+. (c) and (d) angular distribution of the intensity in 4.18(a) and (b), respectively. (e) and (f) total translational energy extracted from 4.18(a) and (b). the cross markers indicate the raw values, and the curves are results of 5-point moving average smoothing.

The total translational energy release (Figure 4.18(e) and (f)) was calculated from this pair of covariance images assuming that it results from double ionization and further Coulomb explosion of methyl chloride molecules which was formed before the interaction region in the main chamber. These two plots match well as expected peaking at around 8 eV which is very close to the peak value observed in the individual VMI images of these ions (Figure 4.17).

Another supposition is that in $MCSC^{2+}$ the charge density accumulates on opposite sides of the molecular di-cation (CH_3 and Cl groups) and leaves the middle fragment (O-CO-S) partly neutral. As the two end ionic fragments repel each other strongly in opposite directions, this neutral co-fragment little momentum has a minor impact on ion trajectories (a concerted three-body dissociation channel[111]). Vallance et al.[107] also explained that in a concerted three-body dissociation channel, the covariance images would be similar to those obtained in a two-body dissociation channel. To examine these two hypotheses, we calculated the Coulomb repulsion energy acting on the two end groups for both scenarios mentioned above. Some approximations were made when calculating this energy such as considering CH_3 and Cl groups as point charges and assuming their initial distance at the time of explosion equals to their equilibrium distance in the relaxed geometry of CH_3Cl (scenario 1) and in the relaxed geometry of MCSC at the ground electronic state (scenario 2). This leads to a value of 8.3 eV and 2.6 eV energy release for the first and second hypotheses respectively. Since the calculated Coulomb repulsion energy in the first scenario is close to the experimental value, we concluded that a pure two-body dissociation mechanism is responsible for these correlated events, where CH_3-Cl^{2+} is produced from

neutral CH_3Cl molecules that are formed before the reaction region and finally goes through Coulomb explosion.

To further investigate this, we also performed a separate experiment with CH_3Cl gas seeded in He, with the exact same experimental conditions set for MCSC molecule. The VMI images of CH_3 and Cl along with the extracted total translational energies were obtained. To minimize the experimental condition errors, we performed a new set of experiment with MCSC molecule in the same week that we did CH_3Cl experiment. According to the qualitative similarities between the velocity map ion images and the total translational energy extracted from the covariance image of Cl^+ with respect to CH_3^+ ions (figure 4.19), we believe that the sharp correlation observed in the MCSC experiment and previous studies[196] is a result of CH_3Cl impurity formed either in the gas line or the bubbler before the intersection of the molecule with the laser beam.

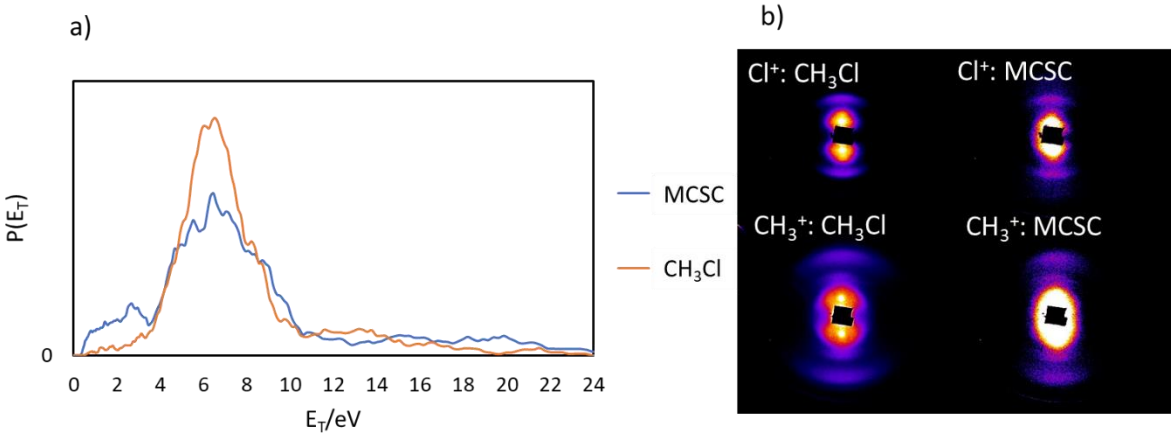

Figure 4.19: Total translational energies extracted from covariance image of Cl^+/CH_3^+ resulted from MCSC and CH_3Cl experiments. b) CH_3^+ and Cl^+ individual VMI images resulted from two corresponding experiments.

A weak correlation between Cl^+ and $H_3COC(O)^+$ pair of ions was observed. The corresponding covariance image (Figure 4.20) showed a distribution sharply peaked around 180° indicating a concerted three-body dissociation channel (process 2). The simultaneous ejection of the neutral fragment (S^0) with low momentum in this channel is assumed to have very little impact on the two ion trajectories thus leading to a sharp covariance image. The total translational energy was then extracted from the covariance image assuming a close to zero kinetic energy for the third neutral fragment. Using the same approximations, we made for the earlier channel (point charges and equilibrium bond distances) we obtained 4.88 eV for the Coulomb repulsion energy between this pair of ions. The higher energy feature could be a result of energy release for C-S bond breaking at high electronic states of the parent di-cation.

$$MCSC^{2+} \rightarrow H_3COC(O)^+ + Cl^+ + S^0 \qquad (2)$$

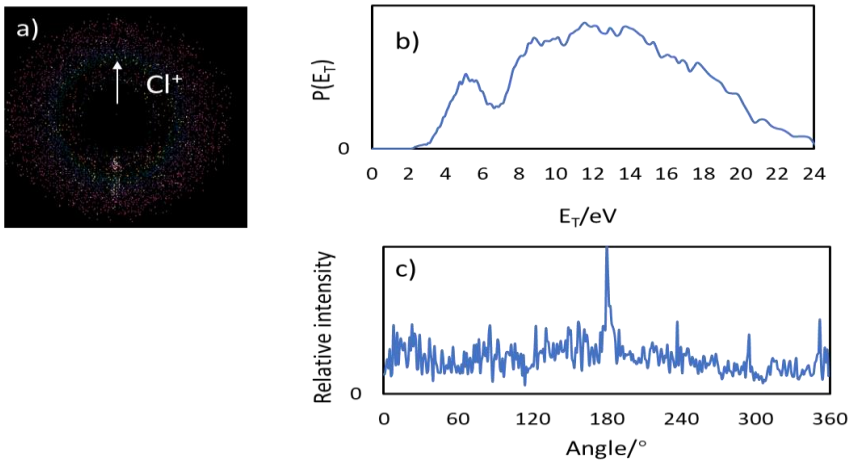

Figure 4.20: Covariance image of $H_3COC(O)S^+/Cl^+$ pair along with total translational energy and angular distribution of the intensity in the image.

We also observed a correlation between HCO^+ and $C(O)S^+$ fragments' momenta. This correlation was not observed by Erben et al.[196]. The covariance images of $HCO^+/C(O)S^+$ show a broader distribution of signal intensity peaking at about 180° (Figure 4.21). This broadening of the intensity is indicative of an initial or deferred charge separation mechanism[107] in which the non-negligible momenta of the neutral fragments results in less sharp signals compared to what is observed for the earlier channel. According to the ab initio calculations the vertical singlet and triplet states of MCSC di-cations are 1.03 and 1.75 eV higher in energy compared to the products in process 3. In both cases the energy difference is lower than the experimental value of the fragment translational energies. This can be indicative of dissociation at higher excited states of the parent di-cation. We also examined the possibility of a triply charged parent that goes through dissociation using a three-fold covariance analysis[174] as we applied to chlorocarbonylsulfenyl chloride. Since we did not observe any correlations, we concluded that all other products produced along with $C(O)S^+/HCO^+$ ions are neutral.

$$MCSC^{2+} \rightarrow HCO^+ + H_2 + C(O)S^+ + Cl \qquad (3)$$

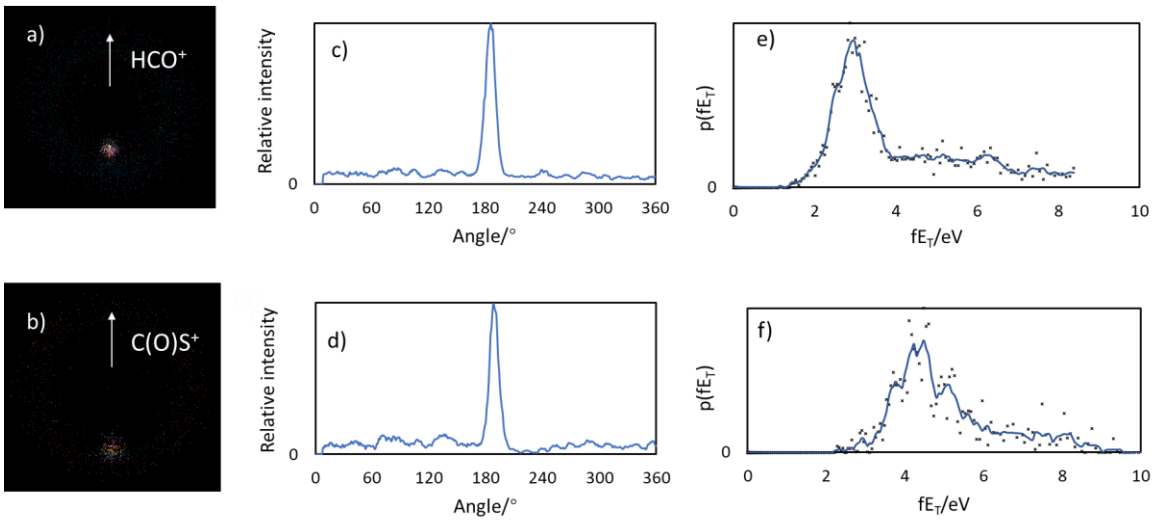

Figure 4.21: (a) and (b) Covariance images of $C(O)S^+/HCO^+$ pair. (c) and (d) angular distribution of the intensity in images (a) and (b). (e) and (f) fragment translational energy distributions of $C(O)S^+$ and HCO^+ respectively.

Conclusion:

We demonstrated the capability of our apparatus to implement a three-dimensional multi-mass coincident detection in a laser-induced Coulomb explosion experiment. Using this multi-mass imaging technique, we used covariance map analysis to find correlations between pairs of photoproducts which were produced from the same ionization events. Coupling Coulomb explosion with a covariance map analysis enabled us to unravel the dissociative ionization dynamics of thioesters.

Chlorocarbonylsulfenyl chloride undergoes multiple ionization and fragmentation processes when exposed to strong laser fields. Following double ionization, the dominant process is C–S cleavage, as the ground electronic state of $CCSC^{2+}$ is dissociative along this coordinate. However, an alternative pathway featuring loss of Cl^+ is also observed, with recorded translational energies indicating that this occurs on excited surfaces exhibiting a

barrier to breaking the C–S bond. Further ionization to the tri-cation leads to processes such as three-body fragmentation to yield $COCl^+$, S^+, and Cl^+, confirmed using three-body covariance analysis techniques, while removing further electrons leads to higher degrees of atomization where the relative trajectories of the product ions are derived from the parent molecule's starting geometry.

CEI of methoxycarbonylsulfenyl chloride revealed that the sharp correlation previously observed between CH_3^+ and Cl^+ does not appear to arise from the parent molecule dissociation but rather is a result of CH_3Cl contaminant likely formed from MCSC decomposition in the sample introduction system. It may be that this same phenomenon is responsible for the observation of this correlation in the synchrotron studies, highlighting the advantage of CEI in this case. A concerted three-body dissociation leading to $Cl^+/H_3COC(O)^+$ correlation was discovered from the corresponding covariance images. The correlation found between HCO^+ and $C(O)S^+$ is assigned to a 4-body dissociation giving neutral Cl and H_2 as coproducts, possibly via excited electronic states of the doubly charged parent ion.

Chapter 5

Time-resolved Ultrafast Electron Diffraction imaging of excited oxalyl chloride

5.1 Introduction

In order to control chemical, physical, and biological processes, it is crucial to unravel the static and dynamic molecular structures. During last few decades, time-resolved laser spectroscopy techniques have been exploited to study the photo-induced reaction dynamics in real time and extract molecular geometry changes indirectly by comparing the resulting spectroscopic features with theoretical simulations[22, 220, 221]. Such techniques have successfully retrieved the electronic dynamics while they have been unable to directly acquire the nuclear trajectories in real time and space. Besides, interpreting the results of such techniques typically requires complicated high levels of theoretical computation. Recent advances in ultrafast diffraction-based imaging methods have enabled us to have a more detailed look into the nuclear dynamics with atomic scale spatial resolution and temporal resolution on the timescale of bond breaking and rearrangement.

Ultrashort X-ray pulses produced from synchrotron or free electron lasers (FEL) with femtosecond time resolution have been widely used in structural dynamics studies of bulk materials such as condensed samples because such optical pulses possess short enough wavelength (high energy) to have a deep sample penetration apart from their high temporal and spatial resolution[222-224]. While in the case of gas phase or thin film samples, ultrafast

electron beams are preferentially used to probe the structural changes of the molecular systems, since such pulses have about six orders of magnitude larger scattering cross section compared to X ray pulses[222], as well as shorter de Broglie wavelength which leads to higher spatial resolution, and less radiation damage per elastic scattering event[225, 226].

Gas phase ultrafast electron diffraction (UED) techniques have recently reached femtosecond time resolution with the development of a mega electron-volt (MeV) UED system at the SLAC National Accelerator Laboratory[227]. At such levels of energies, electrons become relativistic and hence the significant reduction of velocity mismatch between electrons and pump optical pulses as well as reduced space charge effects, leading to higher total instrument temporal resolution. Sub-angstrom spatial resolution combined with sub-100 femtosecond temporal resolution of MeV UED techniques is exploited in order to capture the ultrafast dynamics of isolated molecules.

Using the gas-phase MeV UED technique, the rotational wave-packet dynamics in optically aligned nitrogen molecules and coherent motion of a vibrational wave-packet in isolated iodine molecules have been captured[228, 229]. Since the development of this technique, it has demonstrated its wide applicability in various ultrafast studies such as direct real-space, real-time mapping of the coherent nuclear wave-packet trajectories through conical intersection in isolated molecules[230], dissociation dynamics of complex molecular systems[231], direct observation of photo-induced ring-opening[232], and simultaneous observation of electronic and nuclear dynamics[233].

Here in this study, we have used the gas-phase MeV UED apparatus, a component of the Linac Coherent Light Source Facility at SLAC, to study the unique UV photodissociation of oxalyl chloride. Oxalyl chloride has been the subject of various studies in organic

synthesis and kinetics[234-238]. It has been introduced as a clean photolytic source of chlorin atoms for collision dynamics studies because of large absorption cross section in the UV wavelength range of 193-248 nm (Figure 5.1), high Cl atom quantum yield and unreactive co-fragments[239]. Also, its structural and conformational properties have been studied experimentally and theoretically. Danielson et al.[240] confirmed the existence of a second conformer with gauche form beside its most stable anti form, using gas phase electron diffraction technique along with ab initio calculations.

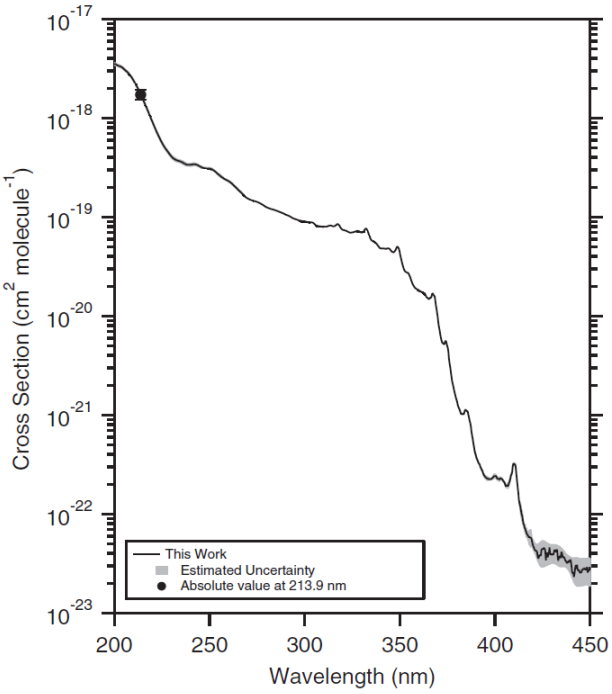

Figure 5.1: Gas-phase UV/VIS absorption spectrum of oxalyl chloride at 296 K. Adapted with permission from B. Ghosh, D. K. Papanastasiou and J. B. Burkholder, J. Chem. Phys 137 (16), 164315 (2012).©American Institute of Physics.

The photodissociation dynamics of oxalyl chloride have been of great interest due to the available energy for breaking multiple bonds (C-C and two C-Cl bonds) in a single UV

photon with the wavelength of 193-248 nm. Ahmed et al.[241] used photofragment imaging technique to investigate the dissociation dynamics of this molecule at 235 nm and discovered that it dissociates into four fragments upon absorption one UV photon. According to the photofragment images, they concluded that the dissociation dynamics follows a two-step mechanism where the first step is an impulsive three-body dissociation channel yielding translationally fast Cl and CO fragments along with slow COCl radicals. The Cl atoms produced in the first step are mainly at their spin-orbit excited state ($^2P_{1/2}$) and CO components are highly rotationally excited (J=30-55). The anisotropic distribution of the fragments produced in the first step is indicative of a fast dissociation step compared to the molecular rotational time scale. Part of the remaining COCl radicals go through dissociation at longer time scales such that the produced Cl and CO fragments have a purely isotropic angular distribution with the CO peaking at lower rotational levels and Cl mainly at its ground electronic state ($^2P_{3/2}$). Later Hemmi and Suits[242] extended these results using photofragment translational spectroscopy at 193 nm. Wu et al.[243] observed similar results at 248 nm using time-resolved Fourier transform spectroscopy. However, in a later study[244] performed at 193 nm, they proposed a different mechanism for the UV photodissociation of oxalyl chloride as the main channel for shorter UV wavelength. combining the internal energy of CO fragments and translational energies reported in previous study[242], a concerted four body dissociation mechanism was suggested. They argued that the two-step mechanism previously observed, could be the result of a minor channel involving electronically excited intermediates.

Fang et al.[245] performed electronic structure calculations along with molecular dynamics (MD) simulation to investigate the photodissociation dynamics of oxalyl chloride in the

wavelength range of 193-248 nm. They also simulated C-C, C-Cl and C-O bond time constants. According to these simulations, the molecule is excited to S_1 state upon absorption a single UV photon where the adiabatic C-C and C-Cl bond fissions show little possibility. Their result suggested that the main trajectories (60%) go through a synchronous concerted four-body dissociation channel after an internal conversion from S_1 to S_0 state. However, a minor channel (~17%) of a concerted three-body dissociation mechanism was observed.

Due to these inconsistent experimental and theoretical results, we have performed a time-resolved experiment on oxalyl chloride for the first time to reveal its structural dynamics in real time and hence infer its main dissociation mechanism at this UV wavelength range. An ultrafast 200 nm pump beam is used to induce excitation in the molecular beam which is subsequently probed by MeV electron pulses. The pair distance distributions as a function of time are then extracted from diffraction patterns and interpreted to acquire information about the development of intermediate structures.

5.2 Experimental Methods

The experimental apparatus has been described in chapter 2. Briefly, we use the fourth harmonic generation of a Ti:Sapphire fundamental output (wavelength = 200 nm, temporal width ~100 fs, beam size ~300 μm) as a pump beam to excite the molecules. The probe electron beam accelerated to 4.2 MeV propagates through the gas flow almost collinearly with respect to the pump pulse (angle ~5°) with a repetition rate of 360 Hz. The gas flow containing 1% oxalyl chloride seeded in He is heated to 70° C and introduced to the

chamber through a 500 μm orifice flow cell. The scattered electrons are then sent toward a detector and their diffraction patterns on the detector are imaged through a CCD camera. We have performed the experiment at high charge mode (total temporal resolution ~ 500 fs) and low charge mode (total temporal resolution~ 200 fs) to investigate both fast and slow dissociation dynamics of the system. The laser energy at high charge mode was set at 10, 16 and 25 μJ/pulse and at the low charge it was set at 16 μJ/pulse.

5.3 Theory

As the electron beam intersects with a molecular beam, electrons are scattered due to the electrostatic potential of atoms and molecules leading to the interference of the diffracted electron beams. The resulting diffraction patterns are used to extract structural information of the system.

Gas phase electron diffraction is described based on the scattering theory[246-250]. The electron wave scattered elastically by a single atom (assuming the independent atom model) can be described as a spherical wave:

$$\psi = Ka\frac{e^{ik_0R}}{R}f(\theta)e^{i(k_0-k)r} \quad (5.1)$$

$$K = 8\frac{\pi^2 mq^2}{\hbar^2} \quad (5.2)$$

Here a is the normalizing wave constant, R is the distance between the scattered electron wave and the observation point (detector), f(θ) is the elastic scattering amplitude of the specific atom that is calculated through ELSEPA[251], k_0 and k are the wave vector of the non-scattered and scattered electrons respectively, r is the atomic position vector, m and q are the electron mass and charge respectively and ħ is the plank's constant. In the case of

scattering off a molecule the scattered wave is a result of coherent sum of N atoms within the molecule:

$$\psi = \sum_{i=1}^{N} \psi_i \tag{5.3}$$

The scattering intensity is acquired simply from a proportional relationship between electron intensity and current density:

$$I = I_0 \frac{J}{J_0} \tag{5.4}$$

Where J_0 and I_0 are the initial electron current density and intensity, I and J are the scattered electron current density and intensity. Scattered current density is calculated by the following equation[252]:

$$J(r) = -\frac{ie\hbar}{2m}\left[\psi^*(\vec{\nabla}\psi) - (\vec{\nabla}\psi^*)\psi\right] \tag{5.5}$$

Therefore, the total diffraction intensity is calculated by inserting 5.5 into 5.4 as a function of electron momentum transfer:

$$I(s) = \frac{K^2 I_0}{R^2} \sum_{i=1}^{N} \sum_{j=1}^{N} f_i(s) f_j^*(s) e^{isr_{ij}} \tag{5.6}$$

Here r_{ij} is the interatomic distance between atoms i and j, N is the total number of atoms, s is the electron momentum transfer that is defined as the difference between the initial and

scattered electron wave vectors $s = |k - k_0| = \frac{4\pi}{\lambda} sin(\frac{\theta}{2})$ where θ is the scattering angle and λ is the De Broglie wavelength which is 0.26 pm for the electron energy of 4.2 MeV.

The total diffraction intensity can be broken into atomic and molecular intensity. The molecular diffraction intensity is of interest as it contains inter-nuclear distances:

$$I_a(s) = \frac{K^2 I_0}{R^2} \sum_{i=1}^{N} f_i(s)^2 \tag{5.7}$$

$$I_m(s) = \frac{K^2 I_0}{R^2} \sum_{i=1}^{N} \sum_{j=1, j\neq i}^{N} f_i(s) f_j^*(s) e^{isr_{ij}} \tag{5.8}$$

In a randomly oriented gas phase molecular beam, the molecular diffraction intensity integrated over all molecular orientation is given by:

$$I_m(s) = \frac{K^2 I_0}{R^2} \sum_{i=1}^{N} \sum_{j=1, j\neq i}^{N} f_i(s) f_j^*(s) cos(\eta_i - \eta_j) \frac{sin(sr_{ij})}{sr_{ij}} \tag{5.9}$$

Here η_i is the i-th atom phase shift. As the atomic number differences increases, the phase shift needs to be considered. The molecular diffraction intensity includes the structural information and needs to be extracted from total diffraction intensity. In order to normalize the diffraction intensity, modified scattering intensity is used:

$$sM(s) = \frac{I_{total} - I_{bkg}}{I_a} = s \frac{I_m(s)}{I_a(s)} \tag{5.10}$$

Where I_{total} is total scattering intensity and I_{bkg} is the background scattering including (atomic scattering, contribution from background gasses in the chamber, UV background

and dark current). Since in this experiment, an ultrashort laser beam induces excitation in the system, molecules are not randomly oriented due to the inherent strong field alignment[253]. In order to remove anisotropy, the diffraction pattern is projected onto the Legendre polynomial to remove non-isotropic contribution by keeping 0-th order polynomial:

$$sM_n(s) = \int P_n(cos(\varphi))sM(s,\varphi)|sin(\varphi)|d\varphi \qquad (5.11)$$

Where φ is the azimuthal angle and P_n is n-th order Legendre polynomial.

The data can be transferred from the momentum space into real space through a Fourier transform of the modified scattering intensity. The pair distribution function (PDF) which directly gives the inter-atomic distances is calculated as:

$$PDF(r) = \int_0^{s_{max}} sM(s)sin(sr)e^{-ks^2}ds \qquad (5.12)$$

Where k is a damping factor that is adjusted to minimize the effect of finite s range[254], and s_{max} is the maximum measured s value. The peaks in PDF(r) correspond to inter-atomic distances.

In order to isolate structural changes in the diffraction signal, we use diffraction-difference[255] method. The difference diffraction map is given by:

$$\frac{\Delta I(t,s,\varphi)}{I} = \frac{I(t>0,s,\varphi)-I(-t,s,\varphi)}{I(-t,s,\varphi)}$$

$$\Delta sM(t,s) = sM(t,s) - sM(-t,s) \qquad (5.13)$$

$$\Delta PDF(t,r) = PDF(t,r) - PDF(-t,r)$$

Where φ is the azimuthal angle of the diffraction pattern, -t is the negative time delay before the excitation starts.

5.4 Image Processing

Here we used a standard image processing to isolate the scattering signal in 2-D diffraction images by removing all experimental noise[231, 254] such as dark current, the detector impurities and X-ray streaks which are minimized by building a lead box around the camera. The image processing algorithm and other related calculations were performed using MATLAB R2021a[256].

First, the outlier pixels at each stage position (with more than 3 standard deviations (std) from the mean) were removed. The hole drilled in the center of the detector to avoid the potential damage caused by the focused non-scattered electrons, was masked along with other detector artifacts. The anisotropy in the static images were spotted by visualizing the images in contour maps and removed.

The images recorded under unstable experimental conditions such as the electron gun valve trip, sudden temperature or pressure jumps in the chamber were removed. The center shift induced by the plasma lensing effect was corrected by shifting the image centers back to the static center. The radial outliers (more than 3 std) were removed, and a median filter was applied to account for the high frequency noise. As mentioned in the theory section, the non-isotropic components shown by higher order Legendre polynomials were removed.

The image normalization was performed by dividing the mean intensity at each stage position by the intensity of regions which are less affected by noise ($1.5< s <6$ Å^{-1}). A baseline was subtracted from images at each stage position corresponding to the mean intensity of the largest radius.

Here in order to obtain the background scattering intensity required for static modified scattering calculations, we used a standard fitting procedure[257] based on a set of zero-crossings of s values where the theoretical $I_M(s)$ equals to zero. Then an exponential curve ($\exp(a+bs^c)$) was fitted to the experimental scattering intensity I_{total} at these s values to obtain I_{bkg}.

5.5 Solid Sample

In order to acquire an accurate time zero which is the temporal overlap between the electron and optical pulses (T_0) as well as pixel to s calibration, the electrons scattered against a solid sample (Bismuth crystal) with well-known diffraction patterns were imaged at different time delays.

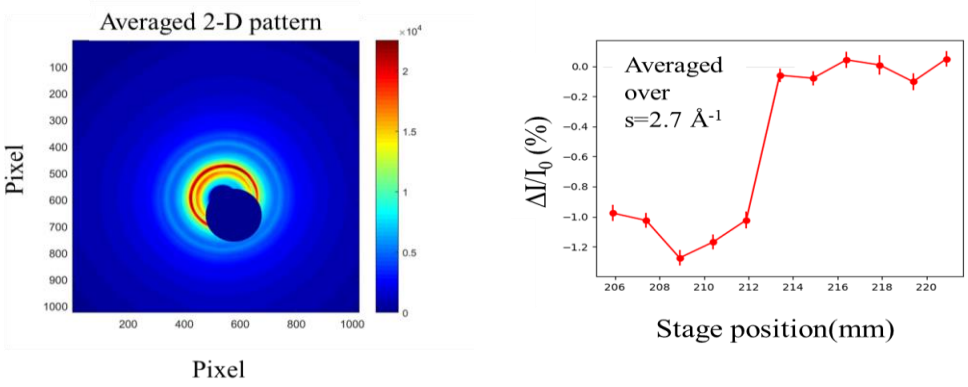

Figure 5.2: (a) solid sample 2-D diffraction image averaged over all time delays. (b) difference pattern extracted from 2-D plot corresponding to the highest scattering intensity at the s value of 2.7 Å^{-1}.

The averaged 2-D diffraction pattern of Bi sample along with the time dependent difference intensity extracted from 2-D patterns are shown in Figure 5.2. The difference signal at the s value corresponding to the highest intensity was plotted as a function of delay (stage position) to get the stage position corresponding to time zero.

The experimental and literature scattering intensity [258] were compared to get a reliable pixel to s calibration. (Figure 5.3)

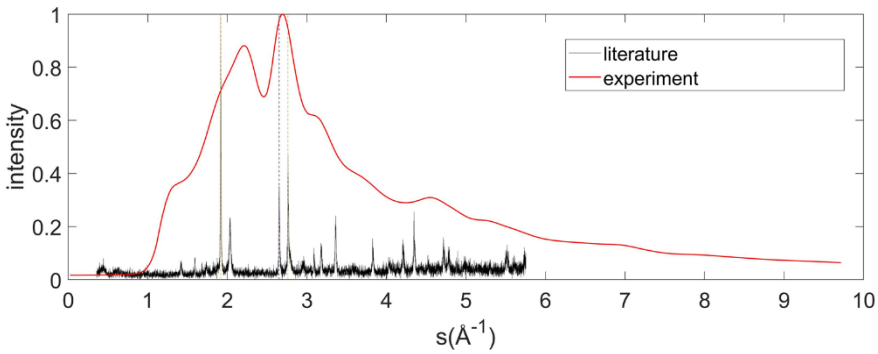

Figure 5.3: Experimental and literature total scattering intensity of Bi crystal plotted as a function of momentum transfer.

5.6 Theoretical Calculations

The geometry optimization for both conformers (Figure 5.4) of oxalyl chloride was performed at density functional theory (DFT) level [197, 198] using the ωB97X-D functional[199] and Dunning's aug-cc-pVTZ basis set[200-202] resulting electronic structures which are in consistent with previous calculations[240]. The anti conformer is slightly more stable than the gauche form (0.18 kcal/mol) with a planar skeleton (C_{2h} symmetry), while gauche form has a dihedral angle of ~88°. The bonding and non-bonding distances of both conformers are given in Table 5.1.

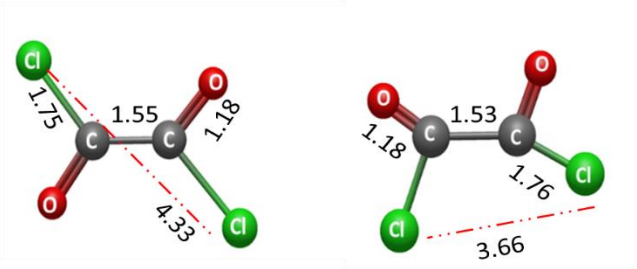

Figure 5.4: The two most stable conformers of oxalyl chloride (left: Anti, right: Gauche). All bonding and non-bonding distance reported in Å.

We also performed time-dependent density functional theory (TDDFT)[259] calculations based on the optimized structures to estimate the oscillator strength of the two conformers in the Frank-Condon region. Based on these calculations, the gauche conformer has close to zero oscillator strength in the vicinity of 200 nm, indicating negligible absorption at this wavelength. Therefore, we expect this conformer to have little contribution in our time dependent experimental signal as it does not go through photoexcitation. All these calculations were performed using Gaussian 16W package[260].

Table 5.1: Bonding and non-bonding distances in the geometry optimized structure of anti and gauche conformers of oxalyl chloride.

	Bonding distances(Å)			**Non-bonding distances (Å)**				
	C-C	C-Cl	C=O	C--Cl	C--O	Cl—Cl	Cl--O	O--O
Anti	1.55	1.75	1.18	2.74	2.42	4.33	2.6,2.94	3.48
Gauche	1.53	1.76	1.18	2.72	2.42	3.66	2.61, 3.4	3.15

5.7 Static Analysis

The static experimental and theoretical modified scattering were compared to confirm the reliability of the experimental condition. The experimental modified scattering is not available for s <0.7 $Å^{-1}$ due to the hole in the center of the detector. Since oxalyl chloride has two stable conformers, the conformer ratio was adjusted to get the best agreement between simulation and experiment (Figure 5.5).

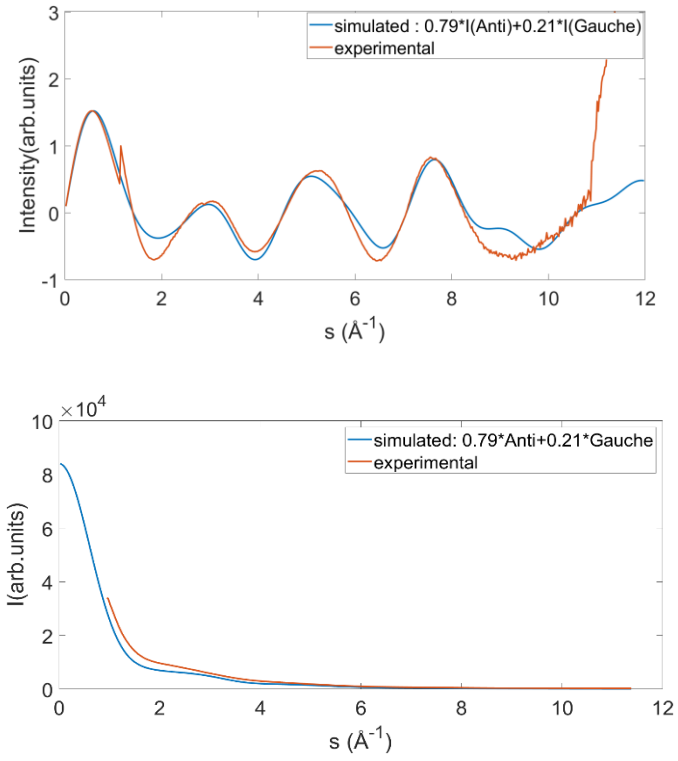

Figure 5.5: Static experimental and simulated modified (top) and total (bottom) scattering spectrum of oxalyl chloride.

The Boltzmann distribution, estimates the conformer ratio based on the following equation:

$$\frac{P_A}{P_C} = e^{\frac{\Delta E}{RT}} \tag{5.14}$$

Where P_A and P_G are the fractional population of anti and gauche forms in thermodynamic equilibrium. ΔE is the energy difference of conformers, R is the molar gas constant and T is the absolute temperature. According to this approximation at the experimental temperature (~70°C) we expect a 0.78/0.22 ratio of anti/gauche which is in good agreement with the value we obtained from the static spectrum analysis. The absolute energy of each conformer was calculated through geometry optimization.

By transferring the spectrum from momentum space to real space we get the radial distribution function which is plotted in Figure 5.6 for both experimental and simulation results. There is good qualitative agreement between simulated and experimental results with each peak corresponding to one or more bonding and non-bonding distances

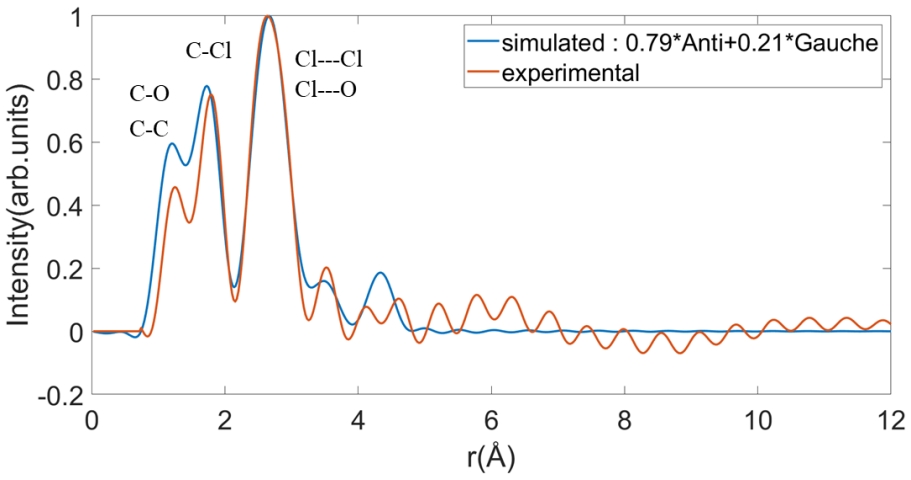

Figure 5.6: Static experimental and simulated pair distribution function of oxalyl chloride.

5.8 Time-dependent Data

As mentioned in the theory section, here we use diffraction-difference method to highlight the time-dependent signal arising from the molecule structural changes. In this method, the diffraction patterns of the ground state parent molecule are obtained at negative time delays to be used as a reference signal. Since the background signal including the incoherent atomic scattering, ground state parent, background gas in the chamber and dark current is present in the diffraction patterns of all time delays, here there is no need to estimate the background intensity using the zero crossings obtained from the theory. Therefore, by using this method, the results are not biased by the input from the simulation unlike the static analysis.

A set of power scan experiments at four time delays (-10,-5,10,70 ps) was performed to find the highest laser intensity where no multi-photon effects is observed. The difference signal amplitude showed a clear linear dependence to the laser intensity from 5.6 to 16 μJ/pulse which is the evidence of single-photon regime (Figure 5.7).

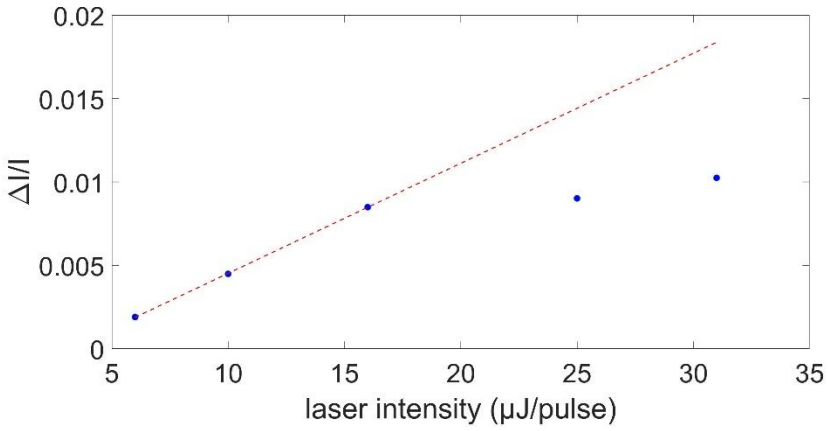

Figure 5.7: Difference signal in the region of 1.6 < s <2.2 $Å^{-1}$ as a function of laser intensity.

First, we analyze the images recorded under high charge mode. Three sets of high charge mode experiments were performed at the laser intensity of 10,16 and 25 μJ/pulse. Here, we only show the analysis of data recorded at 16 μJ/pulse since at this intensity there is higher signal to noise ratio and less probability of multi-photon effects. We observed good agreement between images recorded at 10 and 16 μJ/pulse, however the diffraction patterns acquired at 25 μJ/pulse show clear signatures of multi-photon effects.

In order to estimate the total temporal resolution of the experiment, the instrument temporal resolution was convoluted with the molecular response time[231]. To do so, we picked an area with the highest diffraction difference signal (ΔI/I) and fitted an error function to it:

$$\text{errf} - \text{fit} = a \times erf(-(x-b)/(c/(2 \times sqrt(2 \times log(2))) \times sqrt(2)) + d$$

in Figure 5.8 the highest difference signal corresponding to $1.4 < s < 2.5$ Å^{-1} is plotted as a function of time along with the error function fit for both high charge and low charge mode. With this technique, the experiment time resolution is determined to be 200 and 430 fs for high and low charge mode respectively.

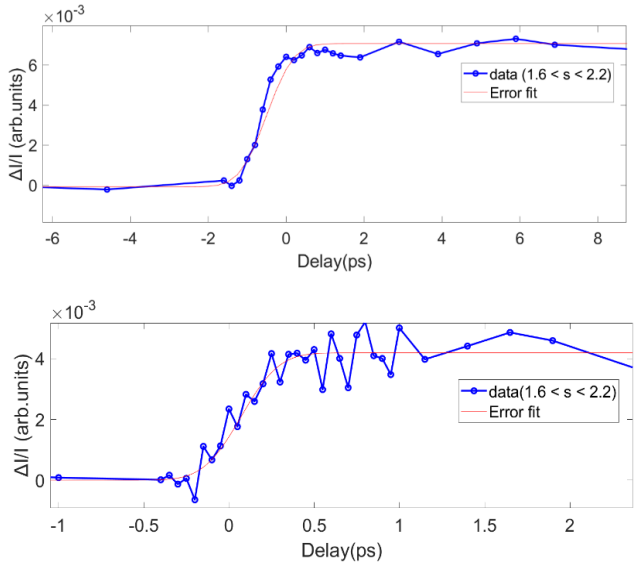

Figure 5.8: Temporal evolution of the difference signal in the region of 1.6 < s <2.2 $Å^{-1}$ along with the time zero fit for high (top) and low (bottom) charge mode experiment.

At each high charge mode experiment about 100 time-scans were performed with each scan including 40 time delays ranging from -10 to 200 ps with 200 fs-1 ps-10 ps time steps. Two-dimensional diffraction images recorded at all time delays are cleaned as explained in the image processing section to eliminate all possible experimental noises and detector artifacts (Figure 5.9).

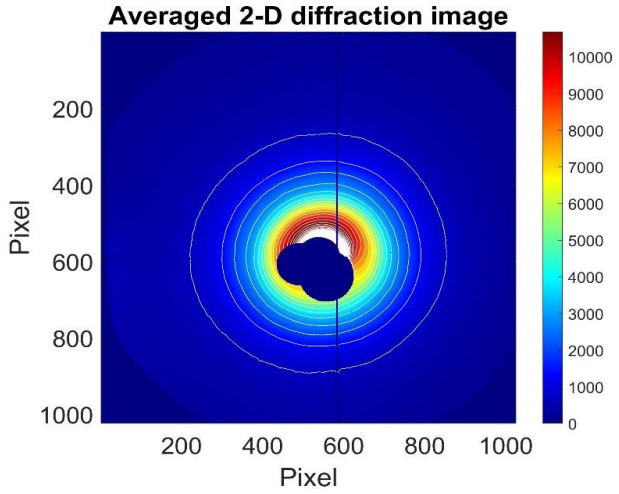

Figure 5.9: High charge 2-D diffraction pattern averaged over all time delays.

Diffraction difference signal false color maps (1-D signal) extracted from 2-D images by averaging over the azimuthal angle are plotted as a function of delay and momentum transfer (Figure 5.10). The intense bleach observed in low s region is indicative of a strong distance loss. A positive feature in the region of $1.6 < s < 2.2$ Å^{-1} could be the result of a new bond formed or an oscillating distance gain due to rotational excitation.

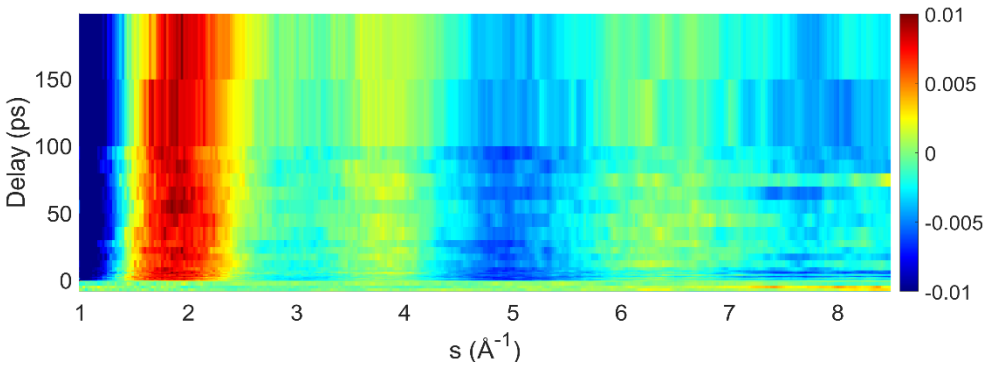

Figure 5.10: ΔI/I false color map of oxalyl chloride as a function of time and momentum transfer.

To better understand this map, a Fourier transform was applied to the modified scattering intensity difference to transform the data to the real space (Figure 5.11). The distance losses in the region of $1.4 < r < 1.9$ Å match well with the bonding distances of C-C and C-Cl, while the feature in the region of $2.4 < r < 3$ Å correspond to the non-bonding distances of C---O and C---Cl. The formation of CO fragments with the bonding distance of 1.11 Å clearly explains the positive region appearing around 1.1 Å in this map. A more intense positive feature at longer distances of $3.2 < r < 4$ Å is explained by the fact that the gauche conformer has close to zero oscillator strength at 200 nm. Therefore, the anti conformers are selectively depleted giving rise to the gain distance feature at this region corresponding to the non-bonding distance of Cl---Cl in gauche forms.

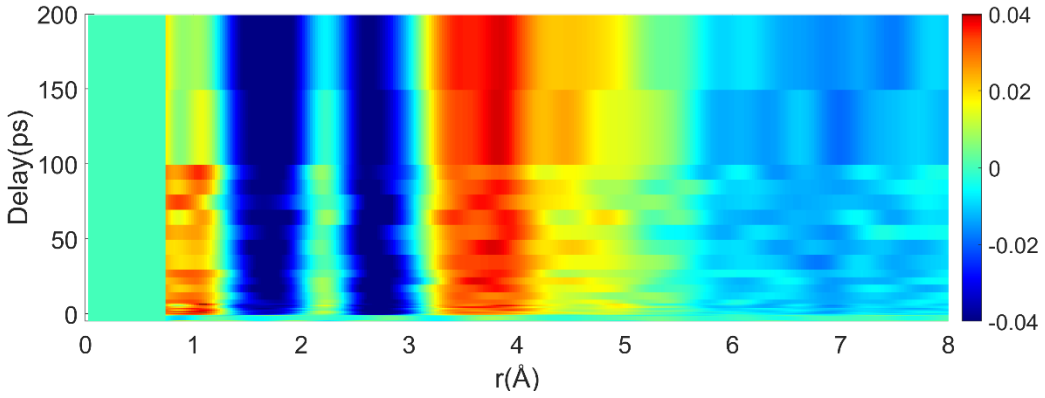

Figure 5.11: ΔPDF false color map of oxalyl chloride as a function of time and interatomic distance.

To confirm these assignments, we simulated the pair distribution function for a mixture of products (10% of CO) and non-excited reactants (90% of anti and 100% of gauche) to calculate the radial distribution of the difference signal. In Figure 5.12, the averaged experimental pair distribution function difference over delay range of 20-60 ps plotted as a function of distance is compared with the simulated difference signal. This plot shows good qualitative agreement between experiment and simulation. We also simulated a difference signal based on the formation of COCl radical as the coproduct of CO, However the resulting radial distribution showed clear disagreement with the experiment. This tells us that the concerted four body dissociation mechanism where C-O and C-Cl bonds fission occur simultaneously giving rise to stable CO fragments, is more probably the main dissociation channel of oxalyl chloride at this UV wavelength. However, to draw more accurate conclusions we need to do simulations based on MD calculations.

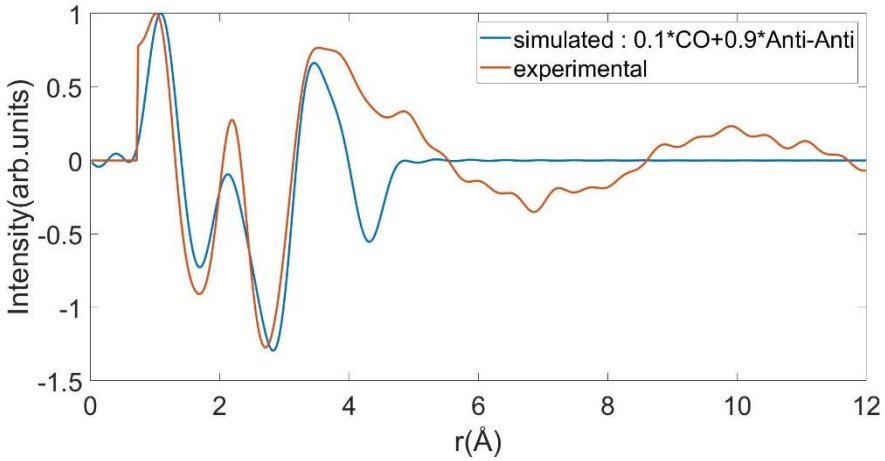

Figure 5.12: Experimental and simulated pair distribution function difference with 10% excitation percentage.

We applied the same data analysis procedure to the low charge mode. In this run, about 120 time-scans were performed each including 37 time delays ranging from -5 to 2.5 ps with 50 and 250 fs time steps for shorter and longer delays respectively. The averaged 2-D diffraction image shown in Figure 5.13 has clearly less signal compared to Figure 5.9 due to less charge per bunch in this regime.

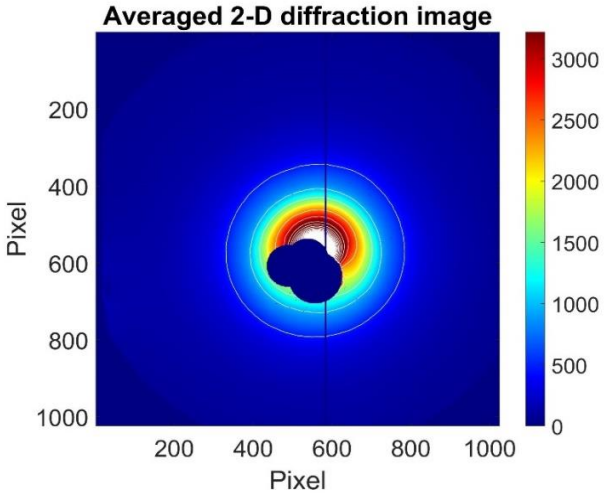

Figure 5.13: Low charge 2-D diffraction pattern averaged over all time delays.

The difference signal false color map in momentum and real space is shown in Figure 5.14. The same features observed in high charge mode, is seen in this regime as well. Here, with the higher temporal resolution, the bleach features corresponding to bonding and non-bonding distance losses show an onset of 400 fs. This is in agreement with the MD simulations of Fang et al.[261] where predicted an average delay of 300-1000 fs before C-C bond fission starts. However, by creating simulated diffraction difference patterns based on future MD simulations we will be able to infer the dynamics of photodissociation more accurately. Such MD simulations will also help us to determine whether the positive region observed in the long distance correspond to a possible rotational excitation in the molecular fragments.

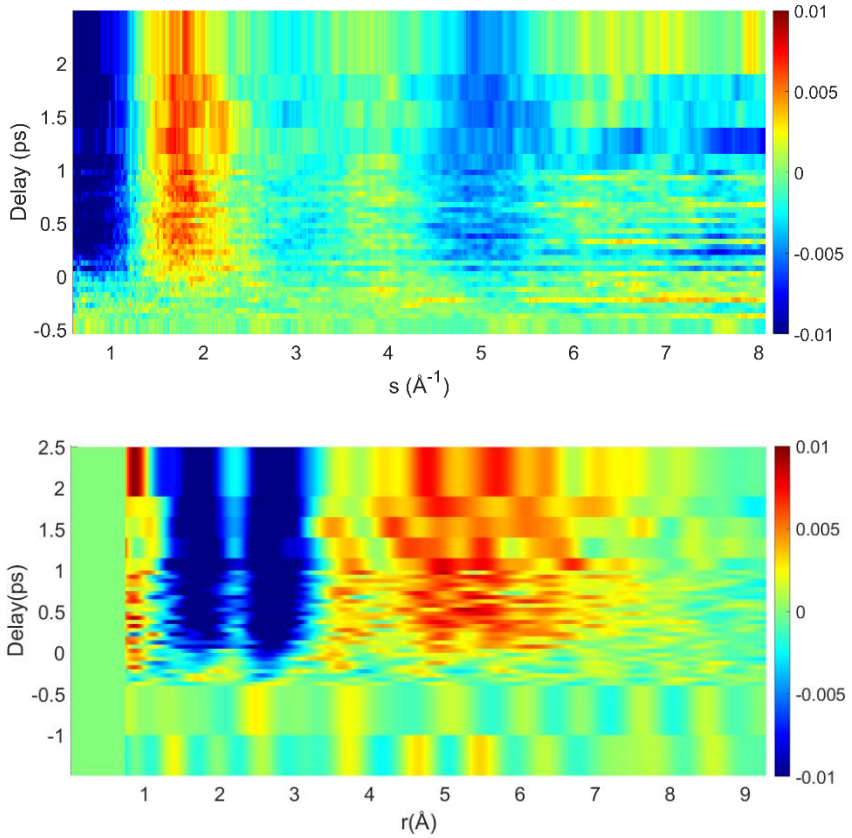

Figure 5.14: ΔI/I and ΔPDF false color map of oxalyl chloride in low charge regime.

5.9 Conclusion

MeV Ultrafast electron diffraction technique has enabled us to unravel more complicated dissociation dynamics in real time and space. Using this technique, we studied the unique UV photodissociation of oxalyl chloride to determine which previously proposed mechanisms are responsible for its dissociation giving rise to four fragments. Here, we used ultrashort UV pulses with the wavelength of 200 nm to induce excitation in the system and further probed the structural evolution with relativistic ultrafast electron pulses propagating with a small angle with respect to the optical pulses. The elastically scattered electrons create interference patterns that are imaged on a phosphor screen through a CCD camera. The resulting diffraction patterns formed at different time delays with respect to the optical pulse are further analyzed to extract structural information.

Based on our initial analysis of time-resolved electron diffraction patterns we found that CO is the main produced fragment. We did not detect any COCl radical formation, indicating that the dissociation of the molecule at this UV wavelength, more probably follows a synchronous concerted four body dissociation mechanism where all three bonds are broken at the same time scale. The ultrafast appearance of all main features in the diffraction patterns and their persistence suggested that unlike the first experimental study on the dissociation dynamics of this molecule, the dissociation occurs through one single step. We found a significant positive signal could be attributed to the gauche conformer owing to selective depletion of the anti conformer. Further molecular dynamics simulations are needed to create simulated diffraction patterns based on different scenarios and compare them with the experimental patterns to find the best match.

APPENDIX A

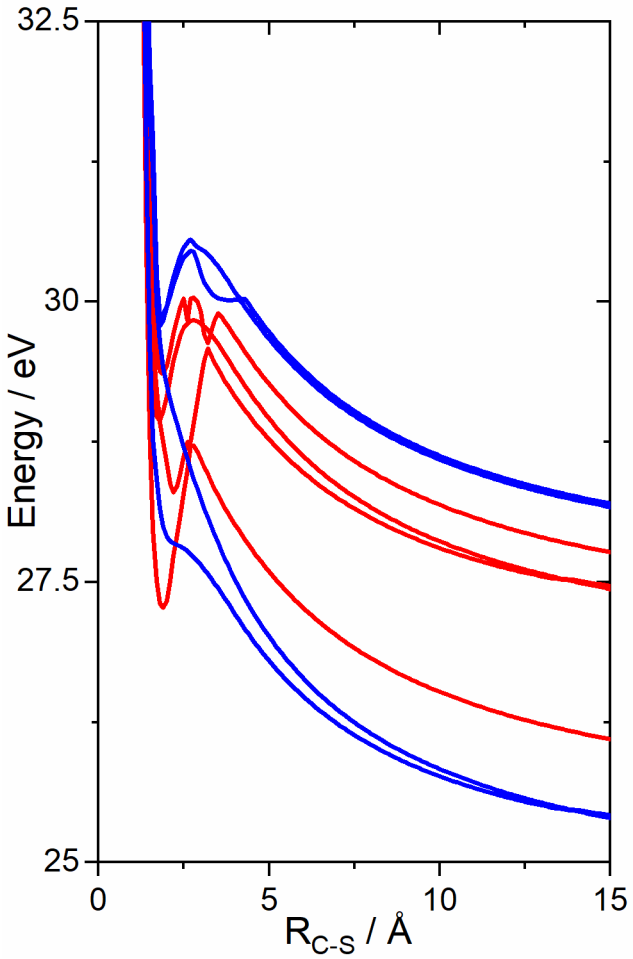

Figure A1: Potential energy curves at the ωB97X-D/aug-cc-pVTZ level along the C-S elongation coordinate of $CCSC^{2+}$ for excited singlet (blue) and triplet (red) states. All other coordinates were fixed at the values for the ground state neutral equilibrium geometry, and the energy is relative to the energy of the neutral molecule at equilibrium.

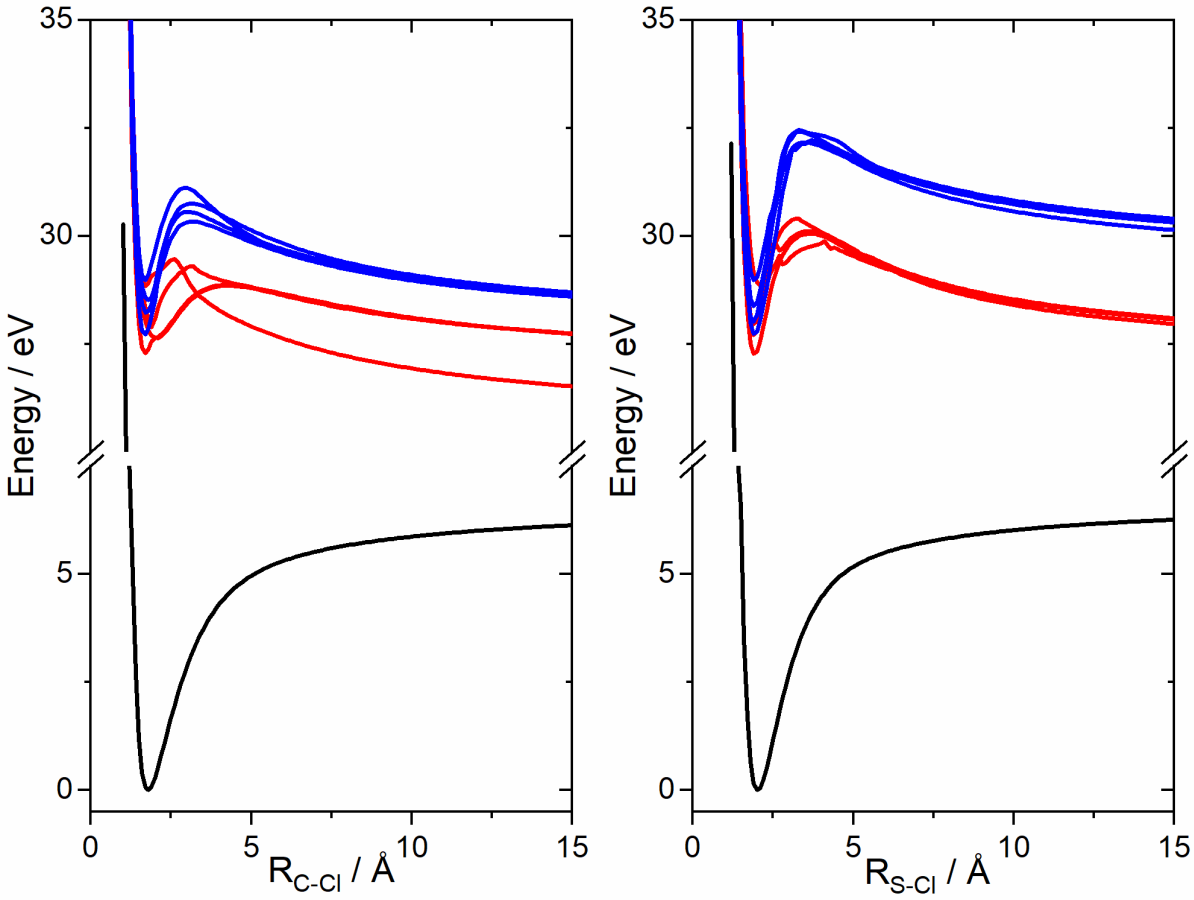

Figure A2: Potential energy curves at the ωB97X-D/aug-cc-pVTZ level along the C-Cl (left) and S–Cl (right) elongation coordinates of $CCSC^{2+}$ for excited singlet (blue) and triplet (red) states and the ground state of the neutral molecule (black). All other coordinates were fixed at the values for the ground state neutral equilibrium geometry, and the energy is relative to the energy of the neutral molecule at equilibrium.

BIBLIOGRAPHY

[1] J. O. Thompson, S. T. Alavi, J. R. Walensky and A. G. Suits, Int. J. Mass spectrom. **445**, 116190 (2019).

[2] G. A. Cooper, S. T. Alavi, W. Li, S. K. Lee and A. G. Suits, J. Phys. Chem A (2021).

[3] S. T. Alavi, G. A. Cooper and A. G. Suits, Mol. Phys. **120** (1-2), e1988170 (2022).

[4] R. D. Levine, *Molecular reaction dynamics*. (Cambridge University Press, 2009).

[5] J. Farrar and Y.-T. Lee, Annu. Rev. Phys. Chem. **25** (1), 357 (1974).

[6] M. Born and R. Oppenheimer, Annalen der physik **389** (20), 457 (1927).

[7] N. F. Ramsey, Z. Phys. **10** (2), 121 (1988).

[8] L. Dunoyer, C.R **157** (1911).

[9] O. Stern, Z. Physik **7** (1), 249 (1921).

[10] A. G. Suits and R. E. Continetti, (2001).

[11] P. French, Rep. Prog. Phys. **58** (2), 169 (1995).

[12] W. Kaiser, Top. Appl. Phys. **60** (1988).

[13] L. J. Butler, Annu. Rev. Phys. Chem. **49** (1), 125 (1998).

[14] A. P. Veenstra, L. Monzel, A. Baksi, J. Czekner, S. Lebedkin, E. K. Schneider, T. Pradeep, A.-N. Unterreiner and M. M. Kappes, J. Phys. Chem. Letts **11** (7), 2675 (2020).

[15] R. Minns, D. Parker, T. Penfold, G. Worth and H. Fielding, Phys. Chem. Chem. Phys **12** (48), 15607 (2010).

[16] R. A. Marsh, J. M. Hodgkiss, S. Albert-Seifried and R. H. Friend, Nano Letts. **10** (3), 923 (2010).

[17] A.-M. Dowgiallo, K. S. Mistry, J. C. Johnson and J. L. Blackburn, ACS nano **8** (8), 8573 (2014).

[18] M. Grifoni and P. Hänggi, Phys. Rep. **304** (5-6), 229 (1998).

[19] T. Oka, R. Arita and H. Aoki, Phys. rev. Lett **91** (6), 066406 (2003).

[20] K. Liu, S. Luo, M. Li, Y. Li, Y. Feng, B. Du, Y. Zhou, P. Lu and I. Barth, Phys. rev. Lett **122** (5), 053202 (2019).

[21] J. C. Tully, in *Modern methods for multidimensional dynamics computations in chemistry* (World Scientific, 1998), pp. 34.

[22] A. Stolow, A. E. Bragg and D. M. Neumark, Chem. Rev **104** (4), 1719 (2004).

[23] A. H. Zewail, J. Phys. Chem. A. **104** (24), 5660 (2000).

[24] M. Protopapas, C.H Keitel and P.L Knight, Rep. Prog. Phys. **60** (4), 389 (1997).

[25] M. Y. Ivanov, M. Spanner and O. Smirnova, J. Mod. Opt **52** (2-3), 165 (2005).

[26] H. Reiss, Phys. Rev. Lett. **101** (4), 043002 (2008).

[27] T. Nubbemeyer, K. Gorling, A. Saenz, U. Eichmann and W. Sandner, Phys. Rev. Lett. **101** (23), 233001 (2008).

[28] F. Fabre, G. Petite, P. Agostini and M. Clement, J. Phys. B- At. Mol. OPT **15** (9), 1353 (1982).

[29] P. Agostini, F. Fabre, G. Mainfray, G. Petite and N. K. Rahman, Phys. Rev. Lett. **42** (17), 1127 (1979).

[30] L. V. Keldysh, Sov. Phys. Uspeckhi **8** (3), 496 (1965).

[31] A. D. Sakharov, R. Z. Lyudaev, E. N. Smirnov, Y. I. Plyushchev, A. I. Pavlovskiĭ, V. K. Chernyshev, E. Feoktistova, E. I. Zharinov and Y. A. Zysin, in *Dokl. Akad. Nauk* (Russian Academy of Sciences, 1965), Vol. 165, pp. 65.

[32] S. Augst, D. Strickland, D. D. Meyerhofer, S.-L. Chin and J. H. Eberly, Phys. Rev. Lett. **63** (20), 2212 (1989).

[33] L. Keldysh, Sov. Phys. JETP **20** (5), 1307 (1965).

[34] H. Reiss, Phys. Rev. A **82** (2), 023418 (2010).

[35] M. Ferray, A. L'Huillier, X. Li, L. Lompre, G. Mainfray and C. Manus, J. Phys. B-At. Mol. OPT **21** (3), L31 (1988).

[36] P. B. Corkum, Phys. Rev. Lett. **71** (13), 1994 (1993).

[37] P. Corkum, N. Burnett and M. Y. Ivanov, Opt. Lett. **19** (22), 1870 (1994).

[38] A. Couairon*, J. Biegert, C. Hauri, W. Kornelis, F. Helbing, U. Keller and A. Mysyrowicz, J. Mod. Opt **53** (1-2), 75 (2006).

[39] M. Lewenstein, P. Balcou, M. Y. Ivanov, A. L'huillier and P. B. Corkum, Phys. Rev. A **49** (3), 2117 (1994).

[40] J. L. Krause, K. J. Schafer and K. C. Kulander, Phys. Rev. Lett. **68** (24), 3535 (1992).

[41] M. Protopapas, C. H. Keitel and P. L. Knight, Rep. Prog. Phys. **60**, 389 (1997).

[42] T. A. Carlson and R. M. White, J. Chem. Phys.

44 (12), 4510 (1966).

[43] F. Allum, M. Burt, K. Amini, R. Boll, H. Köckert, P. K. Olshin, S. Bari, C. Bomme, F. Braußе and B. Cunha de Miranda, J.Chem.Phys **149** (20), 204313 (2018).

[44] A. McPherson, T. Luk, B. Thompson, K. Boyer and C. Rhodes, Appl. Phys. B **57** (5), 337 (1993).

[45] C. Rose-Petruck, K. Schafer, K. Wilson and C. Barty, Phys. Rev. A **55** (2), 1182 (1997).

[46] W. Wiley and I. H. McLaren, Rev. Sci. Instrum. **26** (12), 1150 (1955).

[47] D. Townsend, M. P. Minitti and A. G. Suits, Rev. Sci. Instrum. **74** (4), 2530 (2003).

[48] M. Nakajima, N. Kobayashi, K. Horioka, J. Hasegawa and M. Ogawa, in *National Institute for Fusion Science - Procedings* (2005).

[49] S. K. Lee, F. Cudry, Y. F. Lin, S. Lingenfelter, A. H. Winney, L. Fan and W. Li, Rev. Sci. Instrum. **85** (12), 123303 (2014).

[50] D. Proch and T. Trickl, Rev. Sci. Instrum. **60** (4), 713 (1989).

[51] M. E. Fermann, A. Galvanauskas and G. Sucha. (CRC Press, 2002).

[52] H. A. Haus, IEEE J. Sel **6** (6), 1173 (2000).

[53] K. Gürs, Quantum Elec., 1113 (1964).

[54] M. DiDomenico Jr, J. Appl. Phys. **35** (10), 2870 (1964).

[55] L. Hargrove, R. L. Fork and M. Pollack, Appl. Phys. Lett. **5** (1), 4 (1964).

[56] H. W. Mocker and R. Collins, Appl. Phys. Lett. **7** (10), 270 (1965).

[57] C.-P. Huang, M. T. Asaki, S. Backus, M. M. Murnane, H. C. Kapteyn and H. Nathel, Opt. Lett. **17** (18), 1289 (1992).

[58] P. F. Moulton, JOSA B **3** (1), 125 (1986).

[59] F. Salin, J. Squier and M. Piche, Opt. Lett. **16** (21), 1674 (1991).

[60] D. Strickland and G. Mourou, Opt. Commun. **55** (6), 447 (1985).

[61] E. Treacy, IEEE J. Quantum Electron. **5** (9), 454 (1969).

[62] in *Two-Photon Fluorescence Detects Ultrashort Pulses,* Phys. Today **20** (9), 63 (1967).

[63] E. Ippen and C. Shank, in *Top. Appl. Phys.* (Springer, 1984), pp. 83.

[64] F. Salin, P. Georges, G. Roger and A. Brun, Appl. Opt. **26** (21), 4528 (1987).

[65] J. Janszky, G. Corradi and R. Gyuzalian, Opt. Commun. **23** (3), 293 (1977).

[66] R. Gyuzalian, S. Sogomonian and Z. G. Horvath, Opt. Commun. **29** (2), 239 (1979).

[67] J. Collier, C. Hernandez-Gomez, R. Allott, C. Danson and A. Hall, Laser Part. Beams. **19** (2), 231 (2001).

[68] M. Raghuramaiah, A. Sharma, P. Naik, P. Gupta and R. Ganeev, Sadhana **26** (6), 603 (2001).

[69] Y. Ishida, T. Yajima and A. Watanabe, Opt. Commun. **56** (1), 57 (1985).

[70] B. Schenkel, J. Biegert, U. Keller, C. Vozzi, M. Nisoli, G. Sansone, S. Stagira, S. De Silvestri and O. Svelto, Opt. Lett. **28** (20), 1987 (2003).

[71] A. Galvanauskas, D. Harter, M. Arbore, M. Chou and M. Fejer, Opt. Lett. **23** (21), 1695 (1998).

[72] A. Stabinis, G. Valiulis and E. Ibragimov, Opt. Commun. **86** (3-4), 301 (1991).

[73] J. Biegert and J.-C. Diels, JOSA B **18** (8), 1218 (2001).

[74] J. Moses and F. W. Wise, Opt. Lett. **31** (12), 1881 (2006).

[75] R. W. Boyd, *Nonlinear optics*. (Academic press, 2020).

[76] A. Srinivasa Rao, arXiv e-prints, arXiv: 1612.09399 (2016).

[77] A. Suda and T. Takeda, Appl. Sci. **2** (2), 549 (2012).

[78] Á. Börzsönyi, Z. Heiner, A. Kovács, M. Kalashnikov and K. Osvay, Opt. Express **18** (25), 25847 (2010).

[79] D. Uryupina, M. Kurilova, A. Mazhorova, N. Panov, R. Volkov, S. Gorgutsa, O. Kosareva, A. Savel'ev and S. L. Chin, JOSA B **27** (4), 667 (2010).

[80] D. Grischkowsky and A. Balant, in *Physics of New Laser Sources* (Springer, 1982), pp. 109.

[81] B. Nikolaus and D. Grischkowsky, in *Physics of New Laser Sources* (Springer, 1983), pp. 117.

[82] W. Knox, R. Fork, M. Downer, R. Stolen, C. Shank and J. Valdmanis, Appl. Phys. Lett. **46** (12), 1120 (1985).

[83] M. Nisoli, S. De Silvestri and O. Svelto, Appl. Phys. Lett. **68** (20), 2793 (1996).

[84] Y. Wang, X. Peng, M. Alharbi, C. F. Dutin, T. D. Bradley, F. Gérôme, M. Mielke, T. Booth and F. Benabid, Opt. Lett **37** (15), 3111 (2012).

[85] E. Haddad, R. Safaei, A. Leblanc, R. Piccoli, Y.-G. Jeong, H. Ibrahim, B. E. Schmidt, R. Morandotti, L. Razzari and F. Légaré, Opt. Express **26** (19), 25426 (2018).

[86] O. Heckl, C. J. Saraceno, C. Baer, T. Südmeyer, Y. Wang, Y. Cheng, F. Benabid and U. Keller, Opt. Express **19** (20), 19142 (2011).

[87] E. A. Marcatili and R. Schmeltzer, Bell Syst. Tech **43** (4), 1783 (1964).

[88] A. Hoffmann, M. Zürch, M. Gräfe and C. Spielmann, Opt. Express **22** (10), 12038 (2014).

[89] E. Haddad, R. Safaei, A. Leblanc, R. Piccoli, Y.-G. Jeong, H. Ibrahim, B. E. Schmidt, R. Morandotti, L. Razzari and F. Légaré, Opt. Express **26** (19), 25426 (2018).

[90] J. E. Beetar, M. Nrisimhamurty, T.-C. Truong, G. C. Nagar, Y. Liu, J. Nesper, O. Suarez, F. Rivas, Y. Wu and B. Shim, Sci. Adv. **6** (34), eabb5375 (2020).

[91] C. Li, K. Rishad, P. Horak, Y. Matsuura and D. Faccio, Opt. Express **22** (1), 1143 (2014).

[92] A. Couairon and A. Mysyrowicz, Phys. Rep. **441** (2-4), 47 (2007).

[93] P. Weinberger, Philos. Mag. Lett. **88** (12), 897 (2008).

[94] A. Couairon, M. Franco, A. Mysyrowicz, J. Biegert and U. Keller, Opt. Lett. **30** (19), 2657 (2005).

[95] J. Park, J.-h. Lee and C. H. Nam, Opt. Express **16** (7), 4465 (2008).

[96] C. Hauri, W. Kornelis, F. Helbing, A. Heinrich, A. Couairon, A. Mysyrowicz, J. Biegert and U. Keller, Appl. Phys. B **79** (6), 673 (2004).

[97] L. Gallmann, T. Pfeifer, P. Nagel, M. Abel, D. Neumark and S. Leone, Appl. Phys. B **86** (4), 561 (2007).

[98] D. W. Chandler and P. L. Houston, J.Chem.Phys **87** (2), 1445 (1987).

[99] A. T. Eppink and D. H. Parker, Rev. Sci. Instrum. **68** (9), 3477 (1997).

[100] C. R. Gebhardt, T. P. Rakitzis, P. C. Samartzis, V. Ladopoulos and T. N. Kitsopoulos, Rev. Sci. Instrum. **72** (10), 3848 (2001).

[101] W. Li, S. D. Chambreau, S. A. Lahankar and A. G. Suits, Rev. Sci. Instrum. **76** (6), 063106 (2005).

[102] T. P. Rakitzis and R. N. Zare, J.Chem.Phys **110** (7), 3341 (1999).

[103] C. H. Greene and R. N. Zare, Annu. Rev. Phys. Chem. **33** (1), 119 (1982).

[104] J. L. Wiza, Nucl. Instrum. Methods **162** (1-3), 587 (1979).

[105] A. G. Suits and R. E. Continetti, *Imaging in chemical dynamics: The state of the art*. (2001).

[106] D. Rolles, Z. Pešić, M. Perri, R. Bilodeau, G. Ackerman, B. Rude, A. Kilcoyne, J. Bozek and N. Berrah, Nucl. Instrum. Methods. Phys. Res B **261** (1-2), 170 (2007).

[107] C. Vallance, D. Heathcote and J. W. Lee, J. Phys. Chem A **125** (5), 1117 (2021).

[108] Z. Pešić, D. Rolles, M. Perri, R. Bilodeau, G. Ackerman, B. Rude, A. Kilcoyne, J. Bozek and N. Berrah, J. Electron. Spectrosc. Relat. Phenom. **155** (1-3), 155 (2007).

[109] L. J. Frasinski, J. Phys. B- At. Mol. OPT **49** (15), 152004 (2016).

[110] L. Frasinski, K. Codling and P. Hatherly, J. Sci **246** (4933), 1029 (1989).

[111] J. H. Eland, Acc. Chem. Res. **22** (11), 381 (1989).

[112] C. S. Slater, S. Blake, M. Brouard, A. Lauer, C. Vallance, C. S. Bohun, L. Christensen, J. H. Nielsen, M. P. Johansson and H. Stapelfeldt, Phys. Rev. A **91** (5), 053424 (2015).

[113] J. L. Hansen, J. H. Nielsen, C. B. Madsen, A. T. Lindhardt, M. P. Johansson, T. Skrydstrup, L. B. Madsen and H. Stapelfeldt, J. Chem. Phys. **136** (20), 204310 (2012).

[114] C. S. Slater, S. Blake, M. Brouard, A. Lauer, C. Vallance, J. J. John, R. Turchetta, A. Nomerotski, L. Christensen and J. H. Nielsen, Physical Review A **89** (1), 011401 (2014).

[115] M. Bargheer, N. Zhavoronkov, M. Woerner and T. Elsaesser, Chemphyschem **7** (4), 783 (2006).

[116] M. Burt, K. Amini, J. W. Lee, L. Christiansen, R. R. Johansen, Y. Kobayashi, J. D. Pickering, C. Vallance, M. Brouard and H. Stapelfeldt, J.Chem.Phys **148** (9), 091102 (2018).

[117] L. Christensen, J. H. Nielsen, C. B. Brandt, C. B. Madsen, L. B. Madsen, C. S. Slater, A. Lauer, M. Brouard, M. P. Johansson and B. Shepperson, Phys. Rev. Lett. **113** (7), 073005 (2014).

[118] J. D. Pickering, K. Amini, M. Brouard, M. Burt, I. J. Bush, L. Christensen, A. Lauer, J. H. Nielsen, C. S. Slater and H. Stapelfeldt, J. Chem. Phys (2016).

[119] L. Frasinski, J. Phys. B- At. Mol. OPT **26** (14), 2225 (1993).

[120] D. Card, E. Wisniewski, D. Folmer and A. Castleman Jr, Int. J. Mass spectrom. **223**, 355 (2003).

[121] V. Zhaunerchyk, L. Frasinski, J. H. Eland and R. Feifel, Phys. Rev. A **89** (5), 053418 (2014).

[122] S. Weathersby, G. Brown, M. Centurion, T. Chase, R. Coffee, J. Corbett, J. Eichner, J. Frisch, A. Fry and M. Gühr, Rev. Sci. Instrum. **86** (7), 073702 (2015).

[123] S. Amoruso, R. Bruzzese, N. Spinelli and R. Velotta, J. Phys. B- At. Mol. OPT **32** (14), R131 (1999).

[124] A. Löbe, J. Vrenegor, R. Fleige, V. Sturm and R. Noll, Anal. Bioanal. Chem. **385** (2), 326 (2006).

[125] M. Burger, G. Schwarz, A. Gundlach-Graham, D. Käser, B. Hattendorf and D. Günther, J. Anal. Atom. Spectrom. **32** (10), 1946 (2017).

[126] J. Picard, J.-B. Sirven, J.-L. Lacour, O. Musset, D. Cardona, J.-C. Hubinois and P. Mauchien, SPECTROCHIM ACTA B **101**, 164 (2014).

[127] K. C. Hartig, S. S. Harilal, M. C. Phillips, B. E. Brumfield and I. Jovanovic, Opt. Express **25** (10), 11477 (2017).

[128] M. Zhou, L. Andrews, J. Li and B. E. Bursten, J. Am. Chem. Soc. **121** (41), 9712 (1999).

[129] Z. Varga and G. Surányi, Anal. Chim. Acta **599** (1), 16 (2007).

[130] S. V. Jovanovic, T. Kell, J. El-Haddad, C. Cochrane, C. Drummond and A. El-Jaby, J. Radioanal. Nucl. Chem. **323** (2), 831 (2020).

[131] B. T. Manard, C. D. Quarles, E. M. Wylie and N. Xu, J. Anal. At. Spectrom. **32** (9), 1680 (2017).

[132] F. E. Stanley, A. Stalcup and H. Spitz, J. Radioanal. Nucl. Chem. **295** (2), 1385 (2013).

[133] S. Amoruso, V. Berardi, R. Bruzzese, N. Spinelli and X. Wang, Appl. Surf. Sci. **127**, 953 (1998).

[134] M. Oujja, E. Rebollar and M. Castillejo, Appl. Surf. Sci. **211** (1-4), 128 (2003).

[135] R. Stoian, D. Ashkenasi, A. Rosenfeld and E. Campbell, Phys. Rev. B **62** (19), 13167 (2000).

[136] K.-H. Leitz, B. Redlingshöfer, Y. Reg, A. Otto and M. Schmidt, Phys. Procedia **12**, 230 (2011).

[137] H. Ushida, N. Takada and K. Sasaki, presented at the Journal of Physics: Conference Series, 2007 (unpublished).

[138] M. Capitelli, F. Capitelli and A. Eletskii, Spectrochim Acta Part B At Spectrosc **55** (6), 559 (2000).

[139] A. W. Miziolek, V. Palleschi and I. Schechter, *Laser induced breakdown spectroscopy*. (Cambridge university press, 2006).

[140] J. P. Singh and S. Thakur, *Laser-induced breakdown spectroscopy*. (Elsevier, 2020).

[141] D. Rusak, B. Castle, B. Smith and J. Winefordner, Crit. Rev. Anal. Chem. **27** (4), 257 (1997).

[142] H. P. Longerich, D. Günther and S. E. Jackson, Fresenius' j. Anal. Chem **355** (5), 538 (1996).

[143] H. P. Longerich, S. E. Jackson and D. Günther, J. Anal. Atom. Spectrom. **11** (9), 899 (1996).

[144] C. A. Heinrich, T. Pettke, W. E. Halter, M. Aigner-Torres, A. Audétat, D. Günther, B. Hattendorf, D. Bleiner, M. Guillong and I. Horn, Geochim. Cosmochim. Acta **67** (18), 3473 (2003).

[145] V. Unnikrishnan, K. Alti, R. Nayak, R. Bernard, V. Kartha, C. Santhosh, G. Gupta and B. Suri, Pramana **75** (6), 1145 (2010).

[146] S. Amoruso, B. Toftmann, J. Schou, R. Velotta and X. Wang, Thin Solid Films **453**, 562 (2004).

[147] I. Labazan, E. Vrbanek, S. Milošević and R. Düren, Appl. Phys. A **80** (3), 569 (2005).

[148] R. E. Russo, A. A. Bol'shakov, X. Mao, C. P. McKay, D. L. Perry and O. Sorkhabi, Spectrochim Acta Part B At Spectrosc **66** (2), 99 (2011).

[149] R. E. Russo, X. Mao, H. Liu, J. Gonzalez and S. S. Mao, Talanta **57** (3), 425 (2002).

[150] J. Gonzalez, X. Mao, J. Roy, S. Mao and R. Russo, J. Anal. At. Spectrom. **17** (9), 1108 (2002).

[151] R. E. Russo, X. Mao, J. J. Gonzalez and S. S. Mao, J. Anal. At. Spectrom. **17** (9), 1072 (2002).

[152] J. J. Gonzalez, C. Liu, S.-B. Wen, X. Mao and R. E. Russo, Talanta **73** (3), 567 (2007).

[153] D. Günther and B. Hattendorf, TrAC Trends. Anal. Chem. **24** (3), 255 (2005).

[154] S. F. Durrant, J. Anal. Atom. Spectrom **14** (9), 1385 (1999).

[155] P. Arrowsmith, Anal. Chem. **59** (10), 1437 (1987).

[156] F. R. Doucet, G. Lithgow, R. Kosierb, P. Bouchard and M. Sabsabi, J. Anal. Atom. Spectrom. **26** (3), 536 (2011).

[157] M. Dong, D. Oropeza, J. Chirinos, J. J. González, J. Lu, X. Mao and R. E. Russo, Spectrochim Acta Part B At Spectrosc **109**, 44 (2015).

[158] F. Chandezon, B. Huber and C. Ristori, Rev. Sci. Instrum. **65** (11), 3344 (1994).

[159] Z. Varga, Anal. Chim. Acta **625** (1), 1 (2008).

[160] S. F. Boulyga and T. Prohaska, Anal. bioanal. chem. **390** (2), 531 (2008).

[161] D. Zhang, X. Ma, S. Wang and X. Zhu, Plasma Sci. Technol. **17** (11), 971 (2015).

[162] D. Manura and D. A. Dahl, *SIMION 8.0 User manual*. (Scientific Instrument Services, 2007).

[163] K. Song, D. Kim, H. Cha, Y. Kim, E. C. Jung, I. Choi, H.-S. Yoo and S. Oh, Microchem. J. **76** (1-2), 95 (2004).

[164] S.-B. Wen, X. Mao, R. Greif and R. E. Russo, J. Appl. Phys. **101** (12), 123105 (2007).

[165] S.-B. Wen, X. Mao, R. Greif and R. E. Russo, J. Appl. Phys. **101** (2), 023115 (2007).

[166] S.-B. Wen, X. Mao, R. Greif and R. E. Russo, J. Appl. Phys. **101** (2), 023114 (2007).

[167] H. Stapelfeldt, E. Constant, H. Sakai and P. B. Corkum, Phys. Rev. A **58** (1), 426 (1998).

[168] C. Ellert, H. Stapelfeldt, E. Constant, H. Sakai, J. Wright, D. Rayner and P. Corkum, Philos. Trans. Royal Soc. A **356** (1736), 329 (1998).

[169] H. Hasegawa, A. Hishikawa and K. Yamanouchi, Chem. Phys. Lett **349** (1-2), 57 (2001).

[170] F. Légaré, K. F. Lee, I. Litvinyuk, P. Dooley, S. Wesolowski, P. Bunker, P. Dombi, F. Krausz, A. Bandrauk and D. Villeneuve, Phys. Rev. A. **71** (1), 013415 (2005).

[171] J. Gagnon, K. F. Lee, D. Rayner, P. Corkum and V. Bhardwaj, J. Phys. B: At, Mol, Opt, Phys. **41** (21), 215104 (2008).

[172] M. E. Corrales, G. Gitzinger, J. González-Vázquez, V. Loriot, R. de Nalda and L. Banares, J. Phys. Chem. A **116** (11), 2669 (2012).

[173] C. S. Slater, S. Blake, M. Brouard, A. Lauer, C. Vallance, J. J. John, R. Turchetta, A. Nomerotski, L. Christensen and J. H. Nielsen, Phys. Rev. A. **89** (1), 011401 (2014).

[174] J. D. Pickering, K. Amini, M. Brouard, M. Burt, I. J. Bush, L. Christensen, A. Lauer, J. H. Nielsen, C. S. Slater and H. Stapelfeldt, J. Chem. Phys **144** (16), 161105 (2016).

[175] M. Burt, R. Boll, J. W. Lee, K. Amini, H. Köckert, C. Vallance, A. S. Gentleman, S. R. Mackenzie, S. Bari and C. Bomme, Phys. Rev. A. **96** (4), 043415 (2017).

[176] K. Amini, R. Boll, A. Lauer, M. Burt, J. W. Lee, L. Christensen, F. Brauβe, T. Mullins, E. Savelyev and U. Ablikim, J. Chem. Phys. **147** (1), 013933 (2017).

[177] M. Burt, K. Amini, J. W. Lee, L. Christiansen, R. R. Johansen, Y. Kobayashi, J. D. Pickering, C. Vallance, M. Brouard and H. Stapelfeldt, J. Chem. Phys. **148** (9), 091102 (2018).

[178] F. Allum, M. Burt, K. Amini, R. Boll, H. Köckert, P. K. Olshin, S. Bari, C. Bomme, F. Braußе and B. Cunha de Miranda, J. Chem. Phys. **149** (20), 204313 (2018).

[179] S. K. Lee, F. Cudry, Y. F. Lin, S. Lingenfelter, A. H. Winney, L. Fan and W. Li, Rev. Sci. Instrum. **85** (12), 123303 (2014).

[180] C. Weeraratna, C. Amarasinghe, S. K. Lee, W. Li and A. G. Suits, J. Chem. Phys. **149** (8), 084202 (2018).

[181] J. W. Thoman, D. W. Chandler, D. H. Parker and M. H. Janssen, Laser Chem. **9** (1-3), 27 (1988).

[182] L. Stryer, *Biochemistry*. (W.H. Freeman and Company, New York, 1995).

[183] D. Manidhar, K. Uma Maheswara Rao, C. Suresh Reddy, C. Syamasunder, K. Adeppa and K. Misra, Res. Chem. Intermed. **38** (9), 2479 (2012).

[184] A. Obreza, K. Grabrijan, S. Kadić, F. J. de Lera Garrido, I. Sosič, S. Gobec and M. Jukič, Acta Chim. Slov. **64** (4), 771 (2017).

[185] S. Izawa, H. Nakatsuji and Y. Tanabe, Molbank **2018** (1), M976 (2018).

[186] Q. Shen and K. Hagen, J. Mol. Struct. **128** (1-3), 41 (1985).

[187] A. H. Jubert, C. O. Della Vedova and P. J. Aymonino, Croat. Chem. Acta. **60** (2), 207 (1987).

[188] H. G. Mack, H. Oberhammer and C. Della Védova, J. Phys. Chem. **95** (11), 4238 (1991).

[189] R. M. Romano, C. O. Della Vedova, A. J. Downs and T. M. Greene, J. Am. Chem. Soc. **123** (24), 5794 (2001).

[190] M. F. Erben, C. O. Della Védova, R. M. Romano, R. Boese, H. Oberhammer, H. Willner and O. Sala, Inorg. Chem. **41** (5), 1064 (2002).

[191] R. M. Romano, C. O. Della Védova, A. J. Downs, S. Parsons and C. Smith, New. J. Chem. **27** (3), 514 (2003).

[192] R. M. Romano, C. O. Della Védova and A. J. Downs, J. Phys. Chem. A. **108** (35), 7179 (2004).

[193] M. F. Erben, R. M. Romano and C. O. Della Védova, J. Phys. Chem. A **109** (2), 304 (2005).

[194] L. Lin, W.-J. Ding, W.-H. Fang and R.-Z. Liu, J. Phys. Chem. A **110** (28), 8744 (2006).

[195] M. Gerones, M. F. Erben, R. M. Romano, C. O. Della Vedova, L. Yao and M. Ge, J. Phys. Chem. A **112** (11), 2228 (2008).

[196] M. F. Erben, M. Geronés, R. M. Romano and C. O. Della Védova, J. Phys. Chem A **111** (33), 8062 (2007).

[197] P. Hohenberg and W. Kohn, Phys. Rev. **B864** (1964).

[198] W. Kohn and L. J. Sham, Phys. Rev. **140** (4A), A1133 (1965).

[199] J.-D. Chai and M. Head-Gordon, Phys. Chem. Chem. Phys. **10** (44), 6615 (2008).

[200] R. A. Kendall, T. H. Dunning Jr and R. J. Harrison, J. Chem. Phys. **96** (9), 6796 (1992).

[201] D. E. Woon and T. H. Dunning Jr, J. Chem. Phys. **98** (2), 1358 (1993).

[202] T. H. Dunning Jr, J. Chem. Phys. **90** (2), 1007 (1989).

[203] R. Bauernschmitt and R. Ahlrichs, Chem. Phys. Lett. **256** (4-5), 454 (1996).

[204] M. E. Casida, C. Jamorski, K. C. Casida and D. R. Salahub, J. Chem. Phys. **108** (11), 4439 (1998).

[205] R. E. Stratmann, G. E. Scuseria and M. J. Frisch, J. Chem. Phys. **109** (19), 8218 (1998).

[206] C. Van Caillie and R. D. Amos, Chem. Phys. Lett. **308** (3-4), 249 (1999).

[207] C. Van Caillie and R. D. Amos, Chem. Phys. Lett. **317** (1-2), 159 (2000).

[208] F. Furche and R. Ahlrichs, J. Chem. Phys. **117** (16), 7433 (2002).

[209] G. Scalmani, M. J. Frisch, B. Mennucci, J. Tomasi, R. Cammi and V. Barone, J. Chem. Phys. **124** (9), 094107 (2006).

[210] M. Frisch, G. Trucks, H. Schlegel, G. Scuseria, M. Robb, J. Cheeseman, G. Scalmani, V. Barone, B. Mennucci and G. Petersson, in *Gaussian 09, Revision D. 01, Gaussian, Inc., Wallingford CT* (2009).

[211] M. Frisch, G. Trucks, H. Schlegel, G. Scuseria, M. Robb, J. Cheeseman, G. Scalmani, V. Barone, G. Petersson and H. Nakatsuji, (Gaussian, Inc. Wallingford, CT, 2016).

[212] C. Lee, W. Yang and R. G. Parr, Phys. Rev B **37** (2), 785 (1988).

[213] A. McLean and G. Chandler, J. Chem. Phys. **72** (10), 5639 (1980).

[214] J. Thompson, C. Amarasinghe, C. Foley and A. Suits, J. Chem. Phys. **147** (1), 013913 (2017).

[215] L. Frasinski, K. Codling, P. Hatherly, J. Barr, I. Ross and W. Toner, Phys. Rev. Lett. **58** (23), 2424 (1987).

[216] C. Cornaggia, M. Schmidt and D. Normand, J. Phys. B: At, Mol, Opt, Phys **27** (7), L123 (1994).

[217] P. Hering and C. Cornaggia, Phys. Rev. A **59** (4), 2836 (1999).

[218] M. Brewczyk and L. Frasinski, J. Phys. B: At, Mol, Opt, Phys **24** (13), L307 (1991).

[219] H. Willner, J. Chem. Sci **39** (3), 314 (1984).

[220] J. Brazard, L. A. Bizimana, T. Gellen, W. P. Carbery and D. B. Turner, J. Phys. Chem. Lett **7** (1), 14 (2016).

[221] A. H. Zewail, Angew. Chem. Int. Ed. **39** (15), 2586 (2000).

[222] H. Ihee, M. Lorenc, T. K. Kim, Q. Y. Kong, M. Cammarata, J. H. Lee, S. Bratos and M. Wulff, Science **309** (5738), 1223 (2005).

[223] M. Minitti, J. Budarz, A. Kirrander, J. Robinson, D. Ratner, T. Lane, D. Zhu, J. Glownia, M. Kozina and H. Lemke, Phys. Rev. Lett **114** (25), 255501 (2015).

[224] F. Schotte, M. Lim, T. A. Jackson, A. V. Smirnov, J. Soman, J. S. Olson, G. N. Phillips Jr, M. Wulff and P. A. Anfinrud, Science **300** (5627), 1944 (2003).

[225] K. Amini and J. Biegert, in *Advances In Atomic, Molecular, and Optical Physics* (Elsevier, 2020), Vol. 69, pp. 163.

[226] R. Henderson, Q. Rev. Biophys. **28** (2), 171 (1995).

[227] S. Weathersby, G. Brown, M. Centurion, T. Chase, R. Coffee, J. Corbett, J. Eichner, J. Frisch, A. Fry and M. Gühr, Rev. Sci. Instrum **86** (7), 073702 (2015).

[228] J. Yang, M. Guehr, T. Vecchione, M. S. Robinson, R. Li, N. Hartmann, X. Shen, R. Coffee, J. Corbett and A. Fry, Nat. Commun. **7** (1), 1 (2016).

[229] J. Yang, M. Guehr, X. Shen, R. Li, T. Vecchione, R. Coffee, J. Corbett, A. Fry, N. Hartmann and C. Hast, Phys. Rev. Lett **117** (15), 153002 (2016).

[230] J. Yang, X. Zhu, T. J. Wolf, Z. Li, J. P. F. Nunes, R. Coffee, J. P. Cryan, M. Gühr, K. Hegazy and T. F. Heinz, Science **361** (6397), 64 (2018).

[231] K. J. Wilkin, R. M. Parrish, J. Yang, T. J. Wolf, J. P. F. Nunes, M. Guehr, R. Li, X. Shen, Q. Zheng and X. Wang, Phys. Rev. A. **100** (2), 023402 (2019).

[232] T. J. Wolf, D. M. Sanchez, J. Yang, R. Parrish, J. Nunes, M. Centurion, R. Coffee, J. Cryan, M. Gühr and K. Hegazy, Nat. Chem **11** (6), 504 (2019).

[233] J. Yang, X. Zhu, J. P. F. Nunes, J. K. Yu, R. M. Parrish, T. J. Wolf, M. Centurion, M. Gühr, R. Li and Y. Liu, Science **368** (6493), 885 (2020).

[234] R. Adams and L. Ulich, J. Am. Chem. Soc **42** (3), 599 (1920).

[235] A. Speziale and L. Smith, J. Org. Chem **28** (7), 1805 (1963).

[236] T. Iida and T. Itaya, Tetrahcdron **49** (46), 10511 (1993).

[237] A. J. Mancuso, S.-L. Huang and D. Swern, J. Org. Chem **43** (12), 2480 (1978).

[238] F. Babudri, V. Fiandanese, G. Marchese and A. Punzi, Tetrahedron Lett. **36** (40), 7305 (1995).

[239] A. V. Baklanov and L. N. Krasnoperov, J. Phys. Chem. A. **105** (1), 97 (2001).

[240] D. D. Danielson, L. Hedberg, K. Hedberg, K. Hagen and M. Trtteberg, J. Phys. Chem **99** (23), 9374 (1995).

[241] M. Ahmed, D. Blunt, D. Chen and A. G. Suits, J. Chem. Phys. **106** (18), 7617 (1997).

[242] N. Hemmi and A. G. Suits, J. Phys. Chem. A **101** (36), 6633 (1997).

[243] C.-Y. Wu, Y.-P. Lee, J. Ogilvie and N. S. Wang, J. Phys. Chem. A **107** (14), 2389 (2003).

[244] C.-Y. Wu, Y.-P. Lee and N. S. Wang, J. Chem. Phys **120** (15), 6957 (2004).

[245] Q. Fang, L. Shen and W.-H. Fang, J. Chem. Phys **139** (2), 024310 (2013).

[246] R. A. Bonham, *HIGH ENERGY ELECTRON SCATTERING*. (Van Nostrand Reinhold, 1974).

[247] O. Bastiansen, L. Hedberg and K. Hedberg, J. Chem. Phys **27** (6), 1311 (1957).

[248] M. Hargittai, *Stereochemical Applications of Gas-Phase Electron Diffraction, Part A*. (John Wiley & Sons, 1988).

[249] N. L. Müller, Universität Hamburg Hamburg, 2016.

[250] I. Hargittai and M. Hargittai, *Stereochemical applications of gas-phase electron diffraction*. (VCH, 1988).

[251] F. Salvat, A. Jablonski and C. J. Powell, Comp. Phys. Commun **165** (2), 157 (2005).

[252] G. Wysin, Department of Physics, Kansas State University, 66506, 2601, 2011.

[253] L. Frasinski, K. Codling, P. Hatherly, J. Barr, I. Ross and W. Toner, Phys. Rev. lett **58** (23), 2424 (1987).

[254] H. Ihee, B. M. Goodson, R. Srinivasan, V. A. Lobastov and A. H. Zewail, J. Phys. Chem. A. **106** (16), 4087 (2002).

[255] H. Ihee, V. A. Lobastov, U. M. Gomez, B. M. Goodson, R. Srinivasan, C.-Y. Ruan and A. H. Zewail, Science **291** (5503), 458 (2001).

[256] M. Version, (MathWorks, Natick, MA, USA, 2021).

[257] R. Srinivasan, V. A. Lobastov, C. Y. Ruan and A. H. Zewail, Helv. Chim. Acta **86** (6), 1761 (2003).

[258] B. R. A. Anthony J W, Bladh K W, and Nichols M C, (University of Arizona Mineral Museum, 1990).

[259] E. K. Gross and N. T. Maitra, in *Fundamentals of Time-Dependent Density Functional Theory* (Springer, 2012), pp. 53.

[260] M. Frisch, G. Trucks, H. Schlegel, G. Scuseria, M. Robb, J. Cheeseman, G. Scalmani, V. Barone, G. Petersson and H. Nakatsuji, Wallingford CT **2** (4) (2016).

[261] Q. Fang, L. Shen and W.-H. Fang, J.Chem.Phys **139** (2), 024310 (2013).

VITA

Tahereh Alavi was born in Tehran, Iran. After graduating high school with a major in mathematics and physics, entered the nation's leading institute for science and engineering, Sharif University of Technology, through the national university entrance exam. In 2011, she received a B.Sc. in chemical engineering as a distinguished student which granted her the entrance to the master's program at the Amirkabir University of Technology (Tehran Polytechnique). She earned a M.Sc. degree in chemical engineering as an honor student in 2013. She started her Ph.D. in 2016 under the supervision of Prof. Arthur G. Suits at the University of Missouri-Columbia. She involved in various research projects during her Ph.D. including the state-resolved photodissociation studies, laser-induced plasma mass spectrometry, Coulomb Explosion dynamics of polyatomic molecules, and ultrafast electron diffraction imaging.